Master's thesis

NTNU
Norwegian University of Science and Technology
Faculty of Engineering

Christian Berge Foyn

# Temperature measurement in lithium-ion batteries using FBG

Master's thesis in I&IKT
Supervisor: Jacob J. Lamb
Co-supervisor: Markus S. Wahl, Odne S. Burheim
June 2022

NTNU
Kunnskap for en bedre verden

Christian Berge Foyn

# Temperature measurement in lithium-ion batteries using FBG

Master's thesis in I&IKT
Supervisor: Jacob J. Lamb
Co-supervisor: Markus S. Wahl, Odne S. Burheim
June 2022

Norwegian University of Science and Technology
Faculty of Engineering

NTNU
Norwegian University of
Science and Technology

**Abstract**

As lithium-ion batteries (LIBs) and their applications continue to grow, there is an increasing need to control and monitor the internal state of the battery. Temperature is highly affecting the performance, safety and longevity of LIBs in all applications. Thermal management of the battery is therefore key to enable safe and optimal operation of the battery in use. Currently, temperature measurements are typically done on the battery surface, which do not reflect the true internal state of the battery. Therefore, internal temperature measurements are valuable to improve knowledge on the thermal characteristics of lithium-ion batteries. However, the internal environment of a LIB is chemically harsh and subject to electromagnetic interference, which make internal measurements difficult to obtain. Fiber bragg grating (FBG) sensors are however chemically inert and resistant to electromagnetic interference, which enables them to accurately monitor the internal state of the battery.

In this thesis, commercial LIBs are implemented with FBG sensors to obtain internal temperature measurements of the batteries in use. The batteries are characterised before and after sensor implementation to evaluate the impact of the implementation process on the battery performance. In addition, the batteries are put through a cycle aging schedule to reveal changes in the thermodynamic properties and aging characteristics of the instrumented batteries. The temperature tests revealed large temperature differences between internal and external temperature measurements, peaking at 14.6°C at the end of discharge in an aged cell. The elevated internal resistances of the batteries after sensor implementation gave a significant temperature response, which increased at higher currents. The temperature tests gave a detailed view on the temperature development in a LIB in use, emphasising the importance of internal temperature measurements.

# Table of Contents

**List of Figures** iii

**List of Tables** v

**1 Introduction** 1

**2 Theory** 3

2.1 Working principle of a lithium-ion battery . . . 3

2.1.1 Cathode materials . . . 4

2.1.2 Anode materials . . . 6

2.1.3 Electrolyte and separator . . . 8

2.1.4 Physical properties . . . 8

2.2 Thermal behavior of LIBs . . . 9

2.2.1 Heat generation . . . 9

2.2.2 Thermal conduction . . . 11

2.2.3 Thermal dissipation . . . 11

2.2.4 Thermal balance and modeling . . . 12

2.2.5 Thermal gradients . . . 13

2.2.6 Thermal management . . . 14

2.3 Thermal effects on aging and performance . . . 15

2.3.1 Temperature and battery performance . . . 16

2.3.2 Aging and degradation . . . 17

2.3.3 Safety issues . . . 19

2.4 Light properties . . . 20

2.4.1 Light wave properties . . . 20

2.4.2 Basics of optical fibers . . . 20

2.5 Optical fiber sensors . . . 22

2.6 Fiber Bragg gratings . . . 23

**3 Methods** 25

3.1 Implementation procedure . . . 26

3.1.1 Pouch assembly . . . 26

3.1.2 Pouch removal and repack . . . 27

3.2 Battery testing and characterization . . . 29

3.3 Cycle aging . . . 31

3.4 FBG calibration and measurement . . . 31
3.5 Temperature measurements . . . 34
3.6 Battery type . . . 34

**4 Results and discussion** **34**
4.1 Implementation procedure and invasiveness . . . 34
4.1.1 Cell capacity . . . 35
4.1.2 Internal resistance . . . 38
4.2 Aging effects . . . 40
4.3 Temperature tests . . . 43
4.4 Visual inspection . . . 53

**5 Conclusion** **56**

**Bibliography** **57**

**Appendix** **65**

# List of Figures

1 BMS . . . 1
2 LIB - working principle . . . 4
3 Electrochemical potential . . . 5
4 Overview of cathode and anode materials . . . 7
5 Physical construction of a LIB . . . 8
6 LIB cell types . . . 9
7 Modeled heat generation in a LIB . . . 10
8 Temperature gradients in a cylindrical LIB . . . 14
9 Temperature gradients due to cooling . . . 14
10 PCM cooling system . . . 15
11 Cycle aging . . . 16
12 Capacity Retention . . . 16
13 Impedence rise . . . 17
14 SEI . . . 18
15 Cycle aging for different cathode chemistries . . . 18
16 Resistance heating . . . 19
17 Thermal hazards . . . 19

18 Electromagnetic spectrum . . . . . 20
19 Physical construction of an optical fiber . . . . . 21
20 Refraction . . . . . 21
21 Light propagation . . . . . 22
22 General setup for optical sensing . . . . . 22
23 FBG working principle . . . . . 24
24 Project overview . . . . . 25
25 Pouch design . . . . . 26
26 Pouch assembly process 1 . . . . . 27
27 Pouch assembly process 2 . . . . . 28
28 Folds on pouch seal . . . . . 29
29 HPPC . . . . . 30
30 HPPC discharge pulse . . . . . 31
31 FBG equipment specifications . . . . . 32
32 FBG sensor setup . . . . . 32
33 Reflected wavelength spectrum . . . . . 32
34 Temperature sensitivity . . . . . 33
35 Central wavelength detection with Gaussian . . . . . 33
36 Melasta SLPBB042126 . . . . . 34
37 OCV post implementation . . . . . 35
38 Characterization plot . . . . . 36
39 Discharge capacity prior to implementation . . . . . 36
40 Discharge capacity after implementation . . . . . 37
41 Discharge capacity comparison . . . . . 38
42 Total internal resistance post implementation . . . . . 38
43 HPPC Third LCO . . . . . 39
44 HPPC Reference LCO . . . . . 39
45 R2 resistance after implementation . . . . . 40
46 Capacity fade during cycle aging . . . . . 40
47 Resistance increase during cycle aging . . . . . 41
48 Relative increase internal resistance . . . . . 41
49 Resistance and capacity during cycle aging . . . . . 42
50 Temperature test - second LCO overview . . . . . 43
51 1C discharge temperature - second LCO . . . . . 44
52 1.5C discharge temperature - second LCO . . . . . 45

53 C/2 discharge temperature - second LCO . . . . . 45
54 1.5C discharge temperature and voltage - second LCO . . . . . 46
55 External vs. internal temperature - second LCO . . . . . 46
56 Temperature test - third LCO overview . . . . . 47
57 1.5C discharge temperature - third LCO . . . . . 47
58 1.5C charge temperature - third LCO . . . . . 48
59 Charge onset temperature change - third LCO . . . . . 49
60 External vs. internal temperature - third LCO . . . . . 49
61 Post aging temperature test overview . . . . . 50
62 External vs. internal temperature - second LCO aged . . . . . 50
63 Post aging temperature increase rate . . . . . 51
64 Temperature increase rates - overview . . . . . 51
65 Temperature increase rate second LCO . . . . . 52
66 Temperature increase rate third LCO . . . . . 52
67 Temperature increase rate second LCO - aged . . . . . 52
68 Cell thickness post mortem . . . . . 53
69 Anode degradation on the instrumented electrode . . . . . 54
70 Anode degradation . . . . . 54
71 Anode and cathode degradation . . . . . 55
72 Separator degradation . . . . . 55

# List of Tables

1 **Cathode chemistries** . . . . . 6
2 **Anode chemistries** . . . . . 7

# 1 Introduction

Lithium-ion batteries (LIBs) have gained popularity as energy storage devices in several applications, including portable electronics and hybrid/electric vehicles. Their success is in large due to the high energy and power density, low self-discharge rate, long cycle life and low environmental impact that is offered by them. As further transition from fossil fuels to renewable energy sources is necessary in order to limit the effects of climate change, efforts are also being made to use LIBs as electric energy storage in order to enhance wind and solar power integration to the grid.

The European Commission have targeted a reduction in the greenhouse gas emissions by 80% to 90% in 2030, compared to the levels of 1990. As the transport sector produce ∼25% of the total greenhouse gas emissions, electrifying road transport is an important step in the process. To meet the requirements of a growing electric car fleet, the European Commission have presented an action plan to decrease the dependency on countries outside EU for critical materials in battery production [1]. In addition, application of LIBs for energy storage is expected to grow intensively [2]. This is pointing towards a significant increase in the production and applications of LIBs, which in return demand lowering the environmental impact for the whole life cycle of the battery. The environmental impact of a LIB is dependent on the different contributions from raw material extraction, production, electricity used for charging and recycling. Reducing emissions in all life cycle stages will be beneficial, however, increasing the lifetime of a LIB will ultimately decrease the environmental impact equally.

To increase the lifetime of a LIB, the development of highly functional battery management systems (BMS) is critical. The BMS is an integral part of all LIB applications, as it ensures safe and optimal operation of the battery in use. Important metrics, such as State of Charge (SoC) and State of Health (SoH) are determined by the BMS based on parameters such as voltage, current and temperature that are monitored in the battery pack. The cycle life and ageing processes of a LIB is highly dependent on these internal parameters of the battery during operation. Therefore, the BMS should work to optimise these parameters, so that degradation processes in the battery are minimised.

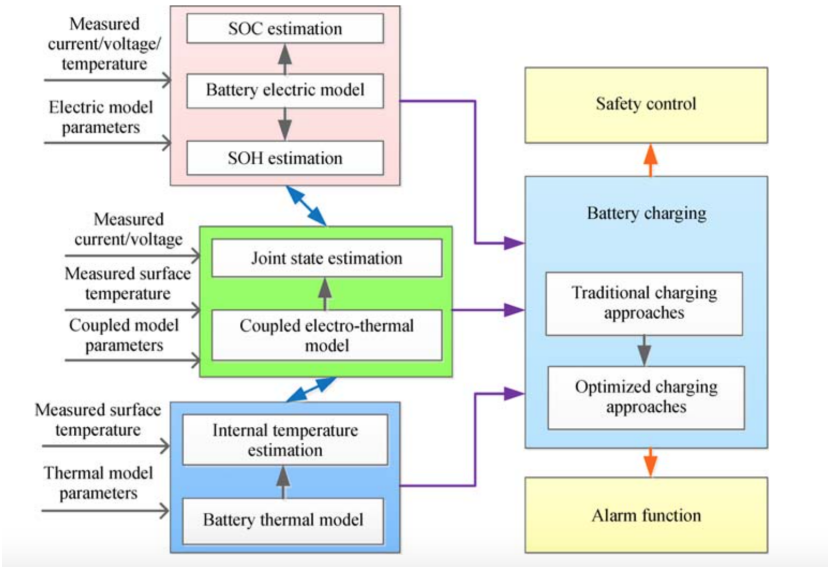


**Figure 1:** The different aspects of a battery management system including the measured surface temperature as an input for both state estimation and optimal charging strategies [3]

.

As a part of the BMS, a battery thermal management system (BTMS) is needed to operate the battery within the optimal temperature range. The BTMS is monitoring the temperature of the battery pack, and provides sufficient cooling or heating depending on the ambient conditions. This involves thermal modeling from temperature measurements obtained in the battery pack. The

accuracy of the input sensors is therefore of great importance, as they affect the accuracy of the thermal models. The sensors that are currently used in the BTMS rely mainly on external measurements, although the internal and external temperatures of the battery can deviate substantially [4]. Therefore, methods for internal temperature measurements are being developed, to increase the accuracy and reliability of the BTMS.

For internal sensing in a LIB, the need for accurate, sensitive and minimal invasive methods for fetching data is required. Several sensing methods that rely on thermocouples have been proposed [5–7], although the size and invasiveness of these sensors may negatively affect the internal state of the battery cell. Fiber optic sensors have shown promising results for internal cell-monitoring, as they are minimally invasive, non-conductive and chemically inert. Moreover, fiber sensors have multiplexing capabilities, which allows for distributed sensing inside the battery, or on battery pack level [8]. These advantageous characteristics make fiber optical sensors well suited for LIB sensing.

In the past decade, the applications of fiber optical sensors in LIBs have grown. Meyer et al. showed how the use of FBG for temperature monitoring on a LIB can improve safety and give grater sensibility compared to a thermistor [9]. Sommer et al. monitored electrode strain in the last charge phase using a FBG strain sensor, and linked it to nonuniform lithium ion distribution in the anode [10]. Nascimento et al. implemented a FBG in a LIB for internal temperature measurement, and compared it to an externally attached FBG. The study showed how the internal temperature had larger variations at a given current rate compared to the externally measured temperature [4]. Bae et al. measured the strain of a LIB by implementing a FBG into the electrode material [11]. Ganguli et al. showed how the internal strain measurements from a FBG sensor can be used for accurate SOC estimation [12]. Recently, development in data-driven methods for state estimation that rely on temperature and strain data from FBG sensors have also been researched [13],[14]. The accuracy of the data-driven methods rely both on the quantity and the quality of the test-data that is used for training and validation [15]. Hence, providing accurate and reliable data by internal battery measurements can be valuable for further development in these areas.

In this thesis, FBG sensors are implemented into commercial LIBs to monitor the internal temperature development during different charge and discharge cycles. In addition, the batteries are cycled in order to induce aging effects that impact the performance and thermal behaviour of the batteries. The batteries are characterised before and after sensor implementation and cycle aging to reveal changes in internal resistance and capacity. The goal of the thesis is to reveal thermal characteristics of the batteries in use, and evaluate the impact of the sensor implementation and aging process on the battery performance. Firstly, relevant theory for lithium-ion batteries and thermal characteristics is presented, in order to analyse the results with greater accuracy. The impact of sensor implementation and cycle aging is analysed in terms of internal resistance and capacity. Lastly, the internal temperature measurements are evaluated and compared to the external temperature measurements.

# 2 Theory

To enable good understanding and interpretation of the temperature measurements that is conducted, a thorough theoretical knowledge of the chemical and thermal behaviour of LIBs is needed. In this section, the basic working principles of a LIBs and fiber optical sensors are presented, as well as relevant thermodynamic properties of LIBs in use. Some insight in battery performance and aging will also be given, as this will be relevant for the experiments conducted later in the study.

## 2.1 Working principle of a lithium-ion battery

A lithium-ion battery consists of two electrodes and current collectors, a separator and an electrolyte (Fig. 2). Secondary LIBs are based on intercalation anodes, which rely on flow of lithium-ions to and from the anode and cathode materials to produce electricity. The flow of electrons is created through redox reactions in the cathode and anode materials, which form the potential for the magnitude of energy that a LIB can produce. During charging, Li-ions deintercalate from the cathode material, move through the porous separator, then diffuse and intercalate into the anode material. During discharge, the process is reversed, so that Li-ions deintercalate from the anode material to produce free electrons, which move in an external circuit to produce electricity. The free Li-ions move back through the separator and into the cathode material. The redox reactions that occur during discharge of a LCO battery can be described by:

$$\mathrm{Li}_x\mathrm{C} \longrightarrow \mathrm{C} + \mathrm{xLi} + \mathrm{xe}^-$$
$$\mathrm{Li}_{1-x}\mathrm{CoO}_2 + \mathrm{xLi}^+ + \mathrm{xe}^- \longrightarrow \mathrm{LiCoO}_2$$

The upper reaction describes the oxidation reaction of the anode, which creates free electrons to produce electric energy. The lower reaction describe the reduction reaction of the cathode, where Li-ions intercalate back into the cathode material to form lithium cobolt oxide.

In the reactions, $x$ represent the amount of Li-ions that are depleted from the cathode during charging, and subsequently produce free electrons. The Li-ions are critical for the mechanical stability of the cathode material, as they contribute to the atomic structure of the cathode. To prevent permanent structural damage of the cathode, $x$ is therefore limited to a value of 0.55 [16]. This limit places great emphasis on the cathode materials that are used in LIBs, as the amount of energy that can be produced rely directly on the magnitude of Li-ions that can be safely stored and removed from the cathode.

To aid electron transport, the cathode and anode materials are coated on thin current collectors, which are made of copper for the anode, and aluminium for the cathode. The current collectors have high electric conductivity and easily attract free electrons to move in the external circuit of the cell.

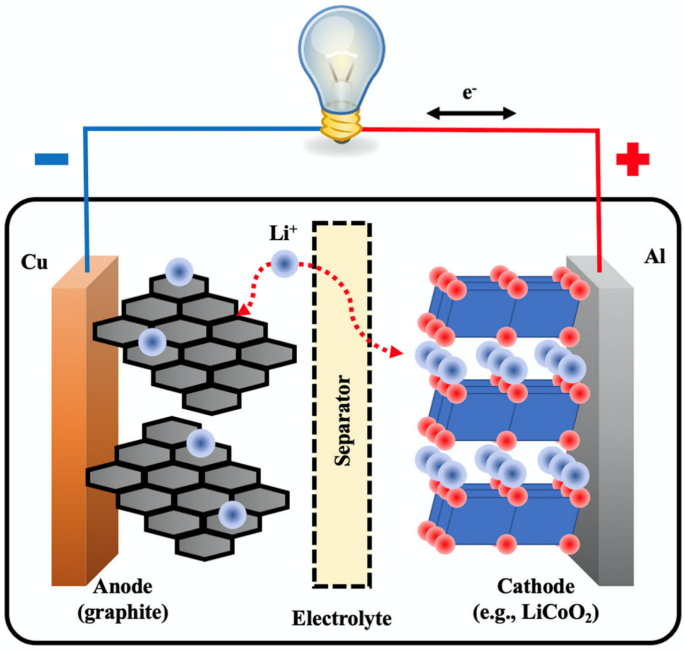


**Figure 2:** Schematic describing the main components of a Lithium-ion battery. During charging the lithium ions deintercalate from the metal oxide of the cathode, moves through the separator, and intercalate into the graphitic structure of the anode. The process is reversed during discharge to produce a flow of electrons in the external circuit. [17].

The specific energy of the battery is highly dependent on the discharge-potential of the cell. This is linked to the electrochemical potential of the oxidation and reduction reactions in the battery, which rely on the chemical composition of the anode and the cathode materials. The operating voltage window for a given battery chemistry sets a limit to the amount of lithium ions that can be repeatedly removed from the cathode without causing structural damage to the material. Selection of anode and cathode materials is therefore critical, as it highly influences the power and capacity characteristics of a LIB battery.

### 2.1.1 Cathode materials

Because of the close relationship between battery performance and cathode chemistry, the topic of cathode materials and structures have been intensively researched. Cathode materials inherit different characteristics when it comes to capacity, operating voltage, cycleability, thermal stability and safety. For instance, nickel rich chemestries give great energy/power characteristics, at the expense of cycleability and thermal safety. Nickel rich cathodes are therefore often doped with Al or Mg to enhance thermal stability and electrochemical performance [18]. When selecting the cathode materials, a trade-off between stability and cycleability versus capacity and power characteristics is often needed.

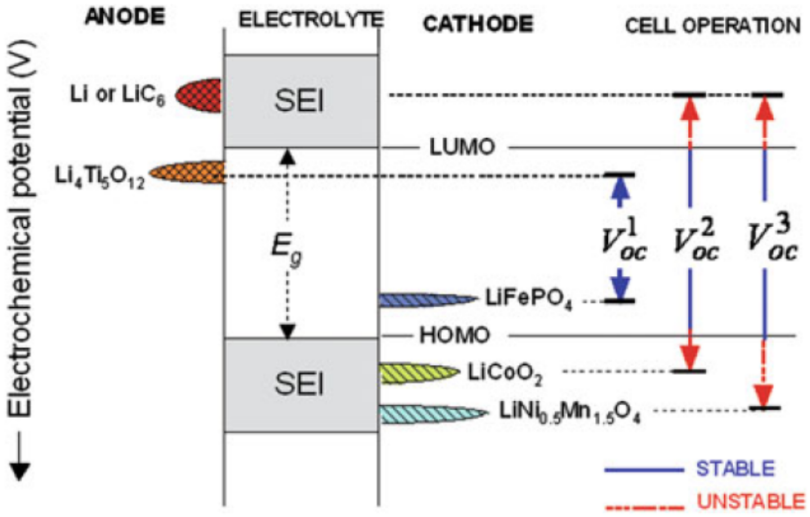


**Figure 3:** Image showing the electrochemical potential of different cathode and anode materials. $E_g$ represents the electrochemical stability window of the electrolyte. Operating outside this voltage range will result in formation of the passive SEI layer, both on the anode an cathode surface. High voltage cathodes operating outside the electrolyte stability window, such as $LiNi_{0.5}Mn_{1.5}O_4$ will suffer from SEI formation. [19].

Cathode chemistries that are often used include lithium nickel cobolt aluminium oxide (NCA), lithium nickel cobalt manganese oxide (NMC), lithium iron phosphate (LFP), and lithium cobolt oxide (LCO).

Lithium cobalt oxide ($LiCoO_2$) was the first commercialised cathode chemistry for lithium-ion batteries, and is made popular due to its high specific capacity and great power characteristics. Main drawbacks for the LCO cathode include high cost and the political and ethical issues involved with cobalt mining. In addition, LCO have relatively low thermal stability, which increase the risk of thermal runaway. Despite these concerns, LCO remain one of the most popular cathode chemistries due to its high discharge voltage ($\sim$ 4V).

Lithium manganese oxide ($LiMn_2O_4$) is another common chemistry because of the low cost and environmentally friendliness of manganese compared to nickel and cobalt. A disadvantage with the LMO chemistry is the observed capacity fade after long term cycling as a result of Mn dissolution and electrolyte decomposition [20]. However, the low toxicity and great safety performance make LMO a considerable choice where long cycle life is not critical for the battery performance.

To increase the structural stability and specific capacity, nickel and cobalt have been added to the LMO chemistry, to create lithium nickel cobalt manganese oxide ($LiNi_xCo_yMn_zO_2$). The chemistry has become popular because of the cost reduction due to lower Co content, while achieving similar power to LCO. The most common mixing ratio for the transition metals is NMC111 ($LiNi_{0.33}Co_{0.33}Mn_{0.33}O_2$), and is used in a variety of applications including electric vehicles. To further increase the specific capacity, Nickel rich NMC chemistries are being explored, which has led to NMC811 ($LiNi_{0.8}Co_{0.1}Mn_{0.1}O_2$). However, these chemistries suffer from capacity fading and low thermal stability compared to NMC111 [21].

As an alternative to NMC, lithium nickel cobalt aluminium oxide ($LiNi_{0.8}Co_{0.15}Al_{0.05}O_2$) is broadly used, due to its high specific capacity. The addition of aluminium in the chemistry improves the thermal stability and electrochemical performance [22]. NCA chemistries still suffer from poor long-term cycle performance, similarly to NMC. Microcracking in the cathode particles have been observed during cycling, which reduce the lifetime of the battery by increasing the cell impedance. By limiting the depth of discharge (DOD), the extent of microcracking can be reduced, at the cost of lower energy density.

Lithium iron phosphate ($LiFePO_4$) have relatively low operating voltage and volumetric energy density compared to other commercialised cathode chemistries. LFP in still a relevant chemistry in applications where long cycle life, high power capacity and high safety level is needed. Due to these characteristics, LFP chemistries are now widely used in ESS applications [23].

Table 1: **Cathode chemistries**

| **Cathode** | **Theoretical Specific Capacity [mAh/g]** | **Experimentally obtained Specific Capacity [mAh/g]** | **Voltage vs. Li/Li+ [V]** | **Sources** |
|---|---|---|---|---|
| LCO ($LiCoO_2$) | 274 | 106.5 - 160<br>180 - 190 (coated) | 3.8 - 4.3<br>4.5 - 4.7 (coated) | [24–29] |
| LMO ($LiMn_2O_4$) | 148 | 120 - 130 | 3.8 - 4.2 | [30–33] |
| NMC111 ($LiNi_{0.33}Co_{0.33}Mn_{0.33}O_2$) | 275 | 155 - 175 | 2.75 - 4.4 | [21, 30, 34–52] |
| NMC811 ($LiNi_{0.8}Co_{0.1}Mn_{0.1}O_2$) | 275 | 200 - 217<br>266 (coated) | <4.0 | [21, 30, 34–52] |
| NCA80 ($LiNi_{0.8}Co_{0.15}Al_{0.05}O_2$) | 279 | 156.6 - 202.5 | 3.7 - 4.2 | [28, 36, 42, 52, 53] |
| LFP ($LiFePO_4$) | 170 | 150 - 170 | <3.75 | [42, 54–58] |

### 2.1.2 Anode materials

The anode material in a LIB should facilitate space-efficient and structured storage for lithium ions, to prevent lithium metal plating and dendrite formation on the anode surface. Dendrite formation is a safety issue that can cause metallic lithium to pierce through the separator and effectively short circuit the cell, which can cause the battery to catch fire. The anode material will also need high electrical conductivity and good transport kinetics for lithium ions. Anode materials can take form of intercalation materials, conversion materials, alloys or lithium metals.

Graphite is the most used anode material, and can be considered an intercalation material. In a graphitic anode, lithium ions intercalate to form $LiC_6$. Graphite can be characterised by its low cost, high availability, low delithiation potential and long cycle life, which have led it to be the dominating anode material for the past decades [59]. Still, the relatively low capacity of graphite ($372\,\mathrm{mAh\,g^{-1}}$) is insufficient to meet the energy density requirements of future batteries. In addition, lithium plating and dendrite formation on the graphite anode contribute to poor lithium ion transport kinetics, which limits the rate capability, especially evident at low temperatures. Graphite anodes also suffer from large volume change during fast charge/discharge cycles, forming unstable SEI layer and causing capacity fading.

Another anode material that have been commercialised, is lithium titanium oxide (LTO). The advantages of LTO anodes include high thermal stability, high rate capability and long cycle life. The operating voltage of a LTO anode is inside the electrochemical stability window of the electrolyte (Fig. 3), which effectively avoids electrolyte decomposition and SEI growth. As a result, the impedance of the SEI layer is removed, which allows for faster lithium insertion and higher rate capability. For the same reason, the common safety issues of graphite anodes including dendrite formation and lithium plating is also absent for the LTO anode. The low volumetric change of LTO during charge/discharge compared to other anode materials, give great cycleability for the battery. The main disadvantage with LTO as anode material is the relatively low specific capacity at ($175\,\mathrm{mAh\,g^{-1}}$). However, LTO can be used in applications where high rate capability and long cycle life is prioritized over energy density.

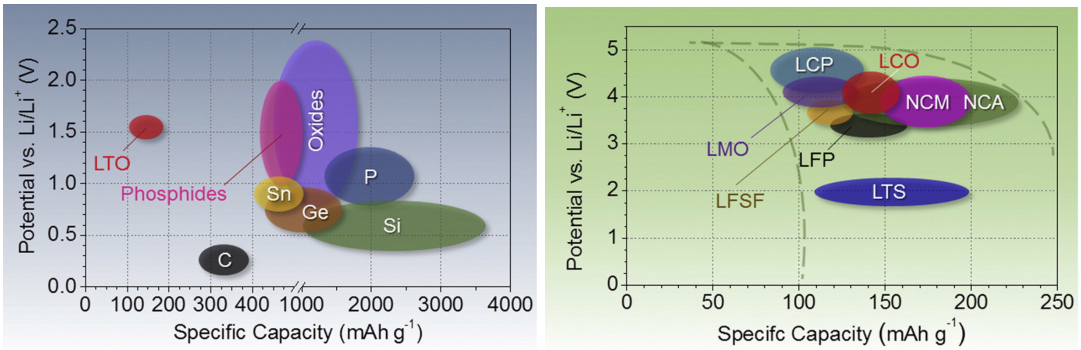


**(a)** **(b)**

**Figure 4:** Schematic overview of the different anode materials (a), cathode materials (b) and their specific capacity and voltages [18].

As an alternative to intercalation anodes, different alloying materials can be used. In alloy-based anode materials, lithium will form an alloy with a metal or metalloid during the lithiation process. A widely used alloy material is silicon. Silicon have a very high specific capacity ($3580\,\mathrm{mAh\,g^{-1}}$), low voltage vs. lithium, low cost and is highly available. Alloy materials suffer from large volumetric expansion during lithiation (up to 300%), which cause damage to the anode structure and decomposition of the SEI layer. To stabilize the anode structure, reduce volumetric expansion, and improve electrical conductivity, carbon particles can be distributed over the silicon oxide surface [60].

In conversion type anode materials, lithium is stored with high capacity through reversible redox reactions with transition metal oxides. The specific capacity for conversion type anodes is higher than intercalation anodes, and can range from 500 to $1000\,\mathrm{mAh\,g^{-1}}$ [60]. The operating voltage of conversion anodes is higher compared to intercalation anodes, making the cell potential lower, which could hinder dendrite growth and SEI formation. Another benefit is the low production cost of conversion type anodes compared to alloy materials, as many of them appear in their natural form ($Fe_3O_4, FeS_2, MnO_2$) [61]. The disadvantages of conversion type anodes are large volumetric expansions, electrolyte decomposition and poor electric conductivity.

Another anode material that have been extensively researched is lithium metal. Lithium metal has high specific capacity and low electrochemical potential. However, lithium metal is prone to dendrite formation during lithiation, which have been the main drawback for this type of anodes. To prevent dendrite growth, research have been made to alter the anode surface and achieve a more uniform distribution of the lithium ions during lithiation [62].

Table 2: **Anode chemistries**

| **Anode** | **Theoretical Specific Capacity [mAh/g]** | **Experimentally obtained Specific Capacity [mAh/g]** | **Voltage vs. Li/Li+ [V]** | **Sources** |
|---|---|---|---|---|
| Graphite | 372 | 350 | 0.05 - 0.2 | [61, 63–65] |
| Titanium<br>LTO $Li_4Ti_5O_{12}$ | 175 | 170 | 1.56 | [61, 63] |
| Silicon<br>Si-Alloys<br>Si-(M)-C | 4200<br>3580 | 3000<br>525 - 3163 | 0.05 - 0.6<br>- | [64, 66] |
| Lithium metal | 3860 | - | 0 | [61, 67] |

### 2.1.3 Electrolyte and separator

In a LIB, a separator and a suitable electrolyte is needed for the battery to function properly. The separator prevents electrical short circuiting between the electrodes. The separator is made up of a porous polymeric membrane that allows for lithium transport between the active material of the anode and cathode. Polypropylene (PP) and polyethylene (PE) are commonly used materials [68]. Separators are important components in terms of the thermal safety of a LIB in operation. The separators should have a shutdown temperature, where the ionic transport through the separator is reduced to inhibit further current flow. This occur by closing the pores of the separator [69]. In addition, the separator should have a high melting temperature exceeding 200°C, to improve thermal stability of the cell. Although the separator is not seen as an active material in a LIB, it has a clear impact on the cell performance by minimising the cell overpotential and assuring uniform porosity and lithium deposition on the anode surface. For lithium metal anodes, modifying the separator might contribute to inhibit dendrite growth during lithiation [51].

The electrolyte in a LIB works to reduce the overall resistance of the cell. In conventional batteries, electrolyte is working as a transport medium for the ions to diffuse through the separator between the electrodes. It is absorbed by the separator and the electrode active material to increase the ionic conductivity. The electrolyte is important in terms of both safety and performance of the battery, because of its electrochemical and thermal stability characteristics. The electrochemical stability window of the electrolyte sets a limit to the operating voltage of a LIB (Fig. 3). Conventional electrolyte solutions is unstable at voltages above 4.3V vs. $Li/Li^+$ [70], which is too low for high voltage LIB batteries. Increasing the electrolyte stability window can therefore increase the operating voltage of the battery, and hence improve energy density.

An important safety issue in LIBs is thermal runaway, which occur when the heat generation rate overcome the heat dissipation rate of the battery. The thermal decomposition of electrolyte is an important contributor to the exothermic reactions of thermal runaway. Therefore, improving thermal stability of the the electrolyte is critical for the safety of the battery.

The most common electrolyte is the lithium salt ($LiPF_6$) dissolved in organic carbonates such as ethylene carbonate (EC), dimethyl carbonate (DEC), diethyl carbonate (DEC), propylene carbonate (PC) or ethyl methyl carbonate (EMC). The electrolyte also play an important role in the formation of a stable SEI layer, which is critical both in terms of battery performance, cycleability and safety. To improve the electrolyte performance, additives can be used to improve SEI formation, thermal stability and enhance safety [71].

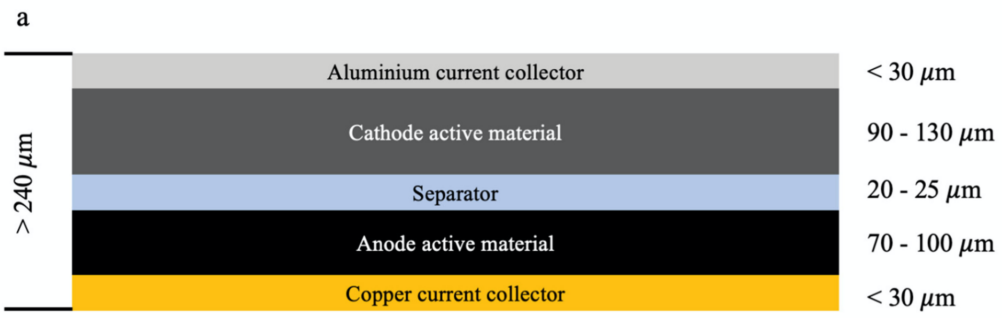


**Figure 5:** Schematic of the physical construction and size of the different components in a LIB [17].

### 2.1.4 Physical properties

To fit the application area of the battery, there exist several different physical constructions of LIBs. The most common physical constructions include cylindrical, prismatic, and pouch cell batteries (Fig. 6). When designing a battery system, the shape and size of the cell should be considered to fit the mechanical and thermodynamic requirements of the system. Small cells have

better heat dissipation characteristics, and provide more uniform charge/discharge of the electrodes. Large cells have greater volumetric and gravimetric capacity, because a grater amount of the total volume or mass consist of active material that provides charge. Large cells however produce a significant amount of heat that can be unevenly distributed, which leads to non-uniform degradation processes that decrease SOH [5][72]. Cylindrical cells have an efficient and well established manufacturing process that reduce the production cost. Pouch cells require additional costs in cutting and compound assembly, but benefit from less packaging costs. Prismatic cells are more difficult to assemble because of the careful insertion of the wound compound into the outer hard casing [73]. Overall, the productions cost of cylindrical and pouch cells are lower compared to prismatic cells. The shape and construction of the cell also influences the energy density on both cell and module level. Pouch cells are superior to prismatic and cylindrical cells in terms of energy density, due to the low weight of the battery housing. Pouch cells can also be stacked more space efficient, which further increase the energy density on a module level. However, pouch cells are considerably more fragile and therefore need more protection when used in a battery system.

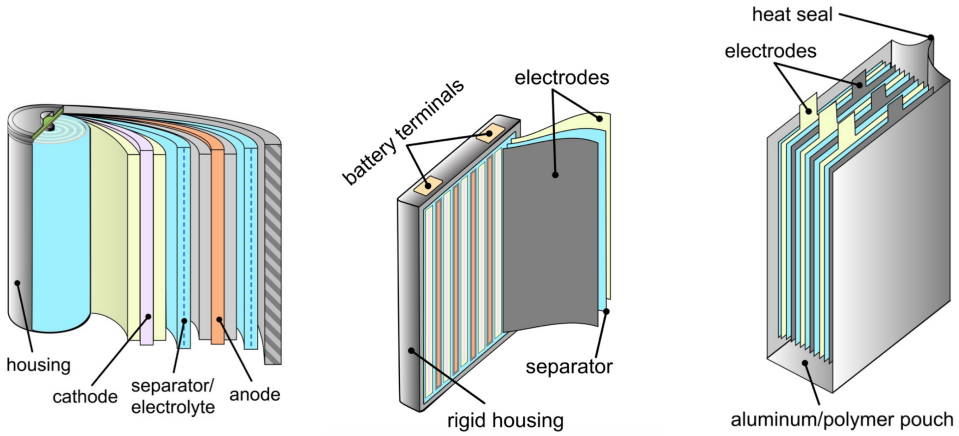


**(a)** Cylindrical cell **(b)** Prismatic cell **(c)** Pouch cell

**Figure 6:** Schematic showing different physical constructions of LIBs [74].

## 2.2 Thermal behavior of LIBs

The thermal behavior of a LIB influenced by both the operation and mechanical properties of the battery. The extent of heat generation in the battery is dependent on the rate of the chemical reactions that occur during charge and discharge, as well as the internal impedance inside the battery. Choice of battery material and packing greatly influence how heat is distributed inside the cell as well as to the surrounding environment. This section will go through the theory of how heat is produced and dissipated in LIBs.

### 2.2.1 Heat generation

In operation, heat is generated inside the battery during charge and discharge, and subsequently dissipated to the surroundings. The magnitude of produced heat relates to the resistance to movement of the ions and electrons inside the cell. The internal resistance is dependent on the charge/discharge rate, State of Charge (SOC), State of Health (SOH), temperature and material properties of the battery. Heat generation in a LIB can be divided into irreversible or reversible heat generation. The reversible reaction heat results from the entropy change of the chemical reactions inside the battery. Reaction heat is dependent on SOC, and is exothermic or endothermic as the battery is charging or discharging, respectively. The irreversible heat is the dominant heat source at higher C-rates, and is a result of the internal resistance of the battery [75]. The irreversible heat can be described by:

$$Q_\eta = \eta_{battery} \cdot I \tag{1}$$

or alternatively

$$Q_\eta = I^2 \cdot R \tag{2}$$

In the last equation, $R$ represent the total internal battery resistance. It is clear that that the internal resistance is an important contributor to the heat production in the battery, and should therefore be minimised. In Eq. (1), $\eta_{battery}$ is the battery overpotential and $I$ is the current density. The overpotential is the difference between the electromotive force and the voltage at the terminals of the cell:

$$\eta_{battery} = E_{battery} - E^{eq}_{battery} = \eta_{ct} + \eta_{el} + \eta_d + \eta_{ohm} \tag{3}$$

In LIBs the battery overpotential can be seen as a measure of the cell efficiency. The overpotential is made up of several thermodynamic losses that have different contributions at different SOC. The different contributions to the battery overpotential include processes linked to charge transfer at the electrodes ($\eta_{ct}$), diffusion and migration of Li-ions in the electrolyte ($\eta_{el}$), diffusion and migration of Li-ions in the electrodes ($\eta_d$) and the ohmic losses ($\eta_{ohm}$) [76–78].

The reversible entropic heat generation can be described by:

$$Q_s = -I \cdot \frac{T \cdot \Delta S}{n \cdot F}$$

where $F$ is the Faraday constant, and $\Delta S$ is the entropy change. The irreversible heat generation is dominant at high C-rates, however the entropic heat generation can be significant in some situations and should be included in the thermodynamic model of the battery [76]. The total internal heat generation in the battery can therefore be described by:

$$Q_{in} = Q_\eta + Q_s \tag{4}$$

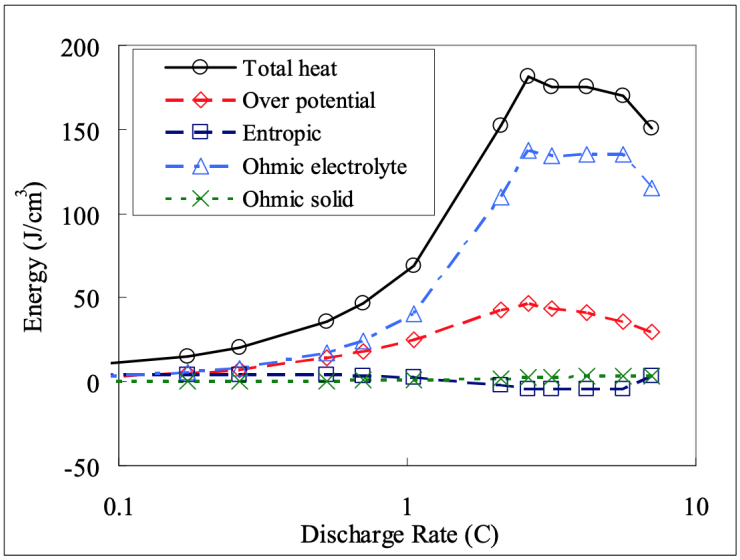


**Figure 7:** Schematic of contributions from various heat sources in a LIB with different current rates. At higher current rates, the overpotential and ohmic heat becomes dominant, while the entropic heat is negligible [79].

### 2.2.2 Thermal conduction

The internal distribution of heat inside the battery is determined by the conductive properties of the battery materials. The conductive heat flux can be described by Fourier's law:

$$\mathbf{q} = -k \cdot \nabla T \tag{5}$$

where $k$ is the conductive heat transfer coefficient and $\nabla T$ is the temperature gradient. The temperature gradient can be written out to evaluate the three dimensional heat flux:

$$\mathbf{q} = -\left(k_x \frac{\partial T}{\partial x} + k_y \frac{\partial T}{\partial y} + k_z \frac{\partial T}{\partial z}\right) \tag{6}$$

Studies have shown that the conduction heat transfer is around an order of magnitude larger in the in-plane compared to the cross-plane direction [27]. Similar results have been shown for cylindrical cells, as the conductivity is larger axially, compared to radially. The reported conductivity in LIBs vary in literature, from measurements of 20 to 35 W/mK in the axial and in-plane direction, compared to 0.15 to 1.4 W/mK in the cross plane direction [80]. It is of interest to improve the low thermal conductivity in the cross plane direction in order to achieve a more uniform cell temperature, especially at higher current rates.

The battery is constructed of several stacked layers of electrodes, current collectors and separators. The thermal conductivity is therefore considered anisotropic. To account for the conduction properties of the different layers of material, the use of an effective heat transfer coefficient may be used. In the cross plane direction, the conductive heat transfer coefficient can be evaluated by [27, 81]:

$$k_{eff} = \frac{d_{total}}{\Sigma \frac{d_i}{k_i}} \tag{7}$$

where $d_{total}$ is the total thickness of the battery, $d_i$ is the thickness of the battery components, and $k_i$ is the thermal conductivity of the battery components. Fig. 8 shows how the use of isotropic and anisotropic conductivities in thermal modeling can impact the heat distribution of a cylindrical cell. It is clear from the figure that the high axial conductivity leads to a more uniform temperature distribution in the cell. To improve the rate at which heat is transported from the centre of the cell to the surroundings, it is important to strive for a high thermal conductivity in the battery components. High conductivity will reduce the temperature gradients inside the cell, which can lead to nonuniform battery degradation [82].

### 2.2.3 Thermal dissipation

Thermal dissipation is the process where heat is transported from the surface of the battery to the ambient air. Controlling the dissipation rate is an important aspect of thermal management, in order to optimise battery temperature and ensure safe operation of the battery pack. Dissipation can be split into heat transfer by convection and radiation. The convection heat transfer can be described by newtons law of cooling:

$$Q_{convection} = h \cdot (T_s - T_\infty) \tag{8}$$

where $h$ is the convection heat transfer coefficient, $T_s$ is the temperature of the battery surface area and $T_\infty$ is the temperature of the air surrounding the battery. The value of $h$ is influenced by the flow conditions (air velocity or free convection), air temperature and density, and surface geometry of the battery. These parameters should be modified so that the battery is operated within the optimal temperature range.

The radiative heat transfer is also part of the heat dissipation from the battery. Thermal radiation does not require a transport medium for heat transfer to occur, in contrast to convection and conduction heat transfer. The radiative heat transfer can be described by:

$$Q_{radiation} = \varepsilon\sigma(T_s^4 - T_\infty^4) \tag{9}$$

where $\varepsilon$ is the emissivity of the battery outer surface ($0 \leq \varepsilon \leq 1$), $\sigma$ is the Stefan Boltzmann constant ($\sigma = 5.67 \times 10^{-8} W/m^2 \cdot K^4$), $T_s$ is the temperature of the battery surface and $T_\infty$ is the temperature of the surroundings. The radiative heat transfer can be improved by altering the outer surface of the battery, and thereby changing the emissivity [83]. The total heat transfer from the battery surface to the surroundings can be described by:

$$Q_{out} = Q_{convection} + Q_{radiation} = h \cdot (T_s - T_\infty) + \varepsilon\sigma(T_s^4 - T_\infty^4) \tag{10}$$

As can be seen from the above equation, the dissipation is a function of both the convection and radiation heat transfer. In operation, the relative contribution from the radiation and convection heat transfer can vary, depending on the battery temperature, flow of air and ambient temperature. For especially high temperatures, the heat dissipation by radiation can overcome the heat dissipation by free convection [84]. However, the radiative heat transfer is rarely large enough to cool the battery pack in use. Therefore, cooling by forced convection is commonly integrated as a part of the thermal management system.

### 2.2.4 Thermal balance and modeling

The temperature of the battery can be determined by solving the thermal balance of the battery. The thermal balance is the relationship between the generated heat inside the battery and the heat dissipation to the surroundings. A simple heat balance of a LIB can be described by:

$$m \cdot C_p \cdot \frac{dT}{dt} = Q_{in} - Q_{out} \tag{11}$$

where $m$ is the mass of the battery, $C_p$ is the specific heat capacity of the battery, $Q_{in}$ is the internal heat generation and $Q_{out}$ is the dissipated heat. This is called a lumped capacity model, as the temperature inside the battery is considered uniform. The lumped capacitance model is simple and requires a small amount of computational resources to solve, however it have limited relevance for battery packs with large temperature gradients and anisotropic conductivities. To reach acceptable accuracy for such models, the Biot number of the battery should be smaller than 0.1:

$$Bi = \frac{hL_c}{k} < 0.1 \tag{12}$$

where $L_c$ is the characteristic length, given by the ratio of the solid's volume to cooled surface area $L_c = \frac{V}{A_s}$. At small Biot numbers, the rate of heat conduction inside the battery is high compared to the surface cooling of the battery. This can be the case for small battery cells. However, in many cases, high volume battery cells that is subject to significant convective cooling effectively makes the model inapplicable.

A more comprehensive thermal model can be obtained by considering the internal temperature of the battery in all three dimensions:

$$\rho C_p \frac{\partial T}{\partial t} = \frac{\partial}{\partial x}\left(k_x \frac{\partial T}{\partial x}\right) + \frac{\partial}{\partial y}\left(k_y \frac{\partial T}{\partial y}\right) + \frac{\partial}{\partial z}\left(k_z \frac{\partial T}{\partial z}\right) + q_{in} \tag{13}$$

Where $q_{in}$ is the volumetric heat generation intensity. The thermal conductivity, $k$, the density, $\rho$, and the specific heat capacity, $C_p$ is now location dependent. Similarly to the effective conductive heat transfer coefficient given by (7), the effective thermal capacity of the battery can be found by:

$$\rho C_p = \frac{\sum_i \rho_i C_{p,i} V_i}{\sum_i V_i} \tag{14}$$

The boundary conditions for the outer surface of the battery can be obtained by the following equation:

$$-k\frac{\partial T}{\partial n} = h \cdot (T_s - T_\infty) + \varepsilon\sigma(T_s^4 - T_\infty^4) \tag{15}$$

where $n$ represent the direction perpendicular to the boundary surface. The three dimensional energy equation (13) can be solved and validated with the boundary conditions given by (15), by obtaining specific battery parameters through experiments. However, the computational cost related to this is high, and is not well suited for real time monitoring of the battery temperature. The use of effective thermal capacities and conductivities as given by Eq. (7) and Eq. (14) will lower the amount of computations.

### 2.2.5 Thermal gradients

In operation temperature gradients will develop inside the LIB due to the internal heat generation and relatively low thermal conductivity of the battery. This is especially evident at higher C-rates, as heat is generated faster than it is dissipated to the surroundings. The development towards high volume energy dense cells with large amount of active material give larger temperature gradients, because of the higher internal resistance [85]. To compensate for the internal heat generation, intensive cooling from the thermal management system is needed. This is often done through convection cooling on the surface of the battery, which in turn creates larger temperature gradients between the surface and the inside of the cell (Fig. 9). As the battery kinetics is largely dependent on the operating temperature, the temperature gradients will contribute to local degradation processes on the electrodes of the battery. This is because the rate of the chemical reactions in a battery have been shown to follow the Arrhenius law - increasing with increasing temperature [86–88]. This in turn leads to enhanced Li-ion intercalation rates in areas with high temperature, which creates local SOC differences at the anode. The local SOC differences cause acceleration of local degradation processes, and therefore aging of the battery [89]. aging of the battery caused by thermal effects is therefore not limited to the temperature itself, but also the internal temperature distribution of the battery.

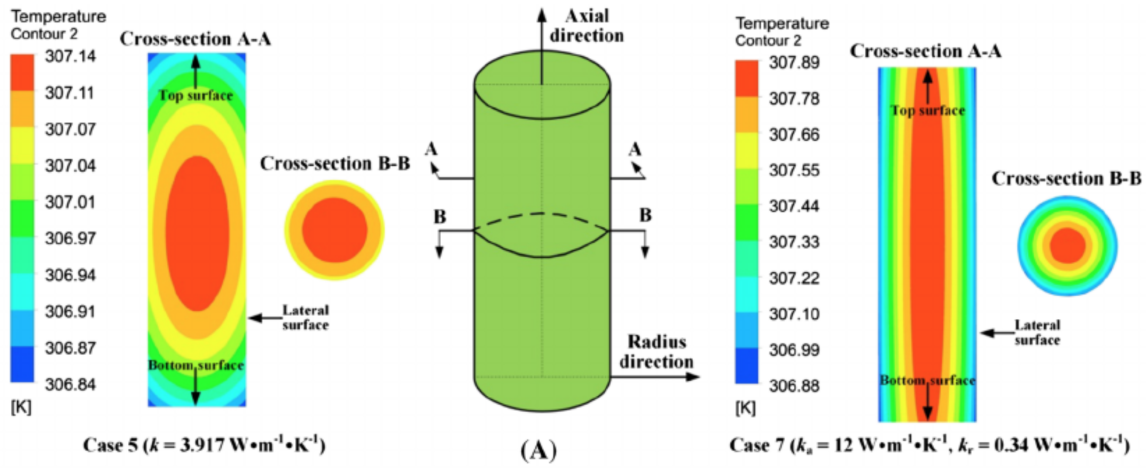


**Figure 8:** Thermal modeling of a cylindrical LIB using isotropic (left) and anisotropic conductivities (right) [27].

### 2.2.6 Thermal management

In all battery systems, a battery thermal management system (BTMS) in needed to ensure safe and optimal temperature of the LIBs in use. The BTMS should work to achieve a uniform temperature distribution of the LIBs, in order to avoid the undesirable aging mechanisms caused by internal temperature gradients. The common BTMS is mainly focused on cooling of the battery pack to remove excess heat, although heating in cold ambient temperatures is also essential for optimal operation of the battery pack. The cooling methods can be divided into air or liquid cooling, internal or external cooling, passive cooling with use of phase change materials (PCM) or hybrid cooling methods. Among these, external cooling by air convection have been popular, because of its low cost and simplicity. The efficiency of this method is however limited, because of the low thermal conductivity and heat capacity of air. Systems based on liquid cooling can be used to improve he heat transfer efficiency. By circulation of a cooling medium such as water or glycol, a large amount of heat can readily be absorbed.

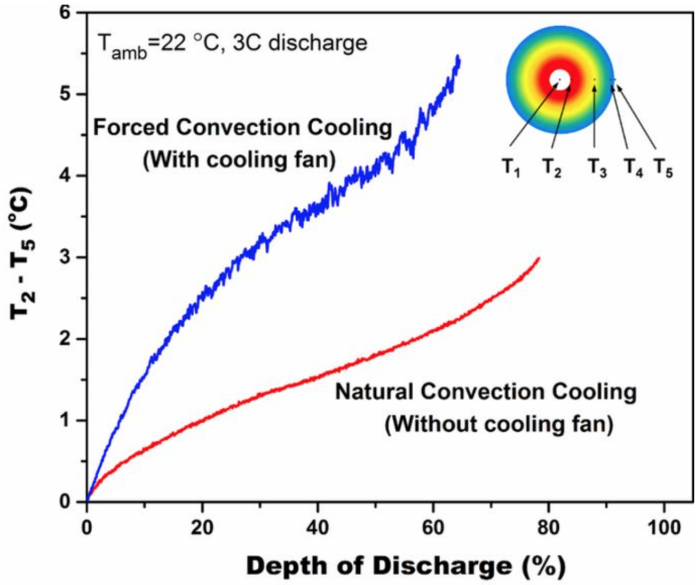


**Figure 9:** Plot of radial temperature gradient as a function of DOD in a cylindrical cell at a rate of 3C [90].

Liquid based cooling systems can be divided into direct contact, indirect contact and heat pipe systems. Direct contact systems work by submerging the battery in a dielectric heat transfer fluid to absorb the generated heat. The cooling efficiency of these systems is high, but the heavy weight and impractical implementation is a disadvantage. In indirect contact systems, the heat transfer fluid is guided through channels between the batteries to absorb heat. The channels can take form of plates or tubes that are placed adjacently to the battery surface. Heat pipe systems take advantage of the large heat transfer associated with the phase change of a circulating fluid to both absorb and reject heat. The flow of fluid inside the pipes is regulated by pressure gradients that evolve during evaporation and condensation of the circulating fluid. Wang et al. [91] showed that the heat pipe systems successfully can be used in EVs for thermal management. An alternative to liquid based cooling methods is systems based on phase change materials. In PCM based systems, heat is absorbed at constant temperaure to induce a phase change in the material that is surrounding the battery (Fig. 10). The PCM can absorb large amount of heat at a constant temperature, which creates a uniform temperature distribution of the batteries. The amount of heat that can be absorbed by the PCM before it is fully melted is however limited. Therefore, to provide a continuous heat absorption, a coupling between the PCM and an external cooling system can be advantageous [92].

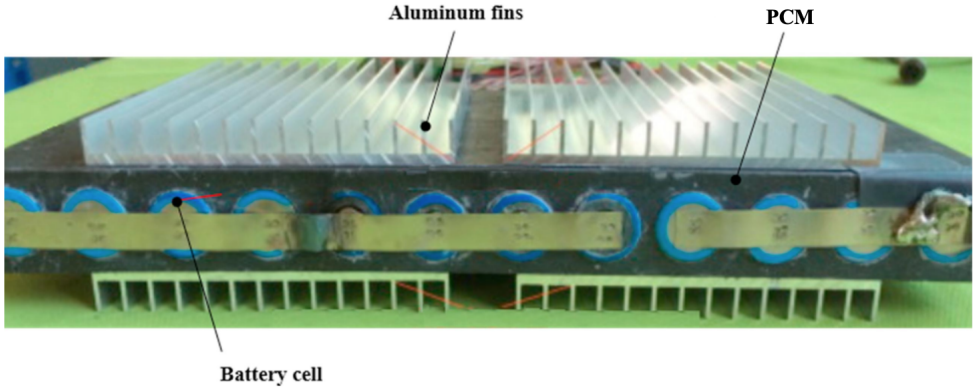


**Figure 10:** Schematic of a PCM system applied over a battery pack of cylindrical cells [93]. Cooling fins are attached to the PCM to increase heat transfer rate.

A good BTMS should also have the ability to provide heat to the battery in cold ambient conditions, to avoid the negative effects that are observed in LIBs at lower temperatures. The heating methods that have been proposed include use of PCM, alternating currents, convective heating, internal self heating or liquid heating [94]. In a study performed by Yang et al. [95], internal self heating with the use of a nickel foil could effectively eliminate the problem of lithium plating at lower temperatures (Fig. 16).

## 2.3 Thermal effects on aging and performance

It is well documented that temperature have a significant impact on the performance and aging processes in a LIB. In addition, controlling the temperature is essential to avoid safety issues including thermal runaway and dendrite formation. The optimal operating temperature of a LIB is shown to be in the range of 15°C-35°C [96], although some variations may occur in the different battery chemistries.

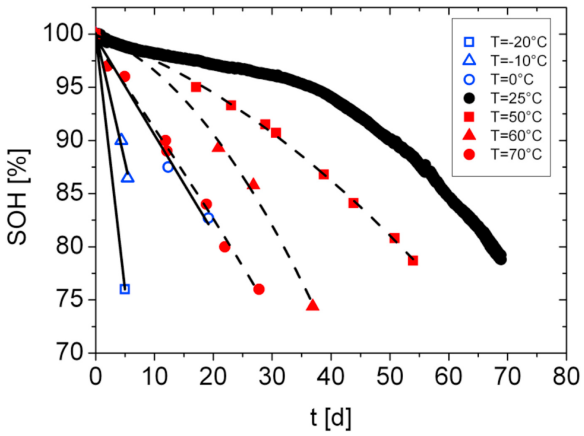


**Figure 11:** Plot of SOH curves as a function of time for cycling at different temperatures and a rate of 1C. Excessive decrease in SOH is evident for both high and low temperatures [97].

### 2.3.1 Temperature and battery performance

The temperature of the battery have a large impact on the battery performance both in terms of rate capability and specific capacity. A significant decrease in the capacity of a LIB is observed already when lowering the temperature from 20 to 15°C, and is even more extensive at lower temperatures (Fig. 12). In addition to loss of capacity, low temperatures is linked to poor intercalation kinetics, especially at the carbon anode surface, which cause a lowered rate capability especially during charging. At higher operating temperatures, an increase in capacity and rate capability is observed, although as explained later in this section, battery degradation rates is also higher at elevated temperatures.

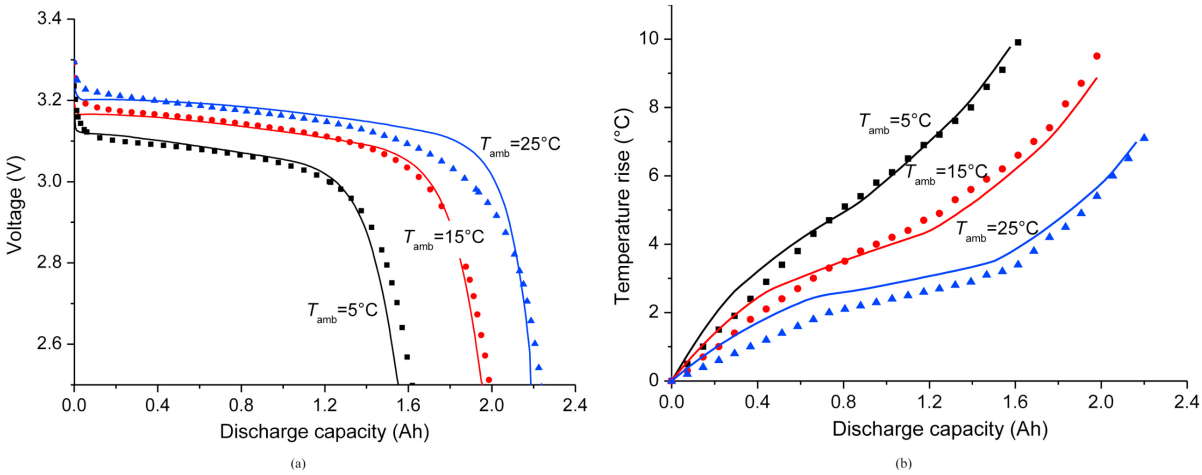


**Figure 12:** Experimental (dotted) and numerical simulations (solid line) for discharge capacity of a $LiFePO_4$ battery at different temperatures. The loss of capacity and reduced discharge voltage at lower ambient temperatures is evident. [98].

The poor low temperature performance have been linked to low ionic conductivity of electrolyte at lower temperatures, reduced lithium diffusion in graphene layers, and an elevated charge transfer resistance at the surface of the graphite anode/SEI layer [99]. All of the above mechanisms is though to reduce the battery performance at lower temperatures.

At low temperatures the lithium concentration on the anode surface increases, which elevates the risk of lithium plating and subsequent dendrite formation that can short circuit the battery [56].

During charging of LIBs in cold temperatures, the current rate is therefore reduced to maintain safe battery operation. This sets a limit for the further implementation of electric vehicles in colder climates, as charging time increases rapidly.

At higher operating temperatures, the negative effects of low temperature operation is avoided, although other issues regarding the safe operation of the battery is evident.

### 2.3.2 Aging and degradation

The temperature of a LIB is also affecting the extent and rate of the degradation processes inside the battery. This is observed during charging/discharging, as well as when the battery is at rest. At high temperatures, the rate of the chemical side reactions inside the LIB increases, which accelerate the degradation processes and shorten the lifetime of the battery. The aging mechanisms that occur at elevated temperatures is complex, and related to the chemical reactions in both the electrolyte and the active material of the battery.

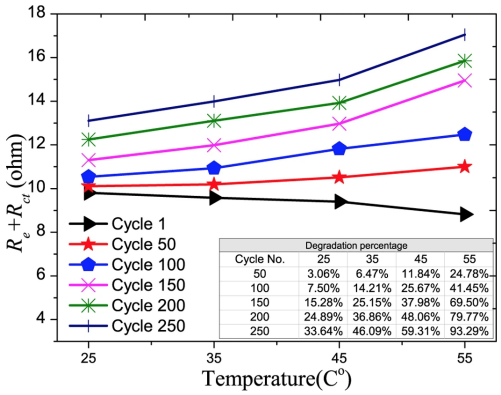


**Figure 13:** Cycle aging at different temperatures and corresponding resistance increase. [98].

A well known aging mechanism in a LIB is the continuous growth and decomposition of the SEI layer on the surface of the graphite anode. The SEI layer is created during the formation stage of the battery production, to prevent exposure between the lithiated anode surface and the electrolyte. The electrolyte is reductively decomposed upon contact with the lithiated carbon of the graphite anode, which cause SEI formation (Fig. 3). The process of forming a stable SEI layer is important to prevent further reaction between the graphite anode and electrolyte in the lifespan of the battery. However, at elevated temperatures, degradation of the SEI layer is apparent, which cause further electrolyte decomposition and loss of lithium ions (Fig.14). Also during charging, the volumetric expansion of the anode upon lithiation can cause cracks in the SEI layer which expose new carbon anode material to the electrolyte. The decomposition and subsequent growth of the SEI layer negatively affect both the capacity and performance of the LIB due to loss of lithium ions and increased cell impedance [100]. The rate at which the SEI layer is formed is showed to follow the Arrhenius equation, thus increasing with temperature [101]. Therefore, to prevent the negative aging effects of excessive SEI formation, the temperature should be kept within the optimal temperature range.

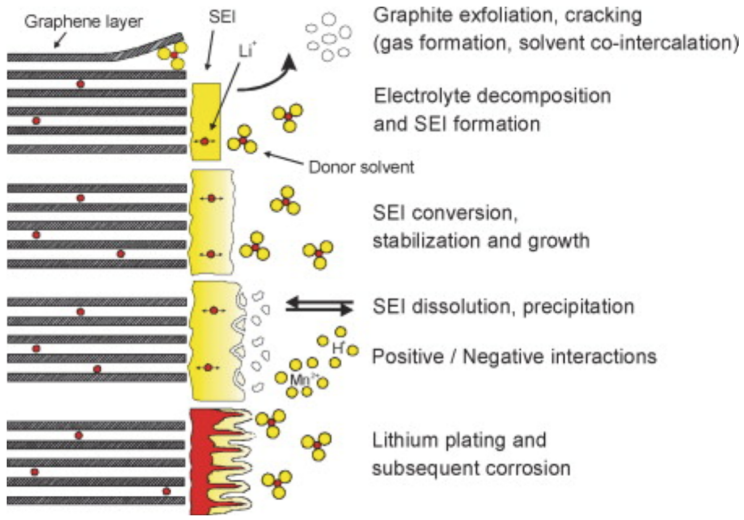


**Figure 14:** Schematic overview of the different aging mechanisms at the anode/electrolyte interface. At elevated temperatures, the degradation rate of the SEI is higher. The subsequent rebuild of the SEI cause depletion of Li-ions in the battery. At lower temperatures, poor diffusion rates in the graphite anode cause lithium plating at the anode surface [77].

The degradation rate of the LIB is highly dependent on both temperature and the materials that are used in the battery. For different cathode chemistries, the degradation rate when exposed to higher temperatures can be highly variable. Fig. 15 shows the temperature dependent aging rate for different cathode materials. The figure shows the number of cycles needed to reach a certain SOH at an elevated temperature, relative to the cycles needed at 15 or 25°C. The negative slope indicates that the cycles needed to reach a certain SOH is reduced as the temperature increases.

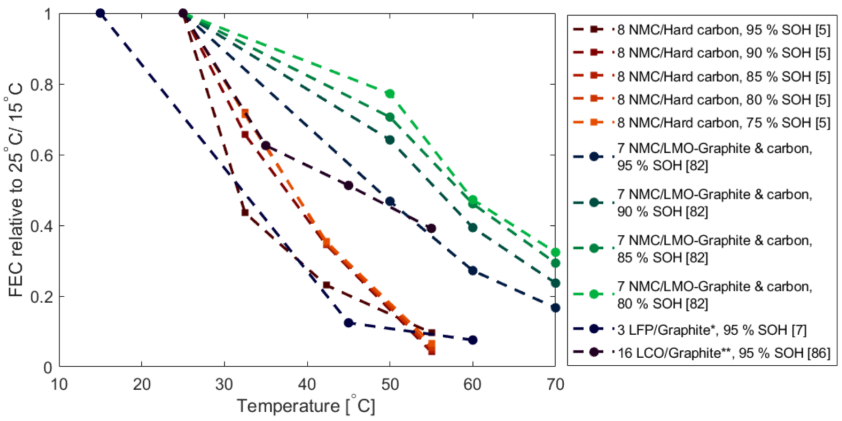


**Figure 15:** Temperature sensitivity and aging rate for different battery chemistries. Capacity fade is observed during cycling at increased temperature, as the number of fully equivalent cycles (FEC) needed to reach the specified SOH decreased. In these results, NMC/Hard carbon chemistry showed greater temperature sensitivity compared to NMC/LMO. [102]

The rate of degradation mechanisms in a LIB is also increased as the temperature go below the recommended operating range. The most important aging process at low temperatures is lithium metal plating. The risk of lithium plating is increased by poor lithium diffusivity into the graphite anode and high charging rates at low temperature (Fig. 14) [103]. Lithium plating cause a decrease in capacity, as some Li-ions are lost irreversibly in the process, and are subsequently unavailable for charge transport in the battery [104]. Therefore, lithium plating is causing both an immediate decrease in capacity and charging rate, and long term decrease in capacity due to loss of lithium.

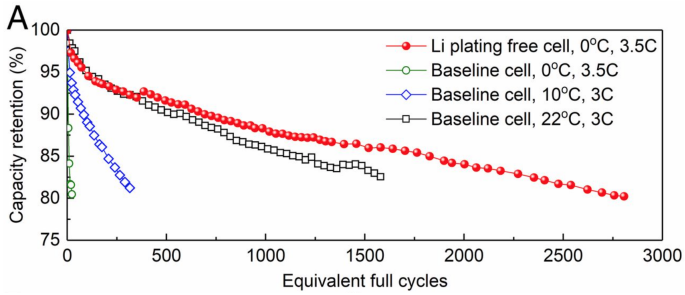


**Figure 16:** Cycle aging at different temperatures. The cell that represents the red dotted line, was heated internally with a nickel foil to prevent lithium plating. The other cells, which were not heated, showed significant capacity decay in comparison [95].

### 2.3.3 Safety issues

In addition to performance decrease and accelerated aging by temperature, there are also safety concerns linked to thermal abuse of a LIB. A well known hazardous safety issue in LIBs is thermal runaway. It can be induced by different abuse conditions, including electrical, mechanical and thermal abuse. The abuse conditions may cause an internal short circuit of the battery followed by a rapid temperature increase. If temperature is elevated sufficiently above the recommended range ($\approx 60°C$), the rate at which temperature is accumulated in the battery can overcome the rate of self heat removal, resulting in a series of exothermic reactions that can cause the battery to catch fire or explode.

For low temperature operation, the most severe safety issue is dendrite growth due to lithium metal plating. It can be caused by overcharging the battery at low ambient temperatures. As described in Sec. 2, the resulting dendrite formation can pierce through the separator and cause an internal short circuit that induce thermal runaway of the cell [56, 105]. The safety issues at different temperatures in a LIB are summarised in Fig. 17. The figure shows how lithium plating is the dominant safety issue at low temperatures, while SEI decomposition and thermal runaway are dominating at higher temperatures.

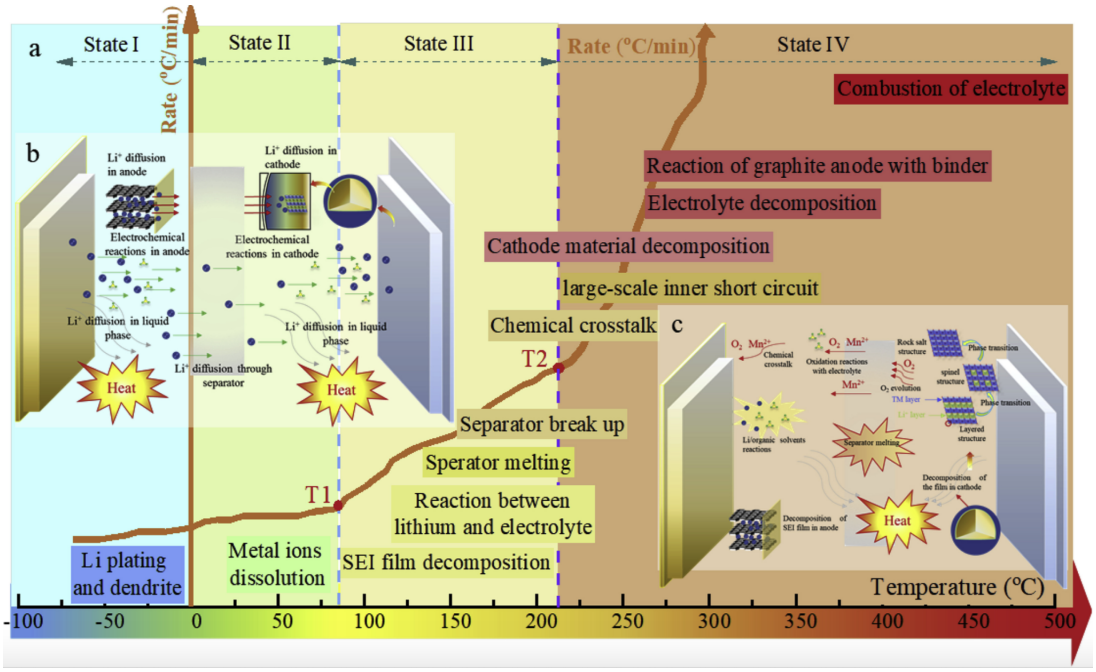


**Figure 17:** Schematic showing the different thermal hazards of a LIB at different operating temperatures. [105].

To summarise, the influence of temperature on performance and degradation of the battery is substantial in both hot and cold climates. The growth and decomposition of SEI layer is dominating at high temperatures, while lithium plating and performance decrease is significant at low temperatures. The operation of LIBs outside the optimal temperature range is therefore highly dependent on effective thermal management, in order to enable high performance, safe operation and long lasting battery packs.

## 2.4 Light properties

This section will provide a theoretical background of light properties and interactions with materials to enable better understanding of the working principle of fiber optical sensors.

### 2.4.1 Light wave properties

Depending on the situation, light can in some instances best be described by electromagnetic waves, while in other situations light is better described as particles.The basic properties of light waves are amplitude, frequency and phase, while light particles (photons) can be characterised by momentum or energy that is determined by frequency [107].

When light is considered a electromagnetic radiation, its properties include an electric and magnetic component. As light is propagating in different dielectric materials, a polarization is induced in the media caused by electron movement from the electromagnetic field. Electromagnetic optics is the study of the interactions that can be observed between light, polarization and charges in different materials. The resulting change of light properties from an external stimuli can be measured, and sets the basis for optical sensors. The electromagnetic spectrum defines the range of frequencies and corresponding wavelengths of electromagnetic radiation.


**Figure 18:** The electromagnetic spectrum [107].

Fig. 18 shows the particular range of the electromagnetic spectrum that is used in optical sensors. The interactions between light and material is varying with the different wavelengths, which is a useful property when it comes to optical sensing.

### 2.4.2 Basics of optical fibers

Fiber optical sensors are based on light propagation through the core of an optical fiber. An optical fiber is constructed of a core, surrounded by a cladding and a protective coating. The physical construction of the fiber is shown in Fig. 19. The core of the fiber is made of a dielectric material, commonly silica, and have a diameter of 8-50 µm. The core allows for light propagation over long distances with minimal attenuation. The majority of light is propagating through the fiber core. Surrounding the core is a layer of glass or plastic cladding with a diameter of 125 µm. The cladding contains light propagation within the core of the fiber, in addition to adding mechanical strength. The outer layer of a fiber consist of a plastic coating, which adds an additional protective layer for the fiber.

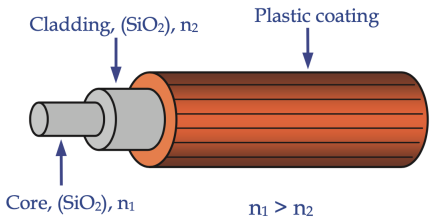


**Figure 19:** Physical construction of an optical fiber. The lower refractive index of the cladding compared to the core facilitates light propagation in the core of the fiber [108].

To enable light propagation over long distances, it is important to minimise the light attenuation in the core of the fiber. In optical fibers, light is contained in the core of the fiber by altering the refractive indexes (RI) of the cladding and the core. The refractive index describes the velocity of light propagation through a material, with respect to the speed of light. It can be expressed as:

$$n = \frac{c}{v} \tag{16}$$

where $c$ is the speed of light in vacuum, and $v$ is the phase velocity of light in the medium. A lower RI gives a higher phase velocity in the material. In an optical fiber, light propagation is retained in the core of the fiber through the concept of total internal reflection, which is achieved when the RI of the cladding is sufficiently low compared to the RI of the core (Fig. 19).

The refractive index also determines the angle of refraction in the transition from one medium to another. The refraction of light at the interface of two materials is described by Snell's law:

$$\frac{\sin\theta_1}{\sin\theta_2} = \frac{v_1}{v_2} = \frac{n_2}{n_1} \tag{17}$$

where $\theta_1$ is the called the angle of incidence, and $\theta_2$ is the angle of refraction (Fig. 21a). The ratio between the refractive indexes of the two materials determine the angle of refraction. If the angle of incidence is sufficiently large, the ray will however be reflected at the boundary, and is thus unable to reach the second medium. This is achieved when the angle of incidence is larger than the critical angle ($\theta_c$), and can be obtained from Snell's law:

$$\theta_c = \arcsin\left(\frac{n_2}{n_1}\right) \tag{18}$$

If the angle of incidence is exactly equal to the critical angle, the light will propagate along the boundary between the two media (Fig. 21b).

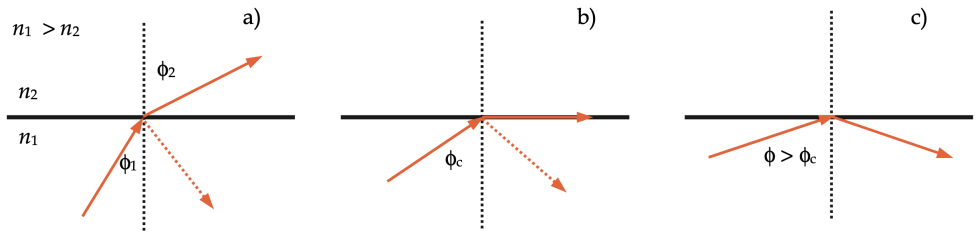


**Figure 20:** Refraction at different angles [108].

As can be observed from Fig. 21a, a portion of light is reflected at the interface between the two media although the angle of incidence is lower than the critical angle. This phenomenon, called

the Fresnel reflection, is utilised in fiber Bragg gratings, as the wavelength of the reflected light is measured.

Optical fibers can be characterised by the number of light modes that are propagating through the core of the fiber. Single-mode fibers are restricted to a single light mode, whereas multi-mode fibers allow several distinct light modes to propagate in the fiber core. The core of the multi-mode fiber is typically larger than the single-mode fiber, with a diameter of 50-200µm.

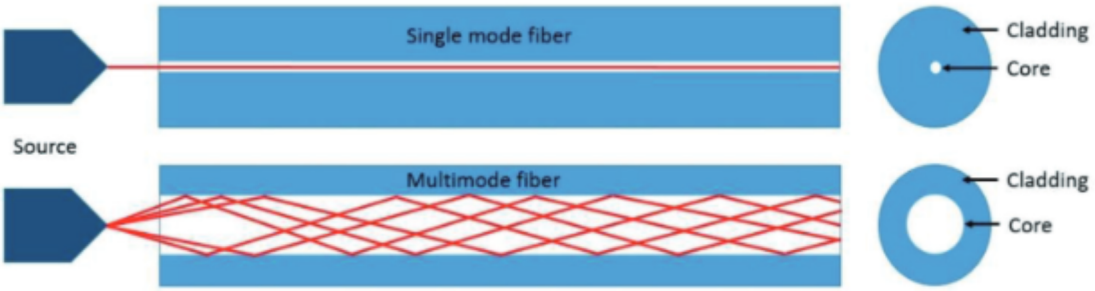


**Figure 21:** Light modes propagating in a multi-mode optical fiber, and a single mode fiber [109]. The majority of the light modes are contained in the core of the fiber through TIR. Some light propagates into the cladding and is terminated.

## 2.5 Optical fiber sensors

Optical fiber (OF) sensors have a wide range of applications. The combined characteristics of long range remote sensing, high sensitivity and physical robustness make OF sensors a reasonable choice in several usage areas [107]. OF sensors are chemically inert, which enable usage in chemically aggressive environments, such as in LIBs. In addition, OF sensors enable remote sensing without supply of electricity, and are immune to electromagnetic interference, which enable sensing in high-voltage environments.

The quantities that can be measured using OF sensors include temperature, strain, pressure, electric and magnetic fields and chemical concentrations. The measurements is based on changes in light properties including phase, polarization, amplitude, intensity and wavelength. Optical sensing is based on light transmittance from an optical source, perturbation of light properties through outer stimuli (temperature, stress, etc.) and detection of the modulated light signal.

Lasers and LEDs is often used as the optical source, whereas the optical fiber works as the transducer that is exposed and respond to an outer stimuli. A photodetector is used for detection of the perturbed signal. A typical setup for an OF sensor is showed in Fig. 22.

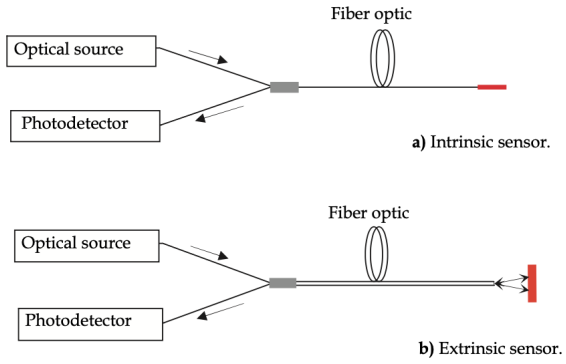


**Figure 22:** a) Optical sensing with intrinsic sensor and b) extrinsic sensor [108].

Optical fiber sensors can be divided into intrinsic and extrinsic sensors. In intrinsic sensors, the fiber work both as a signal transmitter and a transducer. The change of light properties that is measured is a result of changes in the fiber itself. Fiber Bragg gratings are considered intrinsic sensors. In extrinsic sensors, optical fibers are used only as transmitters to the sensors that respond to the measured quantity. The sensor can be either optical or electric, in which an optical transmitter is used to convert the measurements to a light signal. The use of optical fibers for transmission enable sensing in otherwise inaccessible locations.

## 2.6 Fiber Bragg gratings

Fiber Bragg gratings (FBG) are highly sensitive, intrinsic OF sensors that can measure temperature, strain and pressure. The sensors work by measuring shift in wavelength that is reflected at the point of measurement. A FBG sensor have gratings inscribed into the core of the fiber, which contain periodic variations of the refractive index. As the transmitted light propagates through the gratings, part of the light spectrum is reflected due to coherent Fresnel reflections from the periodic index variations, and transmitted back to through the fiber (Fig. 23). The centre wavelength of the reflected light is called the Bragg wavelength. The Bragg wavelength change with respect to the refractive index of the gratings ($\eta_{eff}$) and the grating period ($\Lambda$) by the following equation:

$$\lambda_B = 2\eta_{eff}\Lambda \tag{19}$$

Change in $\eta_{eff}$ or $\Lambda$ cause a measurable shift in the Bragg wavelength, which is the working principle for the FBG sensor. The properties of the gratings are changed as the sensor is exposed to either temperature or strain. Strain cause an expansion or contraction of the grating, which alter the grating period. The refractive index of the gratings are affected by both temperature and strain, due to the thermo-optic effect [110], and the strain-optic effect. Grating period is also affected by temperature due to thermal expansion, although this effect is much smaller compared to the change of refractive index [111].

By differentiating equation (1), the total wavelength shift caused by temperature and strain can be expressed as:

$$\Delta\lambda = 2\left(\Lambda\frac{\partial n_{eff}}{\partial T} + n_{eff}\frac{\partial\Lambda}{\partial T}\right)\Delta T + 2\left(\Lambda\frac{\partial n_{eff}}{\partial\varepsilon} + n_{eff}\frac{\partial\Lambda}{\partial\varepsilon}\right)\Delta\varepsilon \tag{20}$$

The first term represent the wavelength shift caused by change in temperature, and can further be expressed as:

$$\Delta\lambda_T = \lambda_B(\alpha+\xi)\Delta T = K_T\Delta T \tag{21}$$

Where $\alpha$ and $\xi$ represent the thermal expansion coefficient and the thermo-optic coefficient, respectively. Combining the terms give $K_T$, which is the temperature sensitivity for the FBG. The sensitivity for a specific FBG sensor can be obtained in a controlled environment, where wavelength shift is recorded as a response to temperature change. Wavelength shift ranging from 10-16pm/°C have been reported in literature [107]. The second term in (20) represent the wavelength shift caused by strain, and can be expressed as:

$$\Delta\lambda_\varepsilon = \lambda_B(1-p_e)\Delta\varepsilon = K_\varepsilon\Delta\varepsilon \tag{22}$$

Where $p_e$ ($\sim 0.22$) is the photoelastic constant and $\Delta\varepsilon$ is the strain change. The value of the strain sensitivity, $K_\varepsilon$, is usually around 1.2pm/$\mu\varepsilon$ applied strain to the FBG [112].

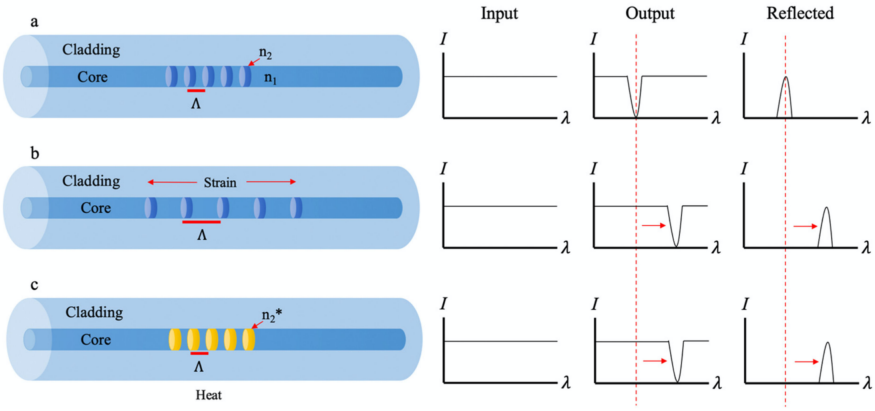


**Figure 23:** a) The components of an optical fiber. The core with the inscribed Bragg gratings is surrounded by the cladding. b) As the gratings are exposed to strain, the grating period changes and a wavelength shift is observed. c) Temperature cause a small increase in grating period and a change in the refractive index of the gratings. Both contribute to the corresponding wavelength shift [17].

As wavelength shift is obtained by changes in both temperature and strain, there is a need to discriminate between the contributions in order to measure a single quantity individually. A common discrimination method is the use of an additional FBG sensor that is isolated from strain perturbations and placed adjacently to the first sensor. The temperature induced wavelength shift that is observed from the reference sensor can then be used to correct the strain measurements of the first sensor.

# 3 Methods

This section will go through the implementation procedure of the fiber sensors in the batteries, as well as the methods that were used for testing and characterization of the batteries. An overview of the process is showed in Fig. 24.

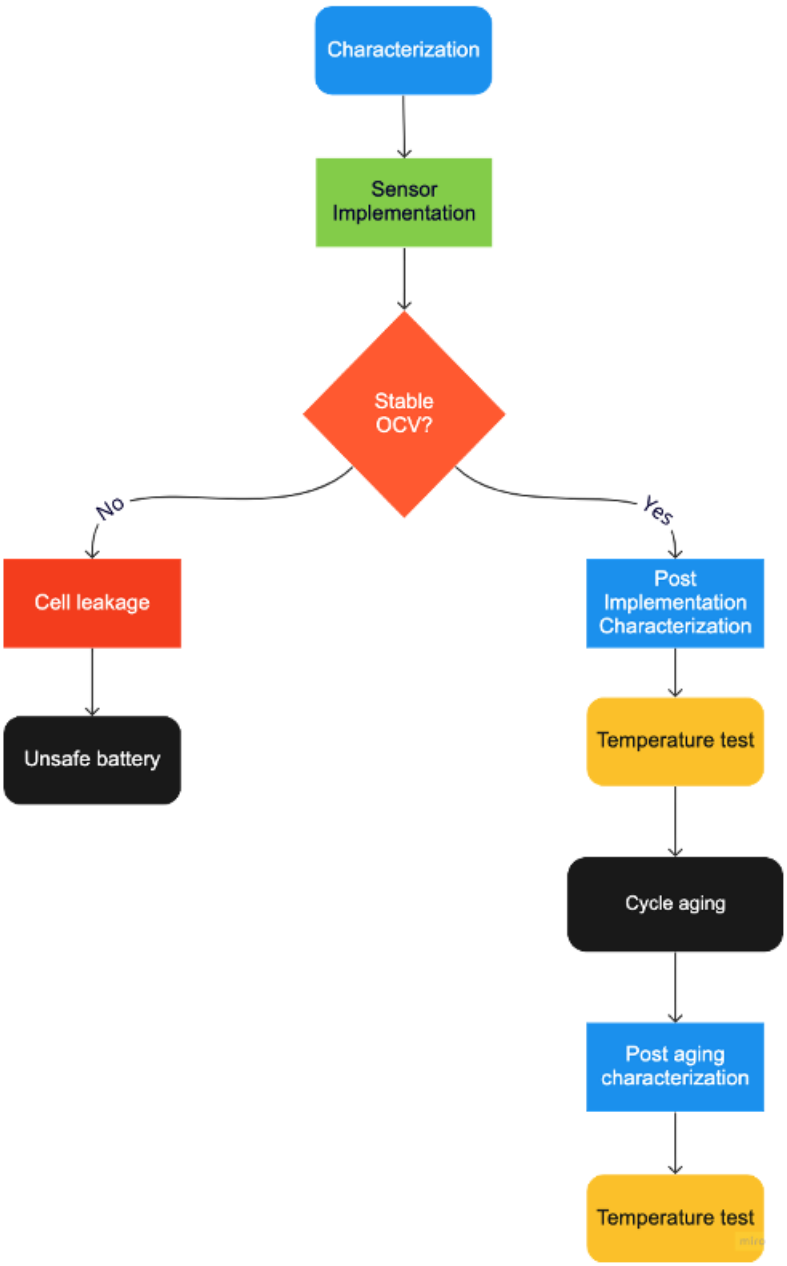


**Figure 24:** Flowchart describing the process of sensor implementation and testing during the project. The batteries were tested after each step that led to a change in the battery characteristics.

## 3.1 Implementation procedure

The following steps were taken to integrate the FBG sensors in the battery:

- Production of new pouch with FBG bracket
- Removal of original pouch
- Repack battery into new pouch assembly and insert capillaries
- Sealing of new pouch

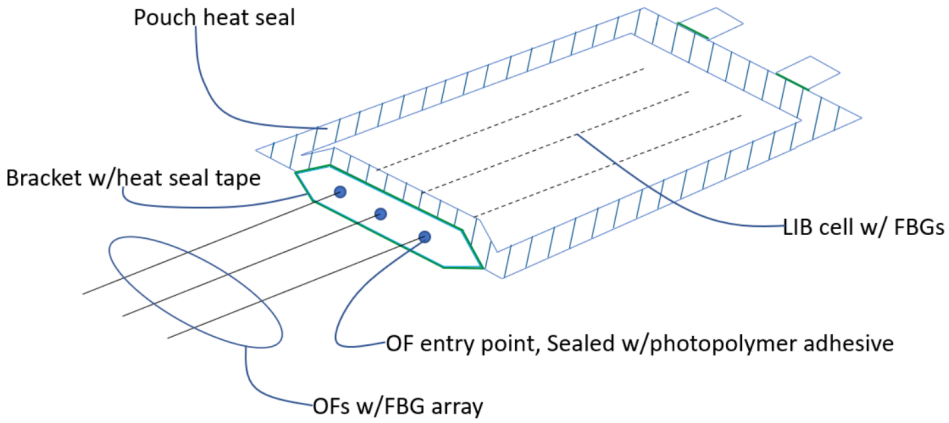


**Figure 25:** Illustration showing the design of the new pouch with embedded FBG sensors. The bracket allow insertion of the FBG sensors, and provides mechanical protection of the fibers during the sealing process [113].

### 3.1.1 Pouch assembly

In this project, commercial LCO pouch cell batteries of the type Melasta SLPBB042126HD (6550mAh, 3.7V) were used. Prior to the removal of pouch laminate from the commercial cell, the batteries were characterised with a test cycle, in order to observe the change in capacity, impedance, and power characteristics resulting from the sensor implementation. A total of three LCO cells were used in this thesis. Two cells that were implemented with fiber-optic sensors, and one reference cell that was opened and repacked without implementing any sensors. In the results section, the cells will be referred to as "Second LCO", "Third LCO" and "Reference LCO". The first LCO had a cell leakage during the second characterization schedule, and was therefore regarded unsafe for further testing.

The first step in the fiber-implementation process include the production of a new pouch assembly for the battery. This is done to support the insertion of glass capillaries through a bracket that is attached to the end of the pouch, opposite to the tab side (Fig. 25). As the sensors are sensitive to both temperature and strain contributions (Eq. 21 and Eq. 22), they are inserted into the glass capillaries to prevent strain contribution to the temperature measurements, and protect the FBG sensors from mechanical damage. The bracket was 3D printed using an Ultimaker 2+ with polypropylene material, which is the same material that is used on the inside of the pouch laminate. This ensure good adhesion between the bracket and the pouch laminate in the sealing process. For insertion of the capillaries into the battery, three holes were drilled through the end of the bracket (see Fig. 27).

In previous testing during the project work, heat seal tape of the type FastelFilm 16071 was used on the bracket side, and a polymer tape of the type EQ-PLIb-HMA4-L200 from MTI was used around the tabs for sealing. However, due to problems with insufficient sealing and subsequent air leakage into the battery, an alternative approach was used in this project. The method included use of a glue gun of the type Ryobi R18GLU-0, with an EVA based hot melt adhesive.

The hot melt adhesive from the glue gun was used to seal all sides of the pouch laminate, including the tab side and the bracket side. Initially, the bracket was glued on to the pouch laminate. In addition, two lines of glue were applied on the inside of the pouch, to create a border that prevents the battery from moving during the subsequent steps (Fig. 27).

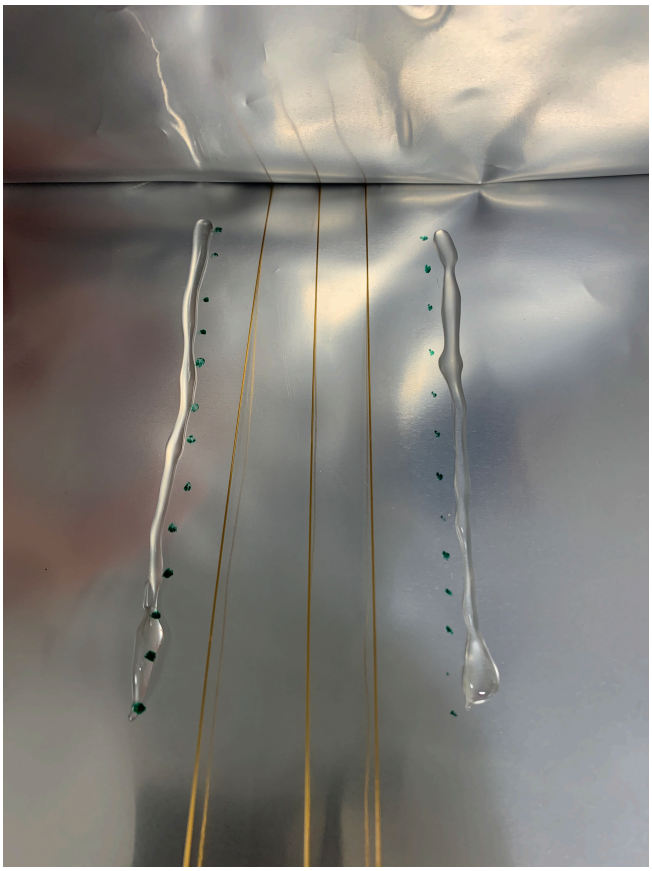

**Figure 26:** Image showing the pouch assembly. The capillaries for the FBG sensors emerge from the bracket at the top of the image.

### 3.1.2 Pouch removal and repack

For the second step the battery and pouch assembly were introduced to a glovebox with an inert argon atmosphere [114] for pouch removal and repack.

The original pouch of the battery was removed without causing damage to the separator or the electrodes of the cell. The separator was then unfolded, and the capillaries were placed in the middle of the battery between the electrode layers. The outer polymer coating of the capillaries that was in contact with the battery was removed with a blowtorch to limit size and invasiveness. After insertion, the cell was slid back into the pouch between the premade borders.

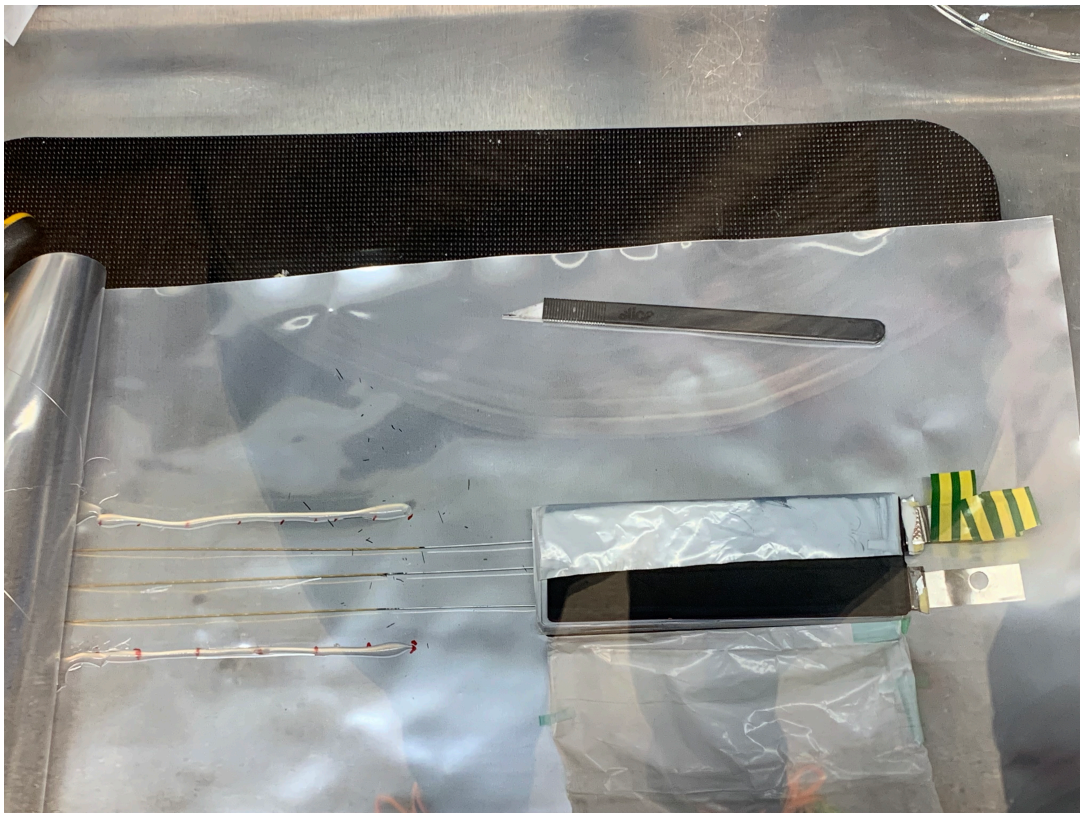

**Figure 27:** Image showing the insertion of the glass capillaries into the middle of the pouch cell battery. After insertion, the battery was slid to the left between the marked boundaries.

After inserting the capillaries, the remaining sides of the battery must be sealed. The long sides of the pouch were sealed using the glue gun, before proceeding to the tab side. For this side, hot melt glue was applied between the tabs and the pouch. To ensure that the hot melt adhesive had sufficiently melted, a hair straightener of the type Remington S1005 was used to apply heat to all sides of the new pouch, where hot melt adhesive from the glue gun had been applied. This ensured that folds in the pouch laminate which could provide a leakage channel for air into the cell was filled with glue and closed (Fig. 28). To prevent leakage from the holes in the bracket, UV glue of the type Norland NOA65 was applied and cured with a UV light source. Lastly, a vacuum chamber of the type AUDIONVAC VMS 53 was used on the tab side to complete the seal. The vacuum chamber evacuates air from the pouch, and applies heat to melt the applied glue at the tab side.

After the implementation procedure, the battery was taken out of the glovebox and placed in a fume hood where the open cell voltage (OCV) was monitored (Fig. 37).

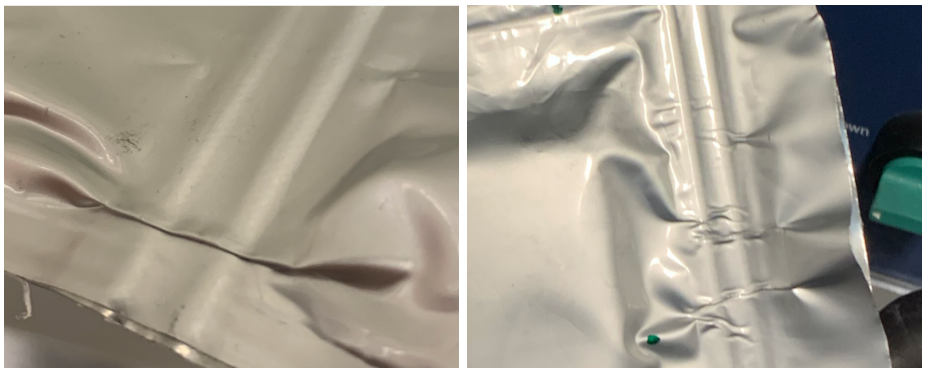

**(a)** Large fold **(b)** Multiple small folds

**Figure 28:** Image showing folds that are created during the repack of the pouch laminate.

## 3.2 Battery testing and characterization

To evaluate the impact of the sensor implementation on the batteries, different battery testing schedules were used in the project. The characterization schedules were completed on each battery before and after implementation, and after cycle aging. The characterization included charge/discharge cycles at different C-rates and a hybrid pulse power characterization (HPPC) to evaluate the internal resistances of the battery. The aim of the characterization schedule is to reveal changes in battery characteristics related to capacity and internal resistance. The following schedule was used as initial characterization of the batteries:

- Discharge and charge at 1C
- Discharge and charge at C/20
- Discharge and charge at C/4
- HPPC characterization at different SOC
- Discharge at C/4, C/10 and C/20

Different current rates were used to compare discharge and charge capacity before and after the sensor implementation. A hybrid power pulse characterization (HPPC) was used to measure the internal resistances in the battery at different SOC. HPPC is based on the battery voltage response during short DC current pulses. Fig. 29 shows the principle of a HPPC test.

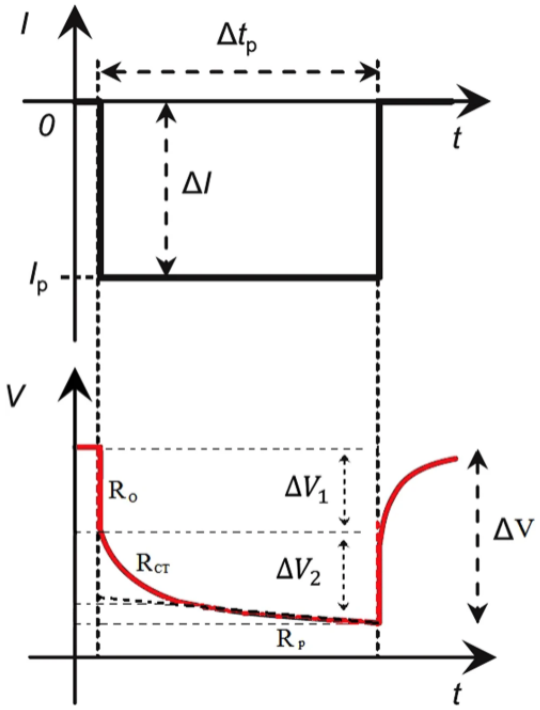


**Figure 29:** HPPC characterization. The upper figure shows the applied DC current pulse, while the lower figure shows the voltage response. The resistances $R_o$ and $R_p$ are measured from the corresponding voltage drop $\Delta V_1$ and $\Delta V_2$ after a chosen time step. [115]

In a HPPC test, the voltage change from an applied current load is measured in order to obtain the internal resistance of the battery. The measured internal resistance is depends on the time step that is used to observe the voltage difference. Initially, the voltage drop from the applied current is caused by ohmic overpotentials in the battery ($R_o$ in Fig. 29). The voltage drop from the remaining time of the current pulse is a combination of charge transfer resistance, and polarisation resistance in the cell [115]. These resistances are annotated as $R_{ct}$ and $R_p$ in Fig. 29. The ohmic resistance is a result of electronic resistances, and electrolyte ionic resistance in the cell. The charge transfer resistance is due to charge transfer reaction at the electrolyte interphase, while the polarisation resistance is a result of ionic diffusion in the solid phase [115]. Fig. 30 shows an example of a HPPC pulse from a characterization test.

For the HPPC tests in this thesis, the voltage was measured after 50ms and 5s. The first measurement is dominated by the ohmic resistance ($R_o$). The resistance measured from 50ms to 5s includes the voltage drop from both charge transfer and polarisation resistance, and can therefore be considered as a combination of these contributions:

$$R_o = \frac{V_0 - V_{50ms}}{I} \tag{23}$$

$$R_2 = \frac{V_{50ms} - V_{5000ms}}{I} \tag{24}$$

HPPC testing were done before and after sensor implementation, and after cycle aging.

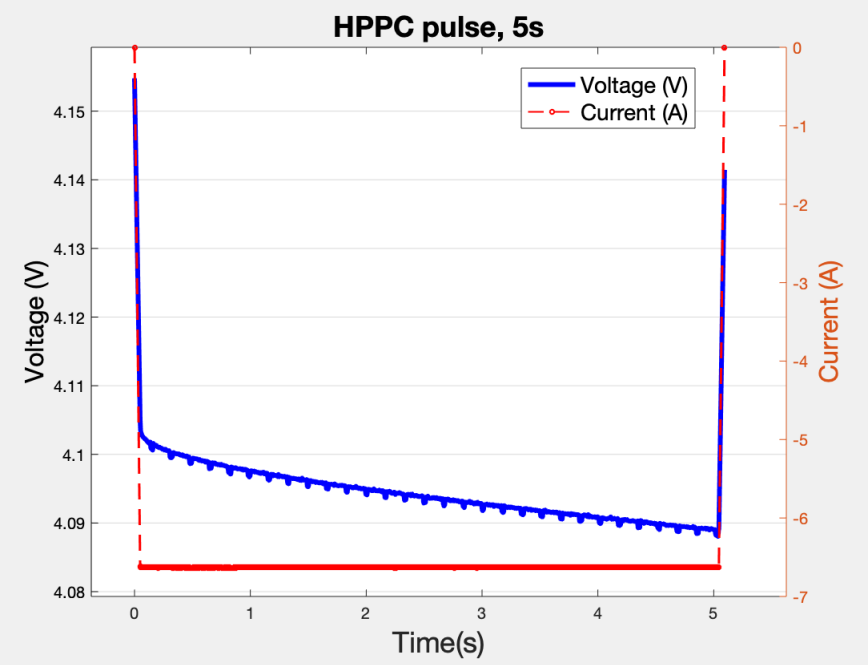


**Figure 30:** Example of a HPPC pulse that were used in the characterizations. This test was done at 100% SOC, and the applied discharge current was 1C (6.63A). The initial voltage drop from 4.155V to 4.103V is much larger than the remaining voltage drop from 4.104V to 4.088V.

## 3.3 Cycle aging

If the batteries showed a stable behaviour after the characterization, they were put through a temperature test and a cycle aging procedure. The aim of the aging cycle was to monitor the capacity fade and internal resistance over the cycle period. In addition, the subsequent temperature test would reveal changes in the temperature development of the battery at a reduced SOH. The following schedule was used for the cycle aging of the batteries:

- CC charge at 1C to high cutoff voltage at 4.2V
- CV charge at 4.2V to low cutoff current at 0.08·1C
- 2 minute rest
- Discharge at 1C to low cutoff voltage at 3V
- 2 minute rest
- Repeat above steps until 200 cycles are reached

## 3.4 FBG calibration and measurement

The setup that was used for the temperature measurements with the FBG sensors are showed in Fig. 32. The light spectrum from the IR source is sent through the optical couplers and the FBG sensors of the battery. The reflected wavelengths from the sensors are detected by the spectrometer and sent to the computer for processing. The specifications of the FBG equipment are given in Fig. 31.

| Equipment | Suplier | Model | Spec |
|---|---|---|---|
| FBG Array | Fisense | | Number of FBG: 3<br>OF diameter: 0,125mm<br>Reflectivity: >50% |
| IR Source | Thorlabs | SM benchtop SLD source | wavelength: 1550 nm<br>bandwitdth: 50nm |
| Spectrometer | Ibsen photonics | I-mon 512 USB | Wavelength range: 1510-1595 nm<br>Wavelength accuracy: 5 pm<br>Measurement frequency: 3000Hz |
| Couplers | Thorlabs | 50:50 Wideband Coupler 1x2 and 2x2 | Center wavelength: 1550nm<br>Signal Output: 45,0%-55,0%<br>Tap Output: 45,0%-55,0% |

**Figure 31:** Equipment used for the fiber optic sensing. [113]

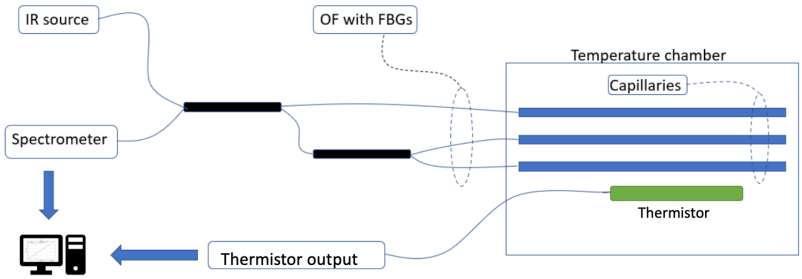


**Figure 32:** The experimental setup for the temperature measurements. [113]

An example of the reflected light spectrum that was detected by the spectrometer is shown in Fig. 33. The amplitude of the reflected signal is lower for two of the FBG arrays, due to splitting of the signal in optical couplers.

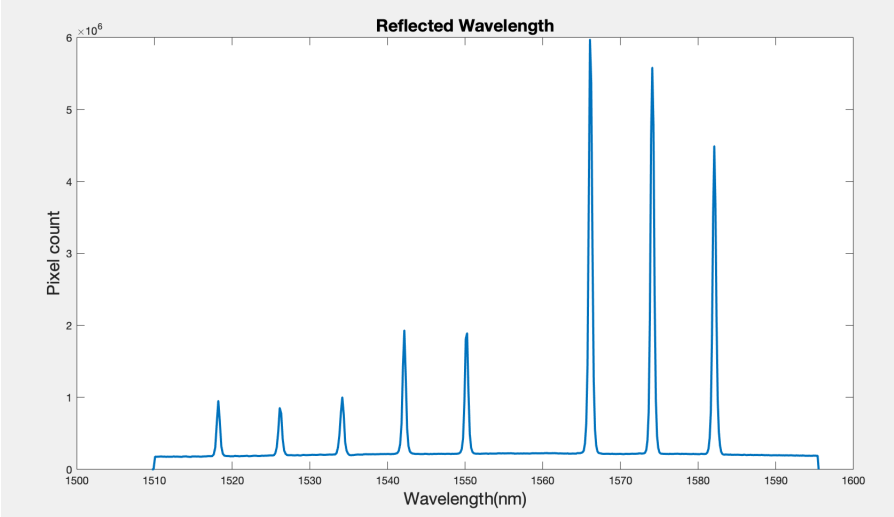


**Figure 33:** Example of the reflected wavelengths that were obtained by the spectrometer.

As described in equation 21, the wavelength shift is dependent on the temperature sensitivity of the FBG sensor. The sensors that were used in this thesis were calibrated in a earlier study [113]. This was done by placing the FBG sensors in a temperature chamber, and observing the wavelength shifts at different controlled temperatures. The obtained results can be seen in Fig. 34 and were comparable to reported values [111].

| FBG central wavelength [nm] | Temperature sensitivity [pm/°C] |
|---|---|
| FBG array 1 | |
| 1518 | 9.43 |
| 1526 | 9.52 |
| 1534 | 9.52 |
| FBG array 2 | |
| 1542 | 9.62 |
| 1550 | 9.43 |
| 1558 | 9.71 |
| FBG array 3 | |
| 1566 | 9.90 |
| 1574 | 9.90 |
| 1582 | 10.0 |

**Figure 34:** Calibration results for the temperature sensitivity [113].

To enable detection of the central wavelength with high accuracy, some processing of the reflected wavelength is required. The temperature induced wavelength shifts are smaller than the pixel resolution that is obtained from the computer software. Therefore, the reflected wavelength was fitted with a Gaussian to enable a more precise location for the central wavelength (Fig. 35).

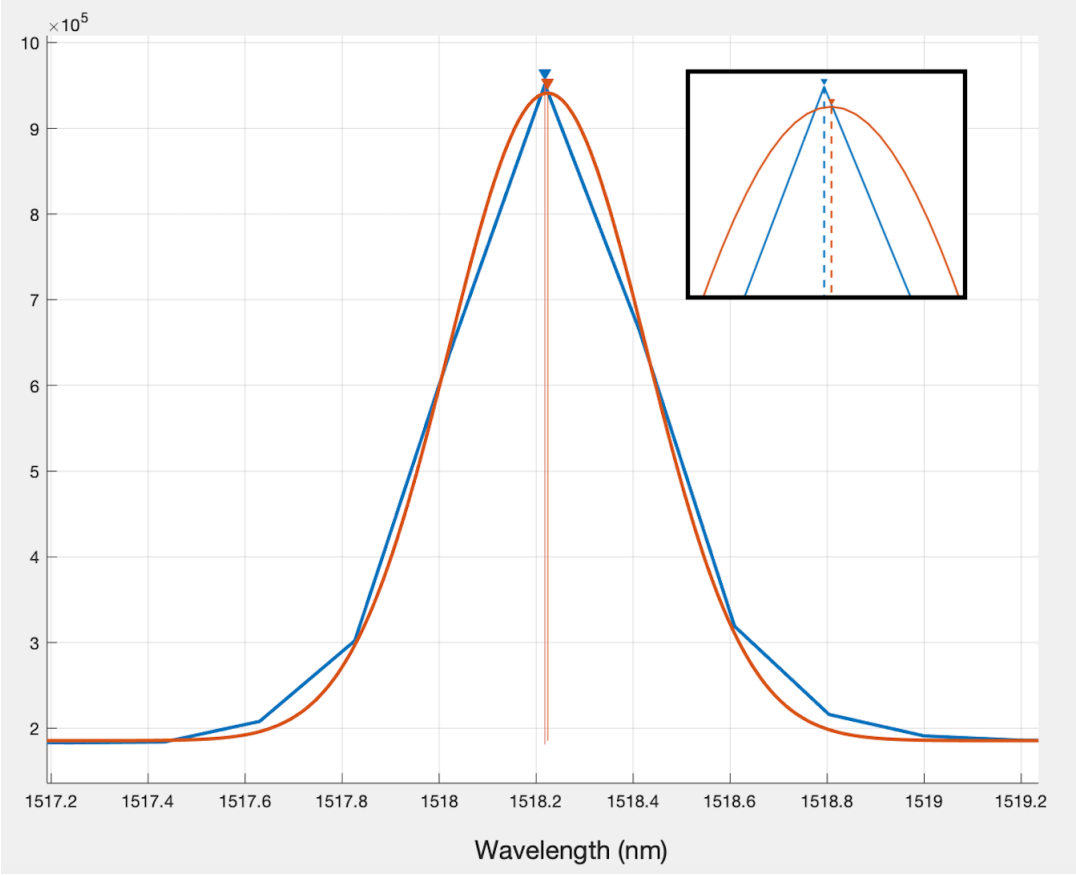


**Figure 35:** Gaussian fit to the central wavelength of one of the FBG sensors.

A Gaussian function was fitted to the Bragg peak at each recorded time step during the temperature tests. A Matlab script with a least squares method was used for the graph fitting.

## 3.5 Temperature measurements

The internal temperature measurements were conducted after implementation of the optical fiber sensors, and after cycle aging. The following testing schedule was selected to observe the temperature development inside the battery at different charge and discharge rates:

- Charge and discharge at 1.5C
- Charge and discharge at 1C
- Charge and discharge at C/2

*15 minute rest between every charge and discharge.*

## 3.6 Battery type

The cell that were used in this thesis is a LCO battery from Shenzhen Melasta Battery Co. ltd. The characteristics of the cell is given by the table below.

| Melasta SLPBB042126 | | |
|---|---|---|
| **Cathode material** | | $LiCoO_2$ |
| **Nominal capacity** | | 6550mAh |
| **Nominal voltage** | Maximum voltage<br>Cut off voltage | 3.7V<br>$4.2 \pm 0.03$V<br>3.0V |
| **Impedance** | | 1.3mOhm $\pm$ 0.3 |
| **Max continous discharge rate** | | 65.5A (10C) |
| **Max continous charge rate** | | 10A |
| **Operating temperature** | Charge<br>Discharge | 0°C - 60°C<br>-20°C - 60°C |

**Figure 36:** Data sheet for the cell used in the thesis [116].

# 4 Results and discussion

This section will present the results that were obtained from the experiments, and discuss these. The results from three cells are presented in this chapter: two with fiber-optic sensors implemented, and one reference that was only opened and re-packed without implementing any sensors. The cells that were implemented with fiber-optic sensors will be referred to as "Second LCO" and "Third LCO" in the following section. The reference cell will be referred to as "Reference LCO".

## 4.1 Implementation procedure and invasiveness

This section will present the changes that were observed in the cells after cell opening and sensor implementation. This will be done by comparing the capacity and internal resistance of the cells before and after sensor implementation. The implementation procedure that was used in the thesis

were a result of several attempts from previous experiments to create a battery with integrated sensors [117]. In the previous work, the most challenging part of the sensor implementation was to hinder air and moisture ingression into the cell, which would dry out the electrolyte and cause HF generation through hydrolysis of $LiPF_6$ [118]. This would lead to cathode material degradation and loss of lithium inventory in the cell, thus decreasing cell performance. The method that was used succeeded in achieving an airtight seal, which was prioritised in order to continue cell testing and temperature measurements. In the following, the impact of sensor implementation on cell performance will be discussed with regards to capacity and internal resistance.

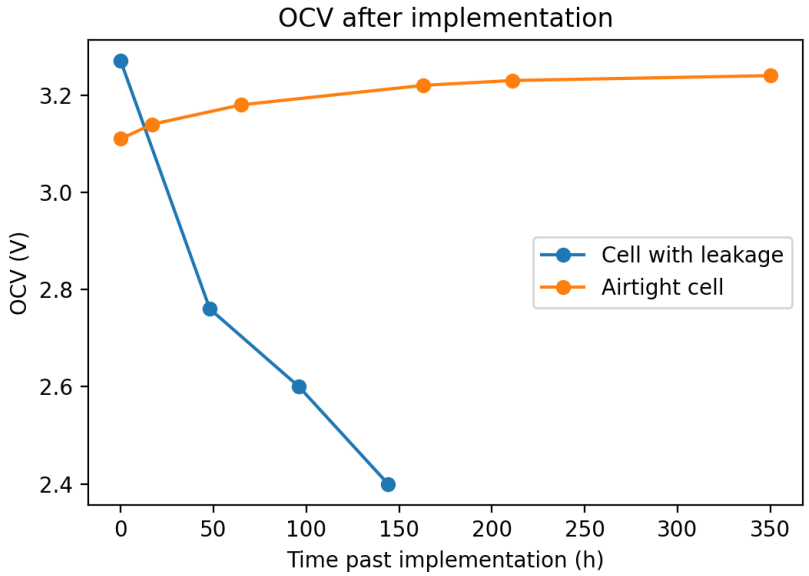


**Figure 37:** Plot showing the measured OCV of the pouch cell after implementation and exposure to atmospheric conditions. The successfull implementation shows an increasing OCV, as the battery is reaching steady state after complete discharge.

### 4.1.1 Cell capacity

The characterization of the batteries before and after implementation gave a clear picture of the change in capacity due to sensor implementation. The characterization included different current rates, which would yield different discharge and charge capacities (see section 3.2). Fig. **??** shows one of the characterization tests. The discharge capacity is evaluated from the basis of a C/4 discharge. The C/4 discharge was chosen as it followed directly after a C/20 charge, which allows charging with lower overpotentials compared to higher C-rates. This allows for more lithium ions to be transferred to the battery anode.

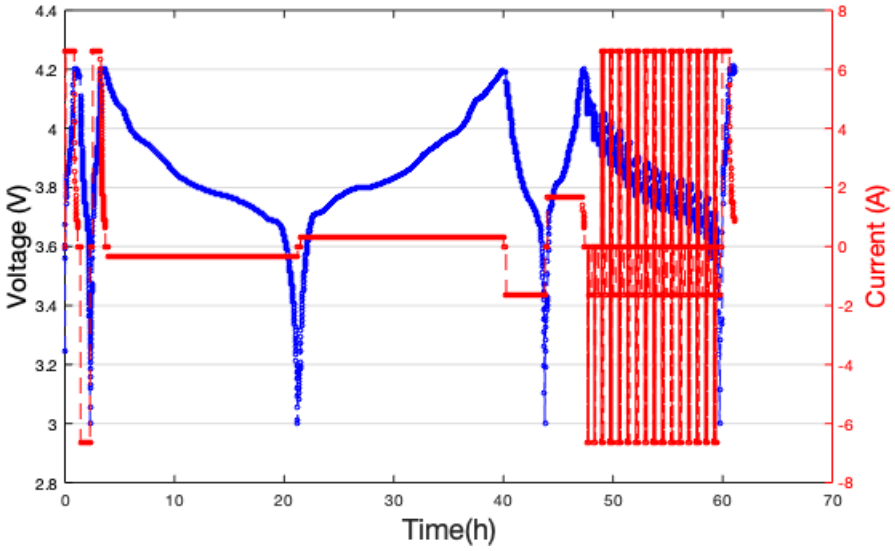


**Figure 38:** Plot showing the voltage and current during the full characterization test. The battery is charged and discharged at 1C, C/20, C/4 before a HPPC test at decreasing SOC is conducted.

Fig. 39 shows the discharge capacity of the batteries prior to sensor implementation.The capacities that were reached was in the range 6.67 to 6.89Ah, which is in excess of the capacity given by the manufacturer for 0.2C and 23°C.

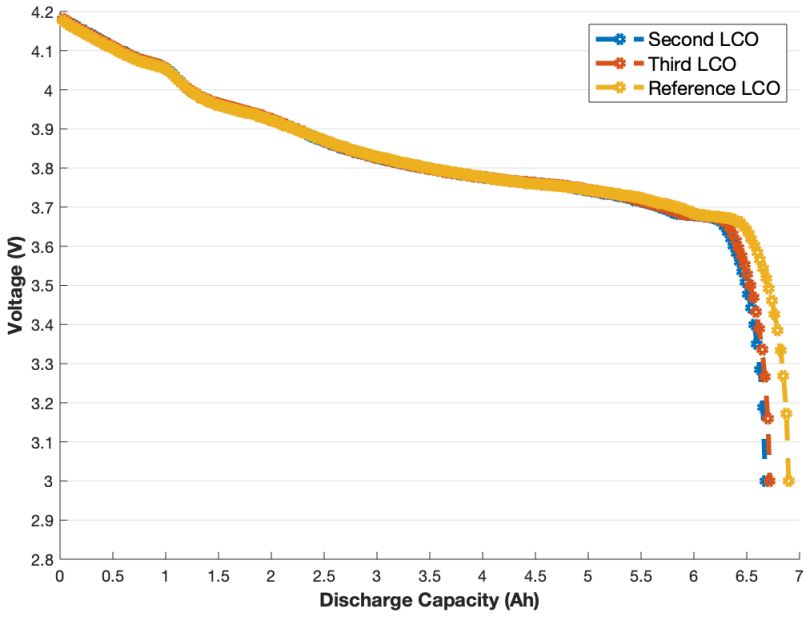


**Figure 39:** Discharge curves showing the capacity of the batteries for a C/4 discharge before sensor implementation.

Fig. 40 shows the discharge capacity measured after implementation. It is clear that the capacity have decreased for all batteries, however the decrease is far greater in the batteries with implemented FBG sensors. The second LCO showed a capacity decrease of 0.83Ah, or 12.4%. The third LCO showed a considerably larger decrease of 1.64Ah, or 24.4%. In comparison, the reference cell which had no internal sensors implemented, showed a much lower relative decrease in capacity. The capacity decrease for this cell was 0.27Ah, or 3.9%. However, due to individual cell differences,

the initial capacity of the reference cell was a bit higher than the other cells.

The observed decrease in capacity can be the result of several factors. During the implementation procedure, the battery is inevitably subject to some mechanical abuse in order to fit the sensors between the electrodes. This may cause permanent damage to parts of the electrode layers, and change the initial characteristics of the battery. The reference cell did not undergo as much mechanical abuse, and in addition, was left opened for a shorter amount of time compared to the other batteries. In factory pouch cell production, the battery is vacuum sealed, which ensure good contact between the electrode layers. However, the vacuum sealer that was tried out in previous experiments failed to sufficiently close the pouch cell, and was therefore not used in this thesis [117]. Therefore, the electrode layers of the batteries may be held more loosely together, which decrease the conductivity of the cell.

The poor conductivity between the electrodes was evident as the batteries were tested after implementation. It was observed that the voltage of the battery would increase if a light pressure was applied to the battery surface. This was interpreted as a decrease in overpotentials caused by the reduced distance and improved contact between the electrodes. Therefore, to compensate for the lack of vacuum, all batteries were pressurised with two plexiglas plates that were located at the top and bottom of the cell. After applying pressure, the reduced internal resistance would allow greater C-rates through the battery within the safe operating voltage.

In addition to poor contact between the electrode layers, a capacity loss may be caused by loss of electrolyte during the implementation procedure. During sensor insertion in the glovebox, a considerable amount of time is spent with an open cell, facilitating loss of electrolyte from the battery. Lower electrolyte volume have been shown to negatively affect the capacity and internal resistance of a battery [119]. Therefore the loss of electrolyte may have contributed to the observed capacity fade.

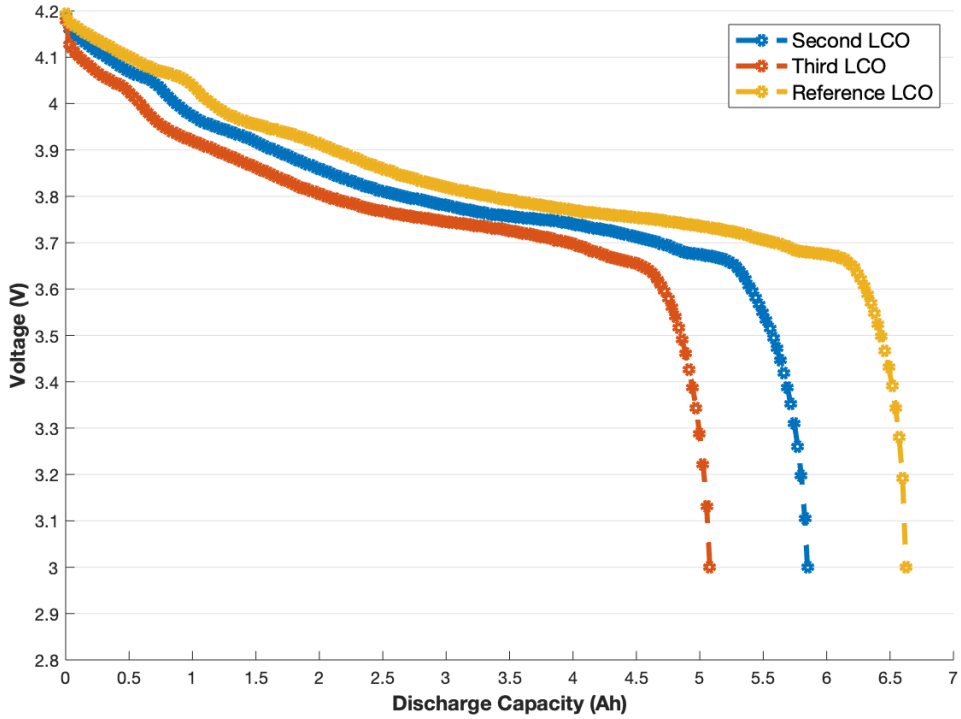


**Figure 40:** Discharge curves showing the capacity of the batteries for a C/4 discharge after sensor implementation.

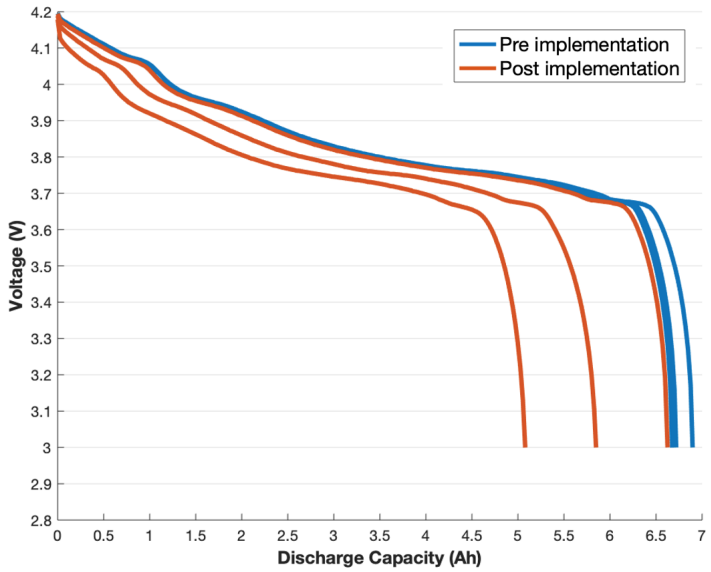


**Figure 41:** Discharge capacity of the batteries prior to and after sensor implementation. The red curves represent the discharge curves after sensor implementation, the blue curves represent the discharge curves before sensor implementation.

### 4.1.2 Internal resistance

The internal resistances of the one battery were measured before and after sensor implementation, and after cycle aging. For the third LCO and the reference cell, a HPPC test was done. Fig. 42 shows the difference in the total internal resistance for cell 2.

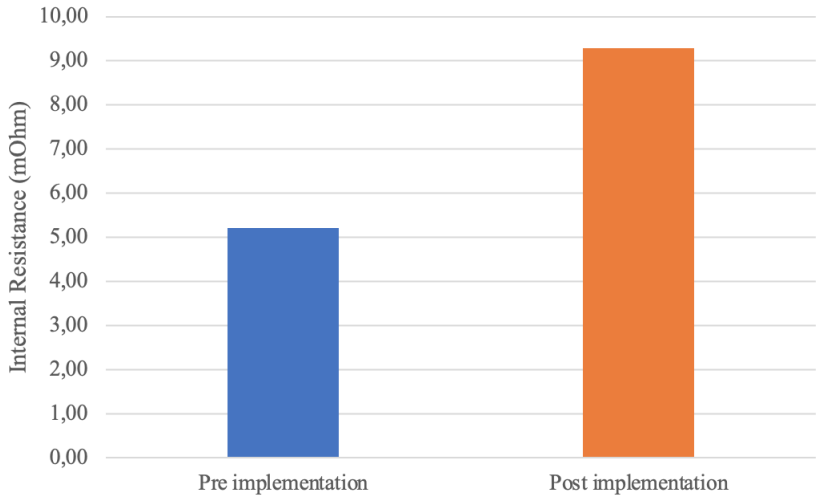


**Figure 42:** Increase in internal resistance after sensor implementation.

The internal resistance for the second LCO increased by a factor of 1.8 after the implementation. The resistance was determined by measuring the voltage drop from a 10 second discharge at 1C at 100% SOC.

Fig. 43 shows the result from the HPPC test before and after sensor implementation of the third LCO. The ohmic resistance, $R_o$, increased significantly from 2.9 to 18.2 mOhm. $R_2$ also increased, from 0.7 to 4.2 mOhm. The large increase in $R_o$ points to an increase in the bulk electrolyte resistance and resistance of the electric components of the cell. The bulk electrolyte resistance could

be a result of loss of electrolyte during the implementation procedure. However, the mechanical abuse that the battery may be subject to during implementation could have affected the ohmic resistance as well.

Fig. 44 shows the result from the HPPC test before and after sensor implementation of the reference LCO. The results show that there is a slight increase in $R_2$, however the test showed a decrease in ohmic resistance which caused the overall resistance to decrease. The total resistance for the reference LCO is 4 times smaller compared to the third LCO, which points to an elevated resistance due to the implementation process of the FBG sensors.

Fig. 45 shows the measured $R_2$ at different SOC for the batteries after sensor implementation. The charge transfer and polarization resistance increased as the SOC decreased, which, as will be discussed later, leads to a greater heat generation towards the end of discharge.

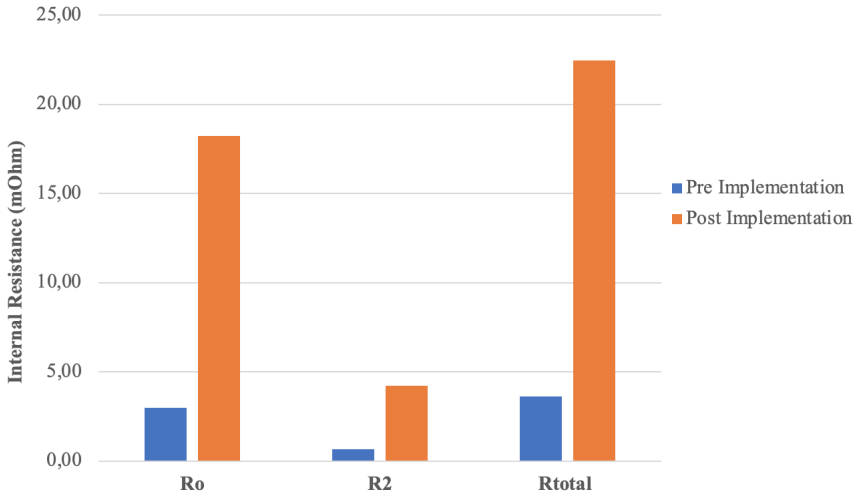


**Figure 43:** Resistance for the third LCO before and after sensor implementation.

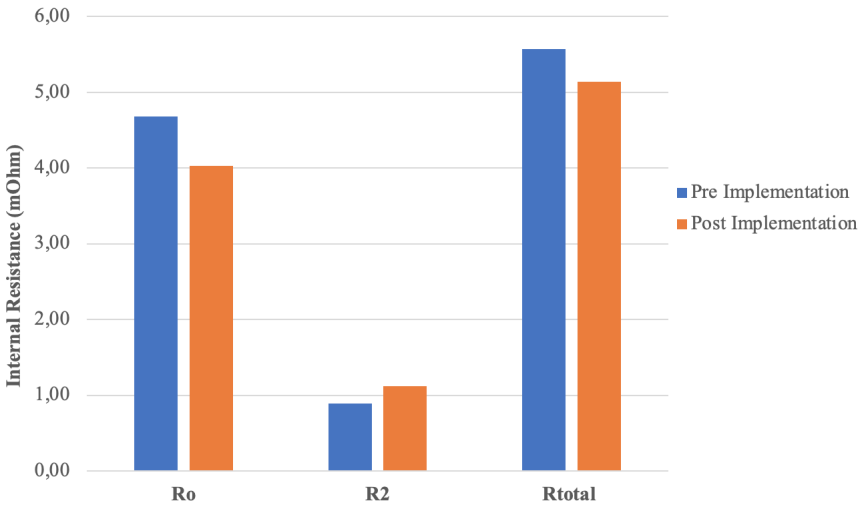


**Figure 44:** Resistance for the reference cell before and after pouch repack.

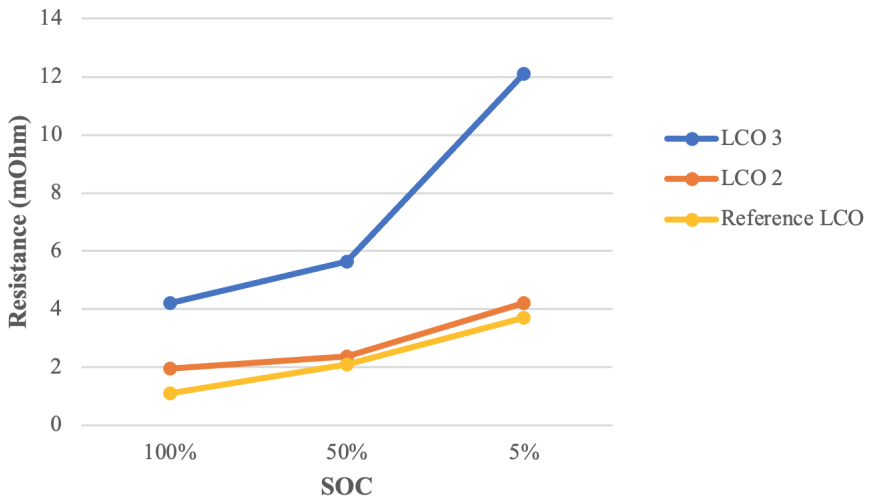


**Figure 45:** Plot of polarization and charge transfer resistance at different SOC for the batteries. Resistance increase as SOC decrease.

## 4.2 Aging effects

As two of the batteries showed promising characteristics in terms of seal integrity, they were cycled at 1C for 200 cycles. The capacity fade of the batteries can be seen in Fig. 46. The second LCO experienced a large decrease in capacity for the first 20 cycles, before reaching a stable decrease of approximately 3mAh/cycle. The third LCO showed a smaller initial decrease in capacity, however the capacity fade were more substantial throughout the aging cycle. The third LCO reached a steady decrease of 8.7mAh/cycle after 100 cycles. Interestingly, both batteries showed this linear decrease in capacity after a certain amount of cycles. The reference LCO with no internal fiber sensors showed a comparable capacity fade to the second LCO, although initially the capacity fade was at a lower rate.

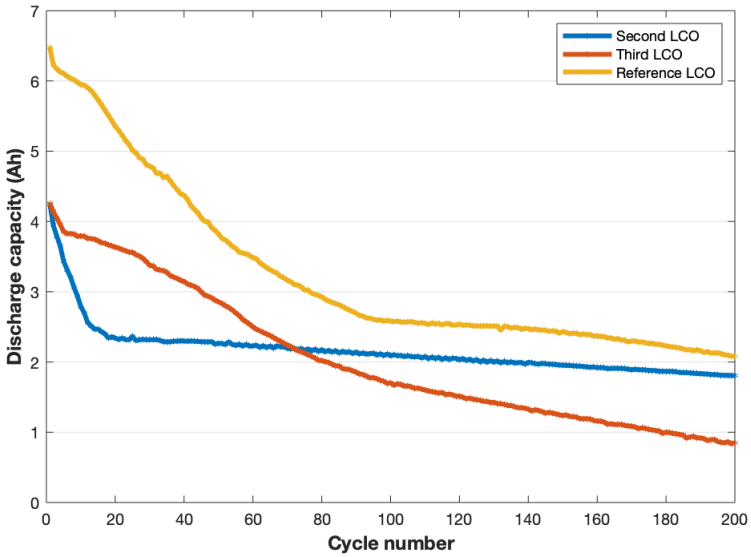


**Figure 46:** Capacity fade for the three batteries with implemented sensors during cycle aging.

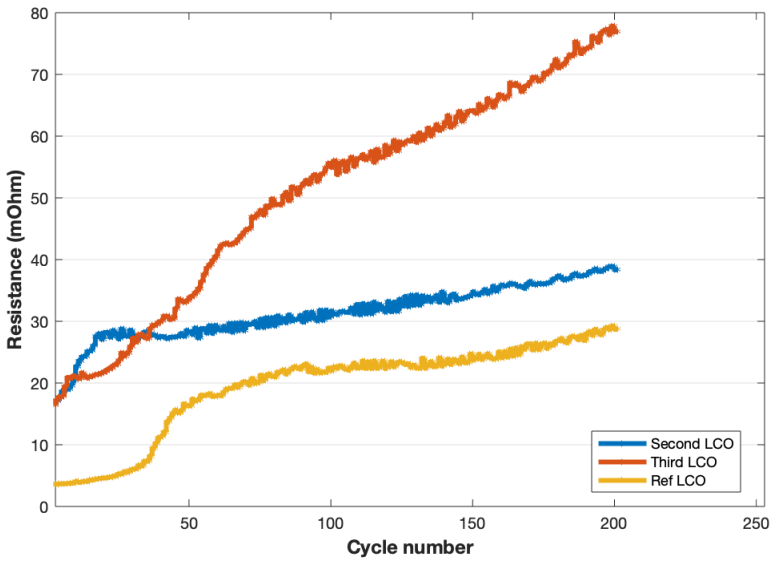


**Figure 47:** Resistance increase for the three batteries during cycle aging.

The resistance of the batteries was also monitored during cycle aging. Fig. 47 shows the increase in resistance for the batteries during cycle aging. The resistance was determined from the battery tester at the start of each aging cycle, and not from a HPPC test. As the internal resistance increased throughout the cycle aging, the discharge capacity decreased. An increased internal resistance leads to faster voltage drop during discharge. Therefore less charge is recovered and capacity is decreasing. Fig. 49 shows this explicitly, as the capacity fade and resistance increase during cycle aging is plotted in the same figure for the third LCO.

After cycle aging, another characterization and HPPC test was conducted to evaluate the internal resistances of the cells. The relative increase in the internal resistances after cycle aging is shown in Fig. 48. Although the resistance for the third LCO was over twice as high compared to the second LCO, the relative increase after enduring cycle aging was similar. The processes causing the capacity loss can therefore be assumed to be similar, and the discrepancy between the cells be attributed to the sensor implementation. The highest increase was in the ohmic resistance $R_o$, which increased around 7 times for all cells. This points to an elevated bulk electrolyte resistance, which could be caused by evaporation of the electrolyte through minor cell leakage.

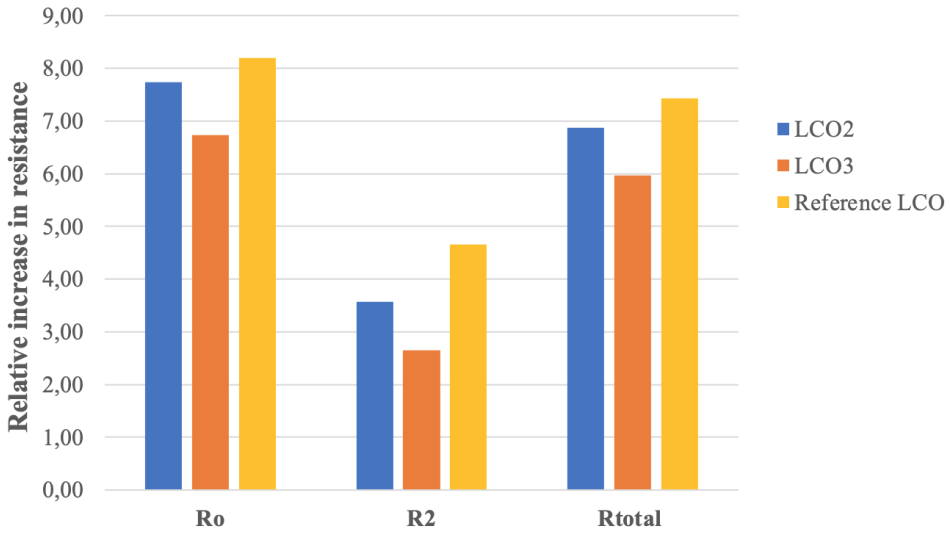


**Figure 48:** Relative increase in the internal resistance of the batteries after cycle aging.

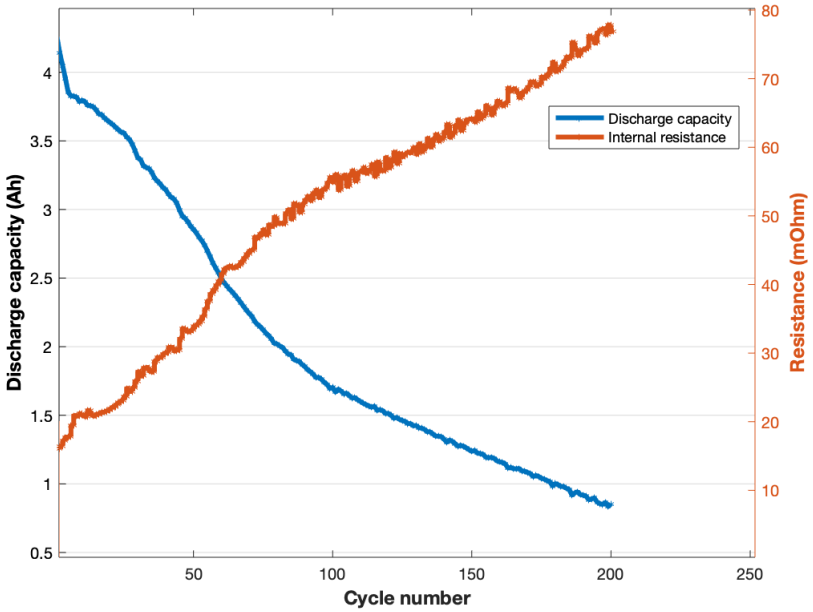


**Figure 49:** Resistance and capacity during cycle aging.

During cycle aging, the high cutoff voltage during charging was reached rapidly, due to the large overpotential of the batteries. This caused the charging part of the schedule to be mostly CV charge at 4.2V (see section 3.3). During charging at this high voltage, lithium is irreversibly lost through side reactions like SEI layer growth, which in turn leads to capacity fade [120]. This likely contributed to the fast increase in internal resistance and capacity fade of the batteries.

## 4.3 Temperature tests

Three temperature tests were conducted to measure the internal temperature of the batteries. The temperature tests were conducted at different current rates, in order to observe the temperature development at different loads. Two tests were done after sensor implementation, and one test was done after cycle aging. First the pre-aging results will be presented and discussed, followed by the post-aging results.

**Temperature test - Second LCO**

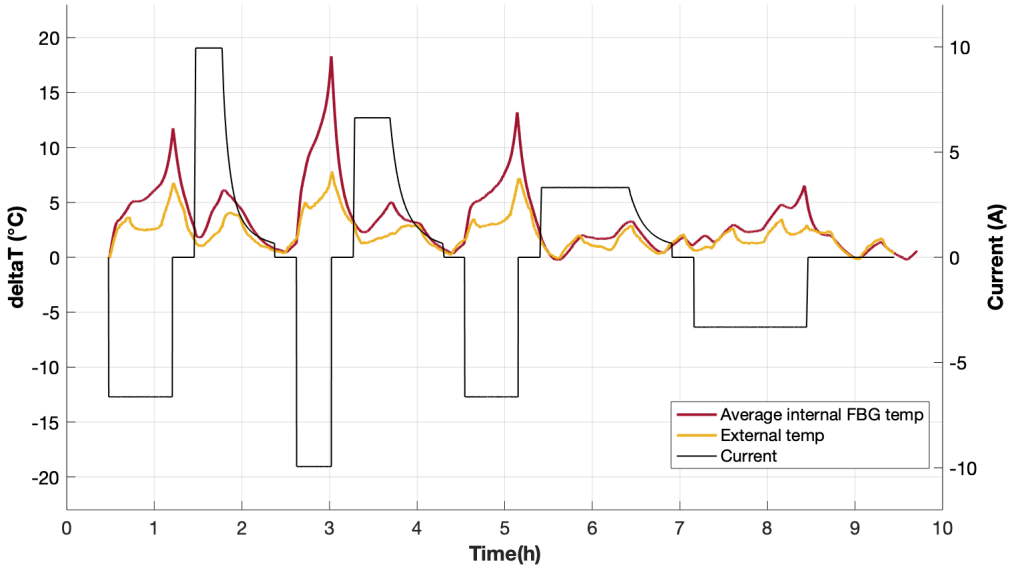


**Figure 50:** Overview of the first temperature test with internal FBG temperature sensors for the second LCO. The temperature peaks are a response to discharge at 1C, 1.5C, 1C and C/4. The temperatures are given as a change from the initial temperature when the current was first applied.

Two tests were done after implementing the temperature sensors in the batteries. The first test done on the second LCO can be seen in Fig. 50. The plotted internal temperature shows the average for the three internal temperature sensors. This test was done with a light pressure added to the tab side of the pouch cell, in order to reduce internal resistance of the cell. This may have affected the temperature distribution inside the battery, which will be discussed in this section.

Fig. 51 shows the first 1C discharge for the temperature test, for the second LCO. The ambient/room temperature is varying, because of the HVAC system regulation of the room where the temperature test was done. An external FBG sensor was placed adjacently to a thermistor on the surface of the pouch cell to measure the external temperature. From Fig. 51 it can be observed that the external temperature sensors were more influenced by the change in ambient temperature compared to the internal temperature sensors. For instance, the decrease in ambient temperature after around 0.7h caused the surface temperature of the battery pack to decrease, whereas the internal temperature were at a steady state. During the 1C discharge, the internal temperature in the cell increased by 11-12°C, reaching the highest temperature at the end of discharge. The highest measured temperature increase on the battery surface was 6.7°C. The end of discharge was also the time with the highest deviation of the external sensors compared to the internal ones, of around 5°C.

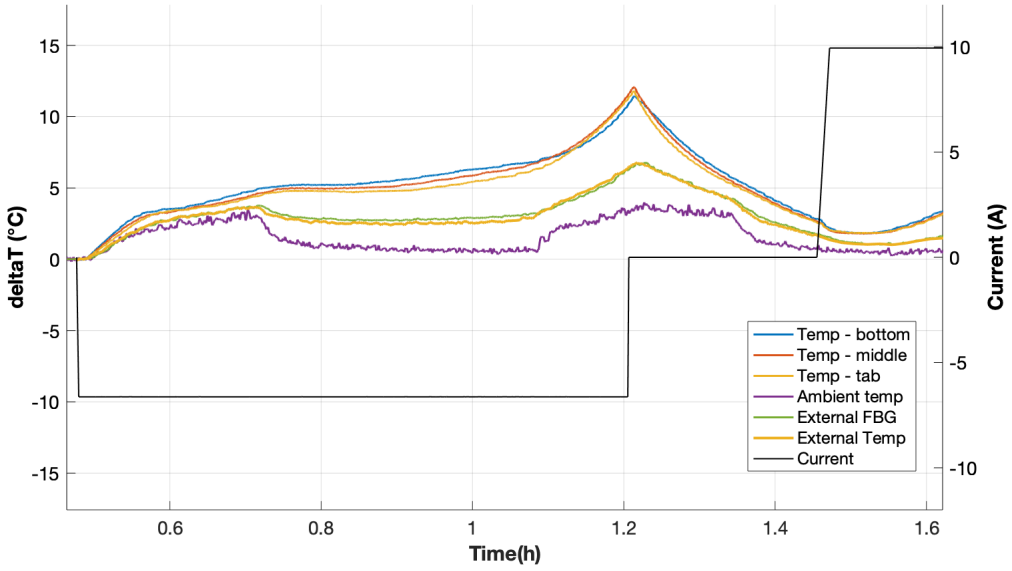


**Figure 51:** Plot of the temperature development in the battery during a 1C discharge, for the second LCO.

Fig. 52 shows the temperature change during the 1.5C discharge, for the second LCO. The temperature increased internally by 13.5 to 17.9°C. In contrast to the first 1C discharge, the variations from the different temperature sensors were large, at most 4.3°C at end of discharge. In addition, the measured external FBG sensor deviated more from the thermistor temperature. The highest temperature were measured on the bottom of the pouch cell, opposite to the tab side.

The temperature development during C/2 discharge can be seen in Fig. 53. The temperature increase was much lower compared to higher discharge rates, and more influenced by the ambient temperature. The same temperature variations between the internal temperature sensors were observed at the end of discharge. Similar to the 1.5C discharge, the temperature was highest at the bottom of the cell, and lowest at the tab side. This could be a result of the applied pressure on the tab side of the cell, which may increase the thermal conductivity and dissipation from the this side of the cell. In this way heat is transported away from the tab side more efficiently compared to the bottom of the cell.

It is apparent that for all discharge rates, the highest temperature increase is at end of discharge, due to increase in polarization and charge transfer resistance at lower SOC (Fig. 45). In Fig. 54 the voltage of the battery and temperature change are shown during a 1C discharge. The temperature increase is at its highest as the battery voltage go below around 3.5V during discharge.

The discharge temperatures for the test are shown in Fig. 55 a). The largest temperature increase was at the beginning and end of discharge for all C-rates. The C/2 discharge temperature was more sensitive to the change in ambient temperature, due to a much lower internal heat generation. The decrease in temperature that can be seen at three different locations during the discharge, points towards the heat diffusion at the surface being greater than the internal heat generation.

The difference in temperature increase between the internal and external temperature sensors are shown in Fig. 55 b). The difference is a result of the finite thermal conductivity of the battery components, which limits the heat diffusion from the inside of the cell to the surface (see section 2.2.2). As the C-rate increase, more heat is generated through ohmic heating, which increase the temperature difference between the inside and surface of the cell. The highest difference was observed at the end of discharge, reaching at most 10°C during the 1.5C discharge. The differences between the shape of the curves for Fig. 55 b) shows how the ambient temperature is affecting the external temperature sensors to a higher degree than the internal temperature sensors.

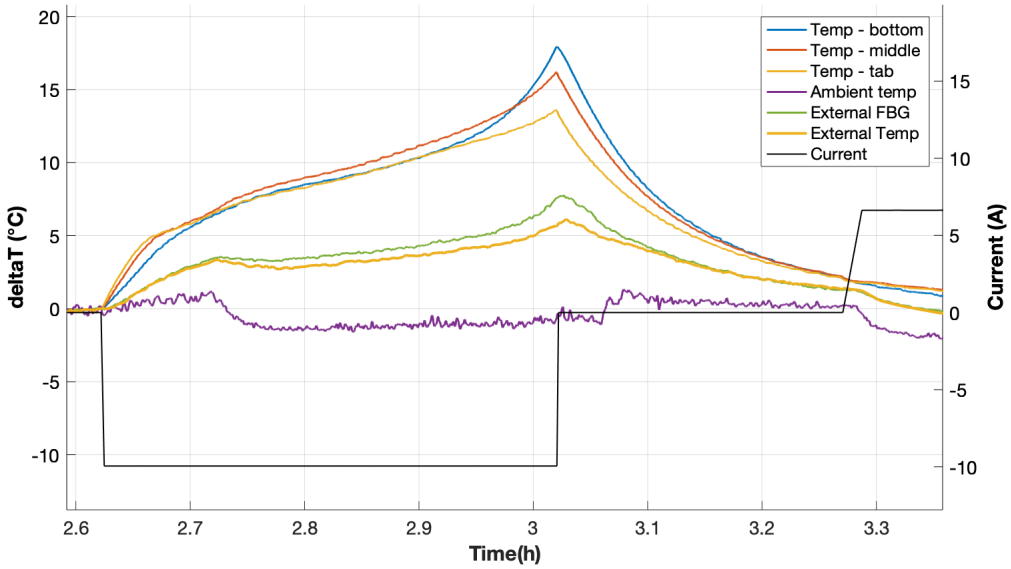


**Figure 52:** Plot of the temperature development in the battery during a 1.5C discharge.

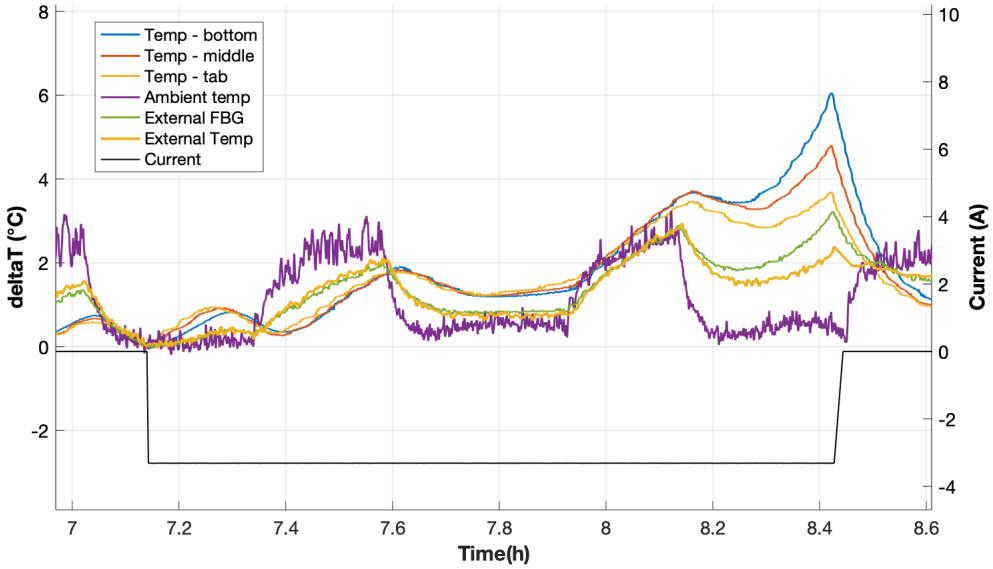


**Figure 53:** Plot of the temperature development in the battery during a C/2 discharge.

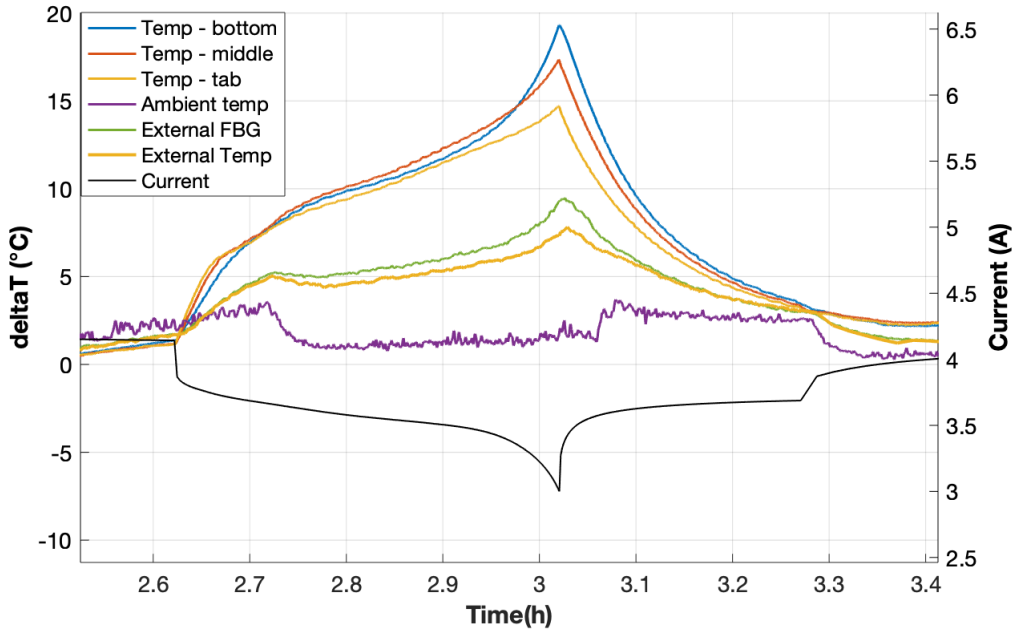


**Figure 54:** Temperature development at 1.5C discharge and battery voltage.

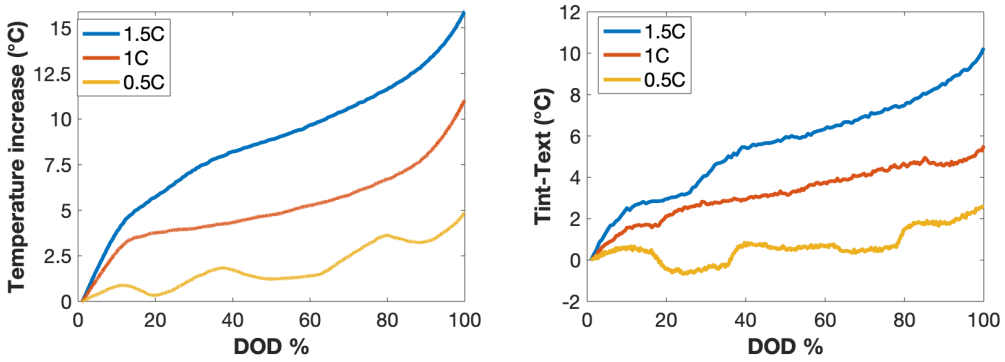


(a) (b)

**Figure 55:** a) Average internal temperature development as a function of depth of discharge (DOD) at different discharge rates during the temperature test. b) Difference in temperature increase between the internal and external temperature as a function of depth of discharge (DOD) at different discharge rates during the temperature test.

### Temperature test - Third LCO

The temperature test for the third LCO can be seen in Fig. 56. The internal resistance for this battery was much higher after sensor implementation compared to the second LCO. This can be observed from Fig. 56, as the temperature peaks are higher for the same discharge current. During this test, the top and bottom side of the battery was compressed, to enhance electrical contact between the electrodes. The test was conducted with six internal FBG sensors, three were placed in the middle of the cell, and three were placed at one side of the cell.

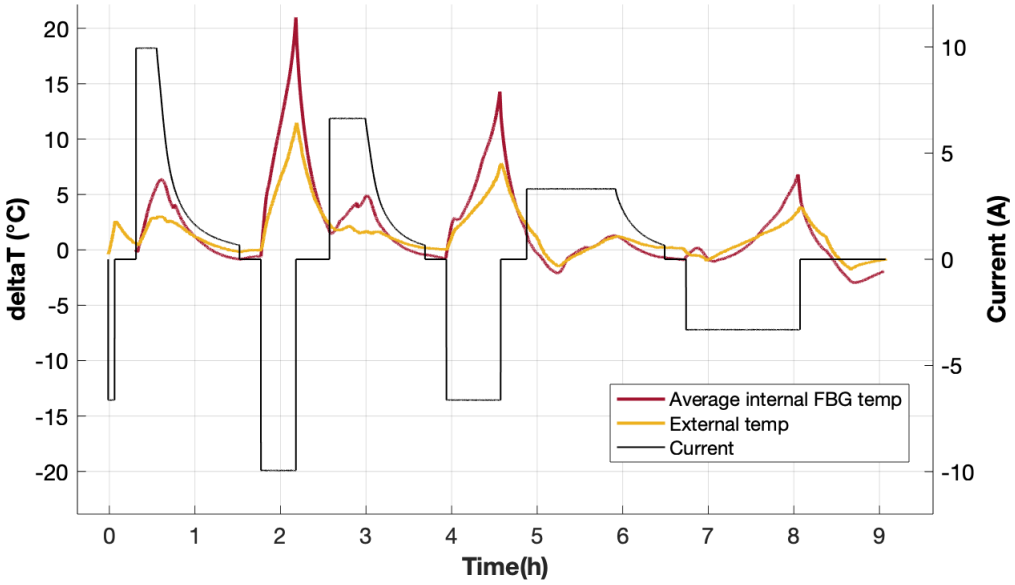


**Figure 56:** Overview of the temperature test for the third LCO, prior to cycle aging.

The 1.5C discharge from this temperature test is shown in Fig. 57. The highest internal temperature increase that was measured from the sensors was 22°C. There was some small variations for the different internal temperature sensors. However, two sensors consistently measured the highest temperature increase, and two sensors consistently measured the lowest temperature increase. The the sensors with the highest recorded temperature increase was the middle and bottom sensors in the middle of the cell. The lowest temperatures were recorded by the tab side sensors. The external thermistor was badly attached to the battery surface during this temperature test. Therefore, the external FBG sensor showed a greater response to the discharge. The ambient temperature sensor was placed in close proximity to the external FBG, and therefore showed a response to the discharge.

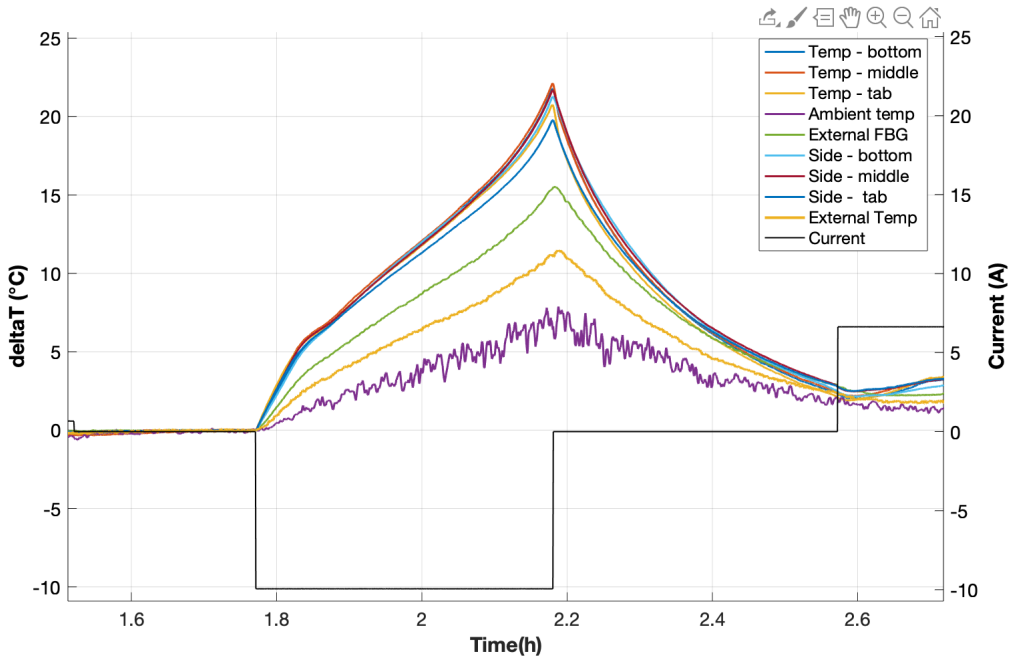


**Figure 57:** Temperature development during a 1.5C discharge for the third LCO.

The temperature response to the initial 1.5C charge is shown in Fig. 58. The battery was charged using a constant current process, followed by a constant voltage process in which the current is decreasing to a defined cut-off at C/10. There was a disturbance to the FBG sensors at around 0.75 hours. In contrast to the discharge temperature profile, which is at its steepest towards the end of discharge, the charging temperature increase at most at the start of charge and decay towards the high voltage limit. The temperature increased by 6.3°C internally, which is modest, considering that the charging was done at the maximum continuous charging rate of the battery.

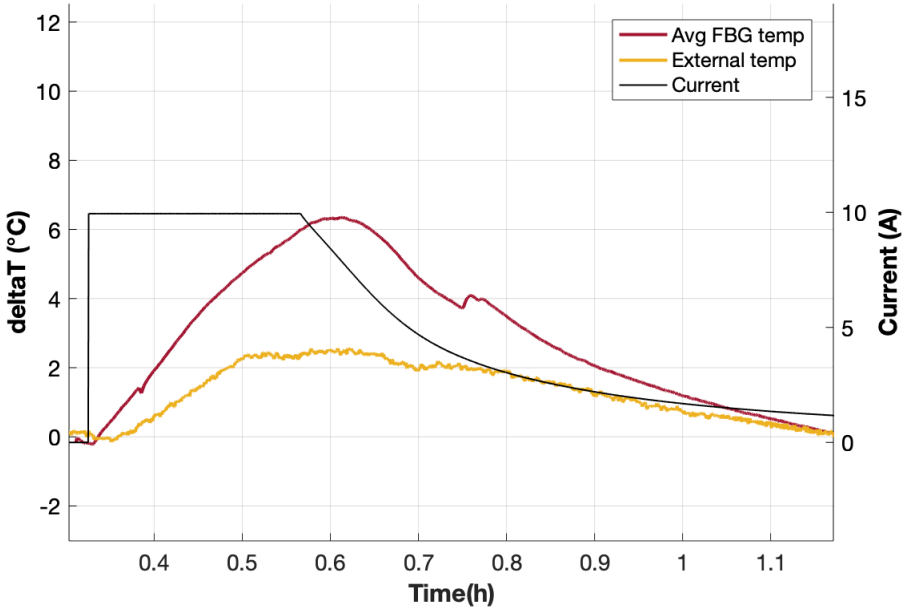


**Figure 58:** Temperature development during a 1.5C charge for the third LCO.

Fig. 59 shows the temperature response as a C/2 charge current is applied to the battery. It is apparent that as the charge started, the temperature decreased at a higher rate, compared to before the charging. The average temperature decrease rate 10 seconds before the onset of charging was -0.004°C/s. After applying the charge current it decreased to -0.01°C/s. This is because of the varying entropy coefficient of the battery during charging at different SOC. At the start of the charging process, the entropy change coefficient is negative, and the battery absorbs more heat than it generates [121].

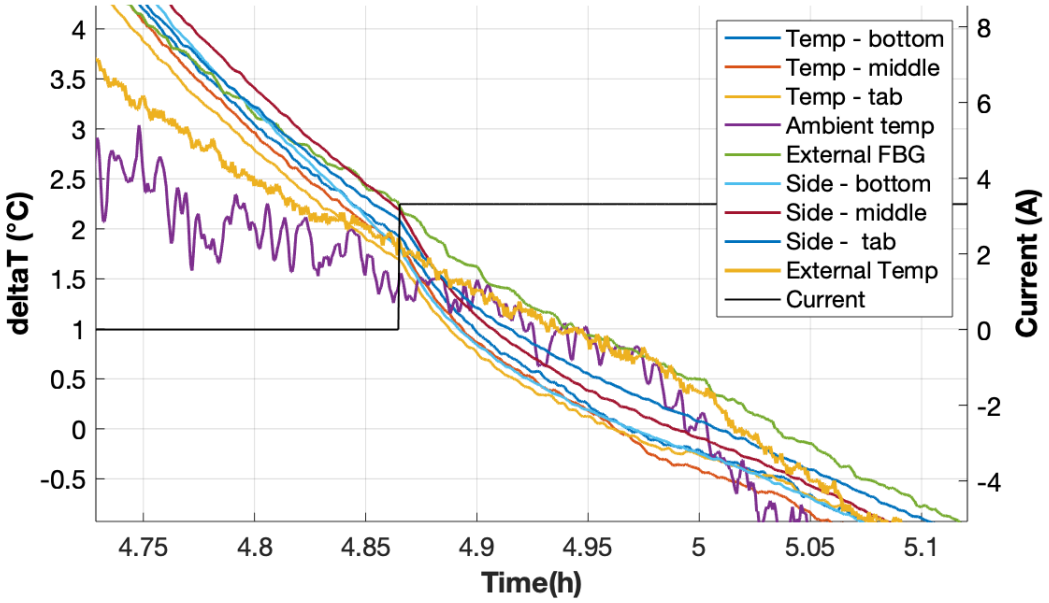


**Figure 59:** Temperature response to the onset of a C/2 charge, for the third LCO.

Fig. 60a) shows the average internal temperature profiles for the different discharge rates during the temperature test. The temperature increased at a high rate at the start of discharge, and towards the end of discharge. Fig. 60b) shows the difference in temperature increase between the external and internal temperature of the battery. The temperature deviations increased during discharge, and were of similar order to the temperature test for the second LCO (Fig. 55b)).

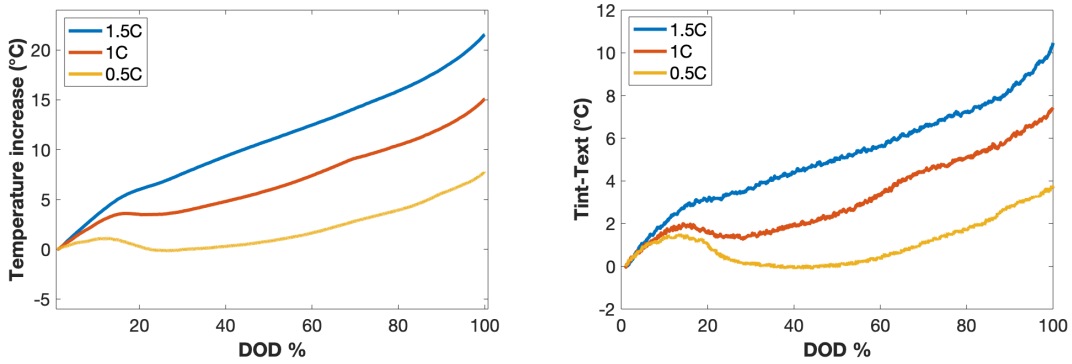


**(a)** **(b)**

**Figure 60:** a) Average internal temperature development as a function of depth of discharge (DOD) at different discharge rates during the temperature test. b) Difference in temperature increase between the internal and external temperature sensors as a function of depth of discharge (DOD) at different discharge rates.

### Post aging temperature test - Second LCO

A temperature test was done on the second LCO after cycle aging. This was done to observe how the aging effects had affected the thermodynamic properties of the battery. As described in section 4.2, the capacity of the battery was greatly reduced during cycle aging. The discharge capacity was reduced to under 25% of the initial capacity, and the internal resistance had increased by a factor 6 (see section 4.2). Despite the low capacity of the aged cell, there was a significant temperature response to all discharge currents that was applied during the test. The high internal resistance contributed to a large amount of ohmic heating, which compensated for the lower discharge capacity

of the cell. The post aging temperature test is shown in Fig. 61.

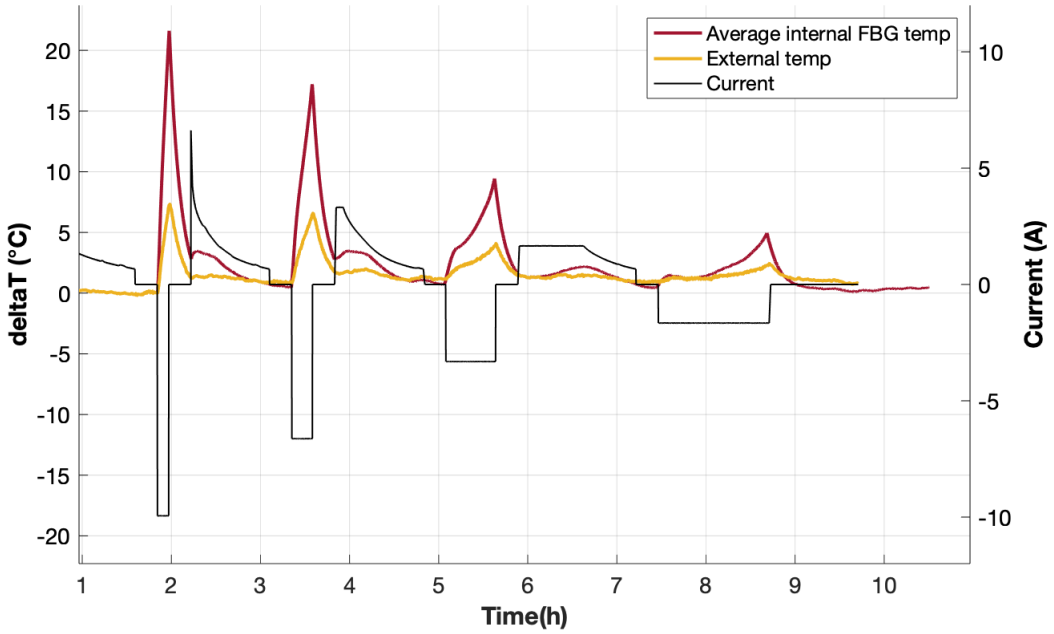


**Figure 61:** Overview of the post aging temperature test for the second LCO.

Because of the high internal resistance of the cell, an additional C/4 discharge was added to the end of the temperature test to see if a temperature response could be triggered. There was a slight initial increase in the internal temperature, and by the end of discharge the temperature was elevated by 4.4°C relative to the start of the discharge. The average internal temperature response for the different discharge rates of the test is shown in Fig. 62 a). Although the temperature response looks similar to the two previous tests, it must be noted that the discharge capacity was much lower, effectively reducing the duration of each discharge and the quantity of total current flow through the battery. The temperature increase rate was therefore much higher compared to the previous tests. Fig. 62b) shows the difference in temperature increase between the external and internal temperature of the battery. The highest difference was observed at end of the 1.5C discharge, with a temperature difference of 14.6°C.

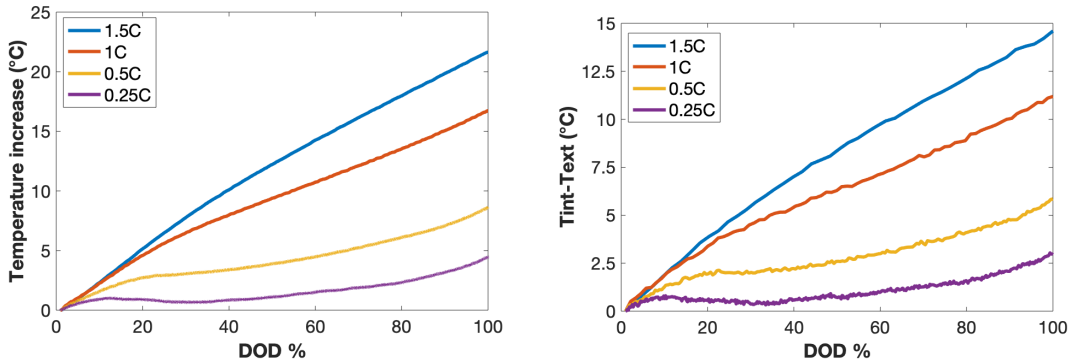


**(a)** **(b)**

**Figure 62:** a) Average internal temperature development as a function of depth of discharge (DOD) at different discharge rates during the temperature test. b) Difference in temperature increase between the internal and external temperature sensors as a function of depth of discharge (DOD) at different discharge rates.

Fig. 63 shows the internal temperature increase per Ah of discharge current for the different temperature tests. For instance, for a 1.5C discharge, the second and third LCO showed a temperature increase of around 4.0 - 5.3 °C/Ah. In contrast, the aged LCO had a temperature increase of 16.9 °C/Ah. If the discharge capacity of the aged LCO had been at its initial capacity of 6.65Ah, the internal temperature at end of discharge would be around 112°C, which is well above the thermal stability limit of the SEI layer of around 90°C [105]. At these temperatures the risk of inducing a thermal runaway in the battery is high. However, the 1.5C discharge capacity of the battery was reduced to 1.3Ah after cycle aging, which inhibited further temperature development.

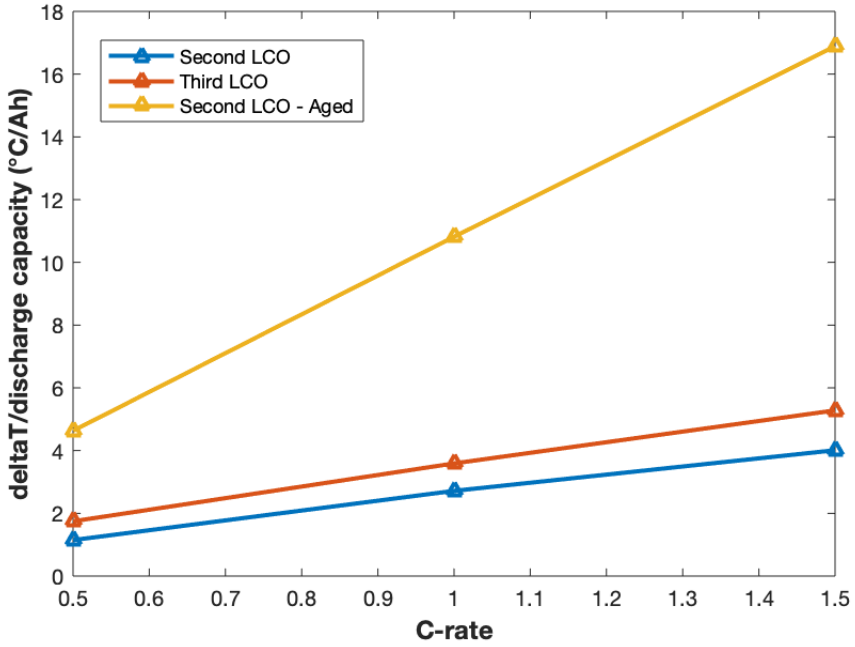


**Figure 63:** Temperature response to different discharge rates during the post aging temperature test.

The internal temperature increase rate for the different temperatures tests are shown in Fig. 65,66 and 67. There was a similar shape to the temperature increase rates for the first two tests. Initially, the temperature increase is high, followed by a decrease towards 20% DOD. Between 20% to 80% DOD, the heat generation is relatively steady, followed by a large increase around 80% DOD. The large temperature increase rate at end of discharge is caused by high cell polarization, and is in accordance with previous findings [122],[123]. The aged LCO in Fig. 67 showed a different temperature increase rate compared to the two other tests. Firstly, the increase rate was on average around three times higher for all C-rates. In addition, the temperature increase was more stable throughout the whole discharge, and no large increase was observed at end of discharge. The internal temperature increase rates during discharge are summarised in Fig 64. It can be observed that the temperature increase rate increases with roughly the square of the current increase, which is in accordance with the irreversible ohmic heat generation (Eq. 2).

**TEMPERATURE INCREASE RATE [°C/S]**

| | 1.5C | 1C | 0.5C | 0.25C |
|---|---|---|---|---|
| **LCO 2** | 0.011 | 0.005 | 0.0011 | - |
| **LCO 3** | 0.015 | 0.0066 | 0.0016 | - |
| **LCO 2 - AGED** | 0.0469 | 0.0201 | 0.0043 | 0.001 |

**Figure 64:** Temperature increase rates for the discharges during the temperature tests.

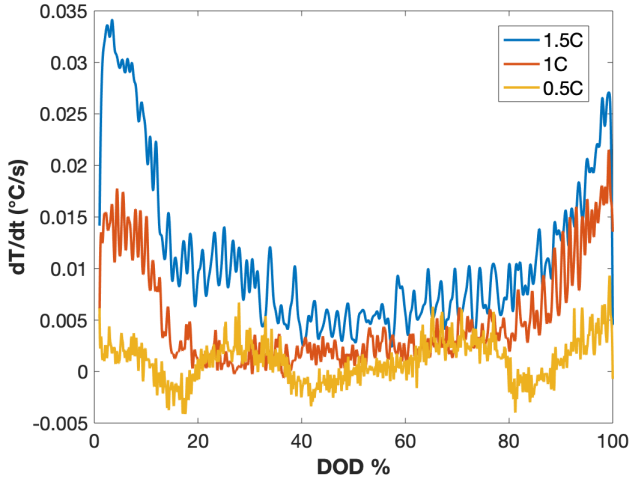


**Figure 65:** Temperature increase rate for the second LCO before cycle aging.

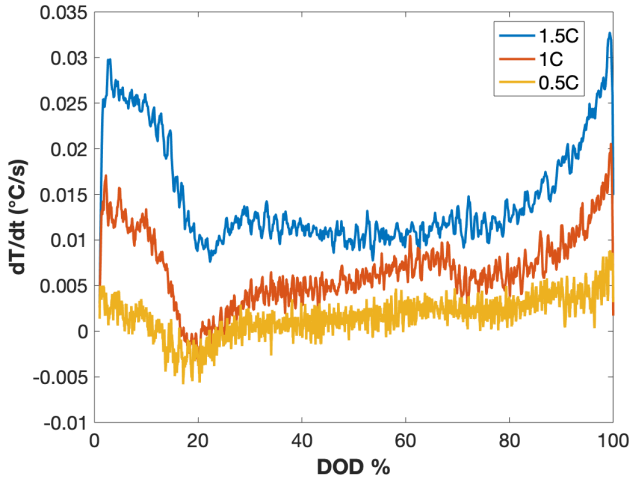


**Figure 66:** Temperature increase rate for the third LCO before cycle aging.

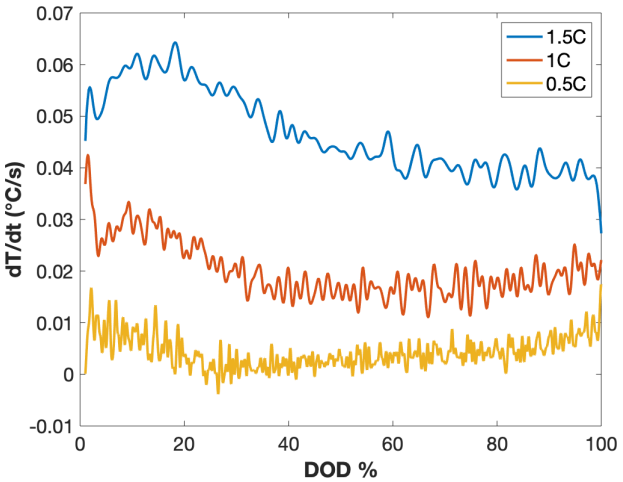


**Figure 67:** Temperature increase rate for the second LCO after cycle aging.

From the temperature tests, it is clear that the temperature response for all tests were significant. The high internal resistance after cell opening and sensor implementation contributed to a large amount of irreversible ohmic heating during charge and discharge (see section 2.2.1). Therefore, the heat generation was significantly higher, although the discharge capacity was greatly reduced. Also, the highest C-rate of 1.5C that was used during the test is far below the maximum continuous discharge current of the batteries at 10C, which shows the potential for temperature development in the batteries.

The temperature increase during charging was consistently lower than the temperature increase during discharge for all temperature tests. During charging, the reversible reaction heat is endothermic (see section 2.2.1), which gives a lower heat generation rate compared to discharging, where both heat generation terms are exothermic. In addition, due to elevated internal resistances, the time to reach the upper voltage limit during charging was greatly reduced, which shortened the charging time at higher current compared to a fresh cell. During the discharge process, the battery was able to sustain a high current load for approximately 50% longer than during discharge, which enabled more thermal energy to be released.

## 4.4 Visual inspection

Two of the cells were opened after aging and temp tests to do a visual inspection. It was noticed after cycle aging that the thickness of the cells had increased. This can be seen in Fig. 68. This cell was compressed at the tab side during cycle aging and temp tests. The side of the cell that was not compressed clearly increased its thickness during the aging process.

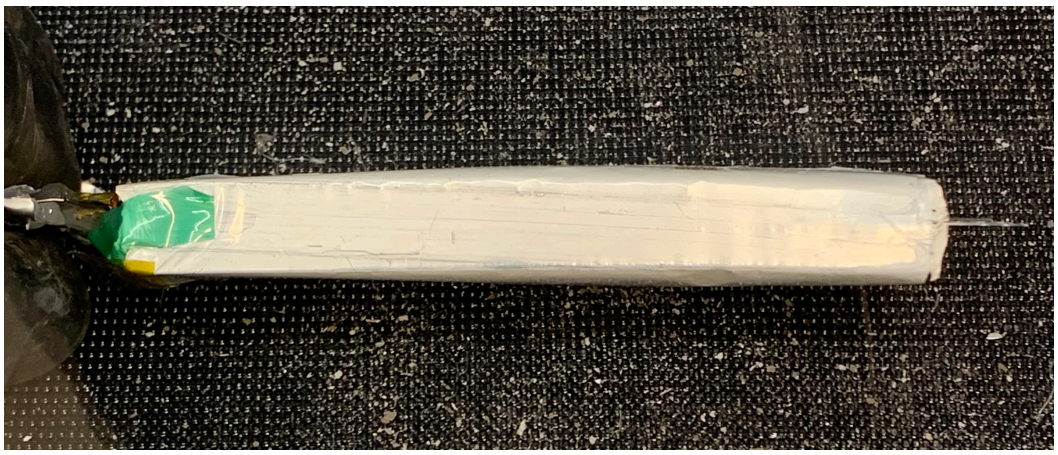

**Figure 68:** Side view of the aged cell. The thickness increase towards the bottom of the cell is evident.

As the cell was opened, it was clear that the anode electrodes were highly deteriorated. The electrodes were loosely held together, and no sign of moisture was seen, which points towards electrolyte dry out. Fig. 69 shows the surface of the graphite anode where the glass capillaries were inserted. Clearly, the area around the capillaries was less affected, possibly because the loss of electrical contact with the separator made the area chemically inactive. Fig. 70 shows the surface of two different anodes of the cell. The traces from the capillaries were highly visible, also in the anodes that were placed several layers from the anode with the glass capillaries. The capillaries may have created an additional "tracks" of pressure that made the electrode area more chemically active and therefore more deteriorated.

**Figure 69:** Traces of the glass capillaries on the anode surface where the glass capilarries were placed.

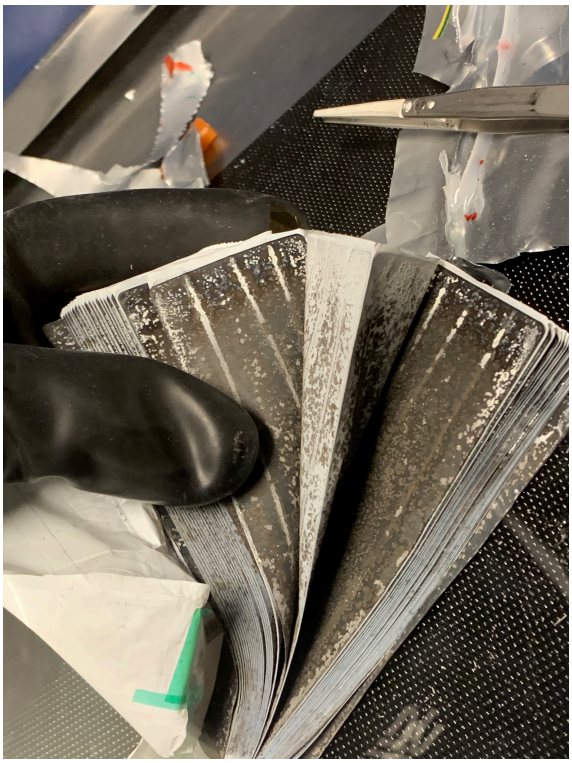

**Figure 70:** Traces of the glass capillaries on the anode surface several layers from the anode with the glass capillaries.

An image of the anodes and cathodes is shown in Fig. 71. The anode surface was clearly affected with a white surface layer. The cathode surface looks more or less unaffected compared to a new cell.

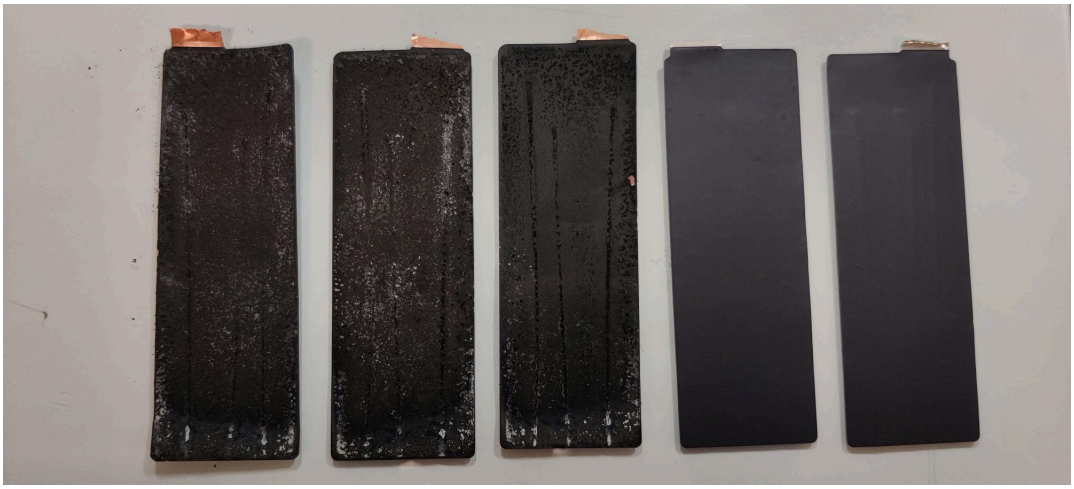

**Figure 71:** Image of anodes to the left and cathodes to the right, from an aged cell.

An image of the separator is shown in Fig. 72. The separator had pieces of the graphite anode stuck onto it as it was removed from the cell. Traces from the glass capillaries was also clearly visible on the separator surface. The mid part of the separator in the image is where the glass capillaries were located.

**Figure 72:** Image of the separator of an aged cell.

# 5 Conclusion

In order to gain understanding on the thermal behaviour in lithium-ion batteries, internal temperature measurements of the battery in operation are valuable. Increased knowledge of the thermal characteristics can increase the accuracy of thermal management systems, and improve battery performance and longevity.

In this thesis FBG temperature sensors were implemented in three different LCO batteries. The batteries were characterised before and after implementation to evaluate the effect of the implementation procedure on the battery performance. The characterizations revealed that the sensor implementation in the battery was clearly affecting the cell performance. This was seen as an immediate effect with increase in internal resistance and loss of capacity. Cell characterisations after the implementation procedure showed that the immediate negative effects were larger for the cells with internal sensors, compared to the reference cell without internal sensors. However, during cycle aging the relative performance decrease measured by capacity fade and internal resistance were similar for all cells. This indicates that the FBG sensors were not the main reason for cell degradation during cycle aging. The rapid aging behaviour could be caused by minor leaks in the pouch cell, which would cause the electrolyte to dry out. This was confirmed during the visual inspection of the cells, as no electrolyte moisture was apparent on the electrodes.

The temperature tests revealed the thermodynamic response for the batteries at different charge and discharge rates. The temperature development during the tests were significant and was likely dominated by irreversible ohmic heating due to high internal resistance. The internal temperature measurements were less affected by changes in the ambient temperature and showed greater response to the applied current, compared to the external sensors. The difference between the measured internal and external temperature increased with higher C-rates and peaked at the end of discharge. The maximum temperature difference between the external and internal temperature sensor was 14.6°C, at the end of a 1.5C discharge in the aged battery. The temperature increase rate was highest at the end of discharge for all C-rates. After enduring cycle aging, the temperature increase rate of the battery was approximately three times higher. This lead to a large temperature response although the discharge capacity of the battery was highly reduced.

The thesis revealed the advantages of internal temperature monitoring with fiber optic sensors for accurate measurement of cell temperatures in use. However, impact of the implementation process was detrimental to the cell performance and could not be realistically adapted to real applications. To ensure that cell performance is sustained after sensor implementation and throughout the cycle life of the cell, new implementation methods should be investigated.

# Bibliography


[1] European Commission Press Release. https://ec.europa.eu/commission/presscorner/detail/en/ip_20_1542, Sep 2020. Accessed: 2021-12-13.

[2] Le Varlet Thomas, Oliver Schmidt, Ajay Gambhir, Sheridan Few, and Iain Staffell. Comparative life cycle assessment of lithium-ion battery chemistries for residential storage. *Journal of Energy Storage*, 28:101230, 4 2020.

[3] Kailong Liu, Kang Li, Qiao Peng, and Cheng Zhang. A brief review on key technologies in the battery management system of electric vehicles.

[4] Susana Novais, Micael Nascimento, Lorenzo Grande, Maria Fátima Domingues, Paulo Antunes, Nélia Alberto, Cátia Leitão, Ricardo Oliveira, Stephan Koch, Guk Tae Kim, Stefano Passerini, and João Pinto. Internal and external temperature monitoring of a li-ion battery with fiber bragg grating sensors. *Sensors (Switzerland)*, 16, 2016.

[5] Zhe Li, Jianbo Zhang, Bin Wu, Jun Huang, Zhihua Nie, Ying Sun, Fuqiang An, and Ningning Wu. Examining temporal and spatial variations of internal temperature in large-format laminated battery with embedded thermocouples. *Journal of Power Sources*, 241:536–553, 11 2013.

[6] Madhu Santosh K. Mutyala, Jingzhou Zhao, Jianyang Li, Hongen Pan, Chris Yuan, and Xiaochun Li. In-situ temperature measurement in lithium ion battery by transferable flexible thin film thermocouples. *Journal of Power Sources*, 260:43–49, 8 2014.

[7] S. J. Drake, M. Martin, D. A. Wetz, J. K. Ostanek, S. P. Miller, J. M. Heinzel, and A. Jain. Heat generation rate measurement in a li-ion cell at large c-rates through temperature and heat flux measurements. *Journal of Power Sources*, 285:266–273, 7 2015.

[8] Micael Nascimento, Tiago Paixão, Marta S. Ferreira, and João L. Pinto. Thermal mapping of a lithium polymer batteries pack with fbgs network. *Batteries 2018, Vol. 4, Page 67*, 4:67, 12 2018.

[9] Jan Meyer, Antonio Nedjalkov, Alexander Doering, Martin Angelmahr, and Wolfgang Schade. Fiber optical sensors for enhanced battery safety. *https://doi.org/10.1117/12.2183325*, 9480:190–201, 5 2015.

[10] Lars Wilko Sommer, Peter Kiesel, Anurag Ganguli, Alexander Lochbaum, Bhaskar Saha, Julian Schwartz, Chang Jun Bae, Mohamed Alamgir, and Ajay Raghavan. Fast and slow ion diffusion processes in lithium ion pouch cells during cycling observed with fiber optic strain sensors. *Journal of Power Sources*, 296:46–52, 11 2015.

[11] Chang Jun Bae, Ashish Manandhar, Peter Kiesel, and Ajay Raghavan. Monitoring the strain evolution of lithium-ion battery electrodes using an optical fiber bragg grating sensor. *Energy Technology*, 4:851–855, 7 2016.

[12] Anurag Ganguli, Bhaskar Saha, Ajay Raghavan, Peter Kiesel, Kyle Arakaki, Andreas Schuh, Julian Schwartz, Alex Hegyi, Lars Wilko Sommer, Alexander Lochbaum, Saroj Sahu, and Mohamed Alamgir. Embedded fiber-optic sensing for accurate internal monitoring of cell state in advanced battery management systems part 2: Internal cell signals and utility for state estimation. *Journal of Power Sources*, 341:474–482, 2 2017.

[13] Yen Jie Ee, Kok Soon Tey, Kok Sing Lim, Prashant Shrivastava, S. B.R.S. Adnan, and Harith Ahmad. Lithium-ion battery state of charge (soc) estimation with non-electrical parameter using uniform fiber bragg grating (fbg). *Journal of Energy Storage*, 40:102704, 8 2021.

[14] Bruno Rente, Matthias Fabian, Miodrag Vidakovic, Xuan Liu, Xiang Li, Kang Li, Tong Sun, and Kenneth T.V. Grattan. Lithium-ion battery state-of-charge estimator based on fbg-based strain sensor and employing machine learning. *IEEE Sensors Journal*, 21:1453–1460, 1 2021.

[15] Carlos Vidal, Pawel Malysz, Phillip Kollmeyer, and Ali Emadi. Machine learning applied to electrified vehicle battery state of charge and state of health estimation: State-of-the-art. *IEEE Access*, 8:52796–52814, 2020.

[16] Odne Stokke Burheim. *Engineering Energy Storage*. 2017.

[17] Markus S. Wahl, Lena Spitthoff, Harald I. Muri, Asanthi Jinasena, Odne S. Burheim, and Jacob J. Lamb. The importance of optical fibres for internal temperature sensing in lithium-ion batteries during operation. *Energies*, 14:3617, 6 2021.

[18] Naoki Nitta, Feixiang Wu, Jung Tae Lee, and Gleb Yushin. Li-ion battery materials: Present and future, 2015.

[19] Lithium batteries: Science and technology - christian julien, alain mauger, ashok vijh, karim zaghib - google books.

[20] Zhenfei Cai, Yangzhou Ma, Xuanning Huang, Xiaohui Yan, Zexin Yu, Shihong Zhang, Guangsheng Song, Youlong Xu, Cuie Wen, and Weidong Yang. High electrochemical stability al-doped spinel limn2o4 cathode material for li-ion batteries. *Journal of Energy Storage*, 27:101036, 2 2020.

[21] Roland Jung, Michael Metzger, Filippo Maglia, Christoph Stinner, and Hubert A. Gasteiger. Oxygen release and its effect on the cycling stability of lini x mn y co z o 2 (nmc) cathode materials for li-ion batteries. *Journal of The Electrochemical Society*, 164:A1361–A1377, 5 2017.

[22] C. H. Chen, J. Liu, M. E. Stoll, G. Henriksen, D. R. Vissers, and K. Amine. Aluminum-doped lithium nickel cobalt oxide electrodes for high-power lithium-ion batteries. *Journal of Power Sources*, 128:278–285, 4 2004.

[23] Davion Hill, Michael Kleinberg, and Jason Goodhand. 2020 battery performance scorecard dnv. https://www.dnv.com/Publications/2020-battery-performance-scorecard-192180, Des 2020. Accessed: 2021-11-04.

[24] Te Tian, Tian Wen Zhang, Yi Chen Yin, Yi Hong Tan, Yong Hui Song, Lei Lei Lu, and Hong Bin Yao. Blow-spinning enabled precise doping and coating for improving high-voltage lithium cobalt oxide cathode performance. *Nano Letters*, 20:677–685, 1 2020.

[25] Xiao Wang, Xinyang Wang, and Yingying Lu. Realizing high voltage lithium cobalt oxide in lithium-ion batteries. *Industrial and Engineering Chemistry Research*, 58:10119–10139, 6 2019.

[26] Victord Zhuravlev, Anna V Shikhovtseva, Larisa V Ermakova, Elizavetayu Evshchik, Elena A Sherstobitova, Dmitry V Novikov, Olga V Bushkova, and Yuri A Dobrovolsky. Solution combustion synthesis of lithium cobalt oxide–cathode material for lithium-ion batteries. *electrochemsci.org*, 14:2965–2983, 2019.

[27] Lichuan Wei, Zhao Lu, Feng Cao, Liyu Zhang, Xi Yang, Xiaoling Yu, and Liwen Jin. A comprehensive study on thermal conductivity of the lithium-ion battery. *International Journal of Energy Research*, 44:9466–9478, 10 2020.

[28] Mitsunobu Sato, Li Lu, and Hiroki Nagai. Lithium-ion batteries thin film for energy materials and devices. 2020.

[29] K. Lahtinen, T. Rauhala, S. Räsänen, E. Rautama, and T. Kallio. The effect of synthesis modifications on the lithium cobalt oxide using commercial precursors. *Electrochimica Acta*, 327:135012, 12 2019.

[30] Jian Xia, Lin Ma, K. J. Nelson, Mengyun Nie, Zhonghua Lu, and J. R. Dahn. A study of li-ion cells operated to 4.5 v and at 55°c. *Journal of The Electrochemical Society*, 163:A2399–A2406, 9 2016.

[31] Takahiro Kozawa, Toshiya Harata, and Makio Naito. Fabrication of an limn2o4@limnpo4 composite cathode for improved cycling performance at high temperatures. *https://doi.org/10.1080/21870764.2020.1743413*, 8:309–317, 4 2020.

[32] Do Kyung Kim, P. Muralidharan, Hyun Wook Lee, Riccardo Ruffo, Yuan Yang, Candace K. Chan, Hailin Peng, Robert A. Huggins, and Yi Cui. Spinel limn2o4 nanorods as lithium ion battery cathodes. *Nano Letters*, 8:3948–3952, 11 2008.

[33] Arihant Bhandari and Jishnu Bhattacharya. Review—manganese dissolution from spinel cathode: Few unanswered questions. *Journal of The Electrochemical Society*, 164:A106–A127, 12 2017.

[34] Dong Ren, Elliot Padgett, Yao Yang, Luxi Shen, Yun Shen, Barnaby D.A. Levin, Yingchao Yu, Francis J. Disalvo, David A. Muller, and Héctor D. Abruña. Ultrahigh rate performance of a robust lithium nickel manganese cobalt oxide cathode with preferentially orientated li-diffusing channels. *ACS Applied Materials and Interfaces*, 11:41178–41187, 11 2019.

[35] Fengxia Xin, Hui Zhou, Xiaobo Chen, Mateusz Zuba, Natasha Chernova, Guangwen Zhou, and M. Stanley Whittingham. Li-nb-o coating/substitution enhances the electrochemical performance of the lini0.8mn0.1co0.1o2 (nmc 811) cathode. *ACS Applied Materials and Interfaces*, 11:34889–34894, 9 2019.

[36] Debasish Mohanty, Kevin Dahlberg, David M. King, Lamuel A. David, Athena S. Sefat, David L. Wood, Claus Daniel, Subhash Dhar, Vishal Mahajan, Myongjai Lee, and Fabio Albano. Modification of ni-rich fcg nmc and nca cathodes by atomic layer deposition: Preventing surface phase transitions for high-voltage lithium-ion batteries. *Scientific Reports 2016 6:1*, 6:1–16, 5 2016.

[37] Arefeh Kazzazi, Dominic Bresser, Agnese Birrozzi, Jan Von Zamory, Maral Hekmatfar, and Stefano Passerini. Comparative analysis of aqueous binders for high-energy li-rich nmc as a lithium-ion cathode and the impact of adding phosphoric acid. *ACS Applied Materials and Interfaces*, 10:17214–17222, 5 2018.

[38] Jan-Patrick Schmiegel, Xin Qi, Sven Klein, Volker Winkler, Marco Evertz, Roman Nölle, Jonas Henschel, Jakub Reiter, Lydia Terborg, Quan Fan, Chengdu Liang, Sascha Nowak, Martin Winter, and Tobias Placke. Improving the cycling performance of high-voltage nmc111 —— graphite lithium ion cells by an effective urea-based electrolyte additive. *Journal of The Electrochemical Society*, 166:A2910–A2920, 8 2019.

[39] Jason R. Croy, Arturo Gutierrez, Meinan He, Bryan T. Yonemoto, Eungje Lee, and Michael M. Thackeray. Development of manganese-rich cathodes as alternatives to nickel-rich chemistries. *Journal of Power Sources*, 434:226706, 9 2019.

[40] Jianming Zheng, Pengfei Yan, Jiandong Zhang, Mark H. Engelhard, Zihua Zhu, Bryant J. Polzin, Steve Trask, Jie Xiao, Chongmin Wang, and Jiguang Zhang. Suppressed oxygen extraction and degradation of lini x mn y co z o2 cathodes at high charge cut-off voltages. *Nano Research 2017 10:12*, 10:4221–4231, 9 2017.

[41] Büşra Çetin, Zeyneb Camtakan, and Neslihan Yuca. Synthesis and characterization of li-rich cathode material for lithium ion batteries. *Materials Letters*, 273:127927, 8 2020.

[42] Agus Purwanto, Cornelius Satria Yudha, U. Ubaidillah, Hendri Widiyandari, Takashi Ogi, and Hery Haerudin. Nca cathode material: synthesis methods and performance enhancement efforts. *Materials Research Express*, 5:122001, 9 2018.

[43] Maxwell D. Radin, Sunny Hy, Mahsa Sina, Chengcheng Fang, Haodong Liu, Julija Vinckeviciute, Minghao Zhang, M. Stanley Whittingham, Y. Shirley Meng, and Anton Van der Ven. Narrowing the gap between theoretical and practical capacities in li-ion layered oxide cathode materials. *Advanced Energy Materials*, 7:1602888, 10 2017.

[44] Sven Klein, Martin Winter, and Tobias Placke. Investigation of new electrolyte additives for improvement of nickel-rich cathode materials at high-voltage in lithium ion batteries. *ECS Meeting Abstracts*, MA2018-02:432, 7 2018.

[45] She huang Wu and Po Han Lee. Storage fading of a commercial 18650 cell comprised with nmc/lmo cathode and graphite anode. *Journal of Power Sources*, 349:27–36, 5 2017.

[46] Jason R. Croy, Brandon R. Long, and Mahalingam Balasubramanian. A path toward cobalt-free lithium-ion cathodes. *Journal of Power Sources*, 440:227113, 11 2019.

[47] Yanli Ruan, Xiangyun Song, Yanbao Fu, Chengyu Song, and Vincent Battaglia. Structural evolution and capacity degradation mechanism of lini0.6mn0.2co0.2o2 cathode materials. *Journal of Power Sources*, 400:539–548, 10 2018.

[48] Fredrick Omenya, Natasha A. Chernova, Hui Zhou, Carrie Siu, and M. Stanley Whittingham. Comparative study nickel rich layered oxides: Nmc 622, nmc 811 and nca cathode materials for lithium ion battery. *ECS Meeting Abstracts*, MA2018-01:531, 4 2018.

[49] Marissa Wood, Jianlin Li, Rose E. Ruther, Zhijia Du, Ethan C. Self, Harry M. Meyer, Claus Daniel, Ilias Belharouak, and David L. Wood. Chemical stability and long-term cell performance of low-cobalt, ni-rich cathodes prepared by aqueous processing for high-energy li-ion batteries. *Energy Storage Materials*, 24:188–197, 1 2020.

[50] Katharina Märker, Philip J. Reeves, Chao Xu, Kent J. Griffith, and Clare P. Grey. Evolution of structure and lithium dynamics in lini0.8mn0.1co0.1o2 (nmc811) cathodes during electrochemical cycling. *Chemistry of Materials*, 31:2545–2554, 4 2019.

[51] Tao Zhang, Jun Yang, Zhixin Xu, Hongping Li, Yongsheng Guo, Chengdu Liang, and Jiulin Wang. Suppressing dendrite growth of a lithium metal anode by modifying conventional polypropylene separators with a composite layer. *ACS Applied Energy Materials*, 3:506–513, 1 2020.

[52] Kang Joon Park, Jang Yeon Hwang, Hoon Hee Ryu, Filippo Maglia, Sung Jin Kim, Peter Lamp, Chong S. Yoon, and Yang Kook Sun. Degradation mechanism of ni-enriched nca cathode for lithium batteries: Are microcracks really critical? *ACS Energy Letters*, 4:1394–1400, 6 2019.

[53] Kang Joon Park, Min Jae Choi, Filippo Maglia, Sung Jin Kim, Kwang Ho Kim, Chong S. Yoon, and Yang Kook Sun. High-capacity concentration gradient li[ni0.865co0.120al0.015]o2 cathode for lithium-ion batteries. *Advanced Energy Materials*, 8:1703612, 7 2018.

[54] Jiarong He, Haoxiang Zhong, Jinglun Wang, and Lingzhi Zhang. Investigation on xanthan gum as novel water soluble binder for lifepo4 cathode in lithium-ion batteries. *Journal of Alloys and Compounds*, 714:409–418, 8 2017.

[55] Michael G. Fischer, Xiao Hua, Bodo D. Wilts, Elizabeth Castillo-Martínez, and Ullrich Steiner. Polymer-templated lifepo4/c nanonetworks as high-performance cathode materials for lithium-ion batteries. *ACS Applied Materials and Interfaces*, 10:1646–1653, 1 2018.

[56] Yalun Li, Xuning Feng, Dongsheng Ren, Minggao Ouyang, Languang Lu, and Xuebing Han. Thermal runaway triggered by plated lithium on the anode after fast charging. *ACS Applied Materials  Interfaces*, 11:46839–46850, 12 2019.

[57] Himani Gupta, Shalu Kataria, Liton Balo, Varun Kumar Singh, Shishir Kumar Singh, Alok Kumar Tripathi, Yogendra Lal Verma, and Rajendra Kumar Singh. Electrochemical study of ionic liquid based polymer electrolyte with graphene oxide coated lifepo4 cathode for li battery. *Solid State Ionics*, 320:186–192, 7 2018.

[58] By Lung-Hao Hu, Feng Yu Wu, Cheng Te Lin, Andrei N. Khlobystov, and Lain Jong Li. Graphene-modified lifepo4 cathode for lithium ion battery beyond theoretical capacity. *Nature Communications 2013 4:1*, 4:1–7, 4 2013.

[59] Hao Zhang, Yang Yang, Dongsheng Ren, Li Wang, and Xiangming He. Graphite as anode materials: Fundamental mechanism, recent progress and advances. *Energy Storage Materials*, 36:147–170, 4 2021.

[60] Hui Cheng, Joseph G. Shapter, Yongying Li, and Guo Gao. Recent progress of advanced anode materials of lithium-ion batteries. *Journal of Energy Chemistry*, 57:451–468, 6 2021.

[61] Yan Lu, Le Yu, and Xiong Wen (David) Lou. Nanostructured conversion-type anode materials for advanced lithium-ion batteries. *Chem*, 4:972–996, 5 2018.

[62] Dingchang Lin, Yayuan Liu, and Yi Cui. Reviving the lithium metal anode for high-energy batteries. *Nature Nanotechnology 2017 12:3*, 12:194–206, 3 2017.

[63] P. Kurzweil and J. Garche. Overview of batteries for future automobiles. *Lead-Acid Batteries for Future Automobiles*, pages 27–96, 1 2017.

[64] Zhenhui Liu, Qiang Yu, Yunlong Zhao, Ruhan He, Ming Xu, Shihao Feng, Shidong Li, Liang Zhou, and Liqiang Mai. Silicon oxides: a promising family of anode materials for lithium-ion batteries. *Chemical Society Reviews*, 48:285–309, 1 2019.

[65] Nils Peter Wagner, Artur Tron, Julian Richard Tolchard, Gianluigi Noia, and Martin Pawel Bellmann. Silicon anodes for lithium-ion batteries produced from recovered kerf powders. *Journal of Power Sources*, 414:486–494, 2 2019.

[66] Cheol Min Park, Jae Hun Kim, Hansu Kim, and Hun Joon Sohn. Li-alloy based anode materials for li secondary batteries. *Chemical Society Reviews*, 39:3115–3141, 7 2010.

[67] Xin Bing Cheng, Rui Zhang, Chen Zi Zhao, and Qiang Zhang. Toward safe lithium metal anode in rechargeable batteries: A review. *Chemical Reviews*, 117:10403–10473, 8 2017.

[68] Marie Francine Lagadec, Raphael Zahn, and Vanessa Wood. Characterization and performance evaluation of lithium-ion battery separators. *Nature Energy 2018 4:1*, 4:16–25, 12 2018.

[69] Kai Liu, Yayuan Liu, Dingchang Lin, Allen Pei, and Yi Cui. Materials for lithium-ion battery safety. *Science Advances*, 4, 6 2018.

[70] Ortal Lavi, Shalom Luski, Netanel Shpigel, Chen Menachem, Zvika Pomerantz, Yuval Elias, and Doron Aurbach. Electrolyte solutions for rechargeable li-ion batteries based on fluorinated solvents. *ACS Applied Energy Materials*, 3:7485–7499, 8 2020.

[71] Sheng Shui Zhang. A review on electrolyte additives for lithium-ion batteries. *Journal of Power Sources*, 162:1379–1394, 11 2006.

[72] S Jung, D Kang Journal of Power Sources, and undefined 2014. Multi-dimensional modeling of large-scale lithium-ion batteries. *Elsevier*.

[73] Robert Schröder, Muhammed Aydemir, and Günther Seliger. Comparatively assessing different shapes of lithium-ion battery cells. *Procedia Manufacturing*, 8:104–111, 1 2017.

[74] Lighting Global. Lithium-ion Batteries Part I. https://www.lightingglobal.org/wp-content/uploads/2019/06/Lithium-Ion_TechNote-2019_update.pdf. Accessed: 2021-12-14.

[75] A Nazari, S Farhad Applied Thermal Engineering, and undefined 2017. Heat generation in lithium-ion batteries with different nominal capacities and chemistries. *Elsevier*.

[76] L. H.J. Raijmakers, D. L. Danilov, R. A. Eichel, and P. H.L. Notten. A review on various temperature-indication methods for li-ion batteries. *Applied Energy*, 240:918–945, 4 2019.

[77] J. Vetter, P. Novák, M. R. Wagner, C. Veit, K. C. Möller, J. O. Besenhard, M. Winter, M. Wohlfahrt-Mehrens, C. Vogler, and A. Hammouche. Ageing mechanisms in lithium-ion batteries. *Journal of Power Sources*, 147:269–281, 9 2005.

[78] Andreas Jossen. Fundamentals of battery dynamics. *Journal of Power Sources*, 154:530–538, 3 2006.

[79] Wei Wu, Xinran Xiao, and Xiaosong Huang. Esffuelcell2011-54785 modeling heat generation in a lithium ion battery. 2011.

[80] Yuqiang Zeng, Divya Chalise, Sean D. Lubner, Sumanjeet Kaur, and Ravi S. Prasher. A review of thermal physics and management inside lithium-ion batteries for high energy density and fast charging. *Energy Storage Materials*, 41:264–288, 10 2021.

[81] Frank Richter, Signe Kjelstrup, Preben J.S. Vie, and Odne S. Burheim. Thermal conductivity and internal temperature profiles of li-ion secondary batteries. *Journal of Power Sources*, 359:592–600, 8 2017.

[82] Gabriel M. Cavalheiro, Takuto Iriyama, George J. Nelson, Shan Huang, and Guangsheng Zhang. Effects of nonuniform temperature distribution on degradation of lithium-ion batteries. *Journal of Electrochemical Energy Conversion and Storage*, 17, 5 2020.

[83] T D Hatchard, D D Macneil, D A Stevens, L Christensen, and J R Dahn. Importance of heat transfer by radiation in li-ion batteries during thermal abuse. *Electrochemical and Solid-State Letters*, 3:305–308, 2000.

[84] M. Shadman Rad, D. L. Danilov, M. Baghalha, M. Kazemeini, and P. H.L. Notten. Adaptive thermal modeling of li-ion batteries. *Electrochimica Acta*, 102:183–195, 2013.

[85] Thomas Waldmann, Gunther Bisle, Björn-Ingo Hogg, Stefan Stumpp, Michael A. Danzer, Michael Kasper, Peter Axmann, and Margret Wohlfahrt-Mehrens. Influence of cell design on temperatures and temperature gradients in lithium-ion cells: An in operando study. *Journal of The Electrochemical Society*, 162:A921–A927, 3 2015.

[86] Yannic Troxler, Billy Wu, Monica Marinescu, Vladimir Yufit, Yatish Patel, Andrew J. Marquis, Nigel P. Brandon, and Gregory J. Offer. The effect of thermal gradients on the performance of lithium-ion batteries. *Journal of Power Sources*, 247:1018–1025, 2 2014.

[87] M. Broussely, S. Herreyre, P. Biensan, P. Kasztejna, K. Nechev, and R. J. Staniewicz. Aging mechanism in li ion cells and calendar life predictions. *Journal of Power Sources*, 97-98:13–21, 7 2001.

[88] Bor Yann Liaw, E. Peter Roth, Rudolph G. Jungst, Ganesan Nagasubramanian, Herbert L. Case, and Daniel H. Doughty. Correlation of arrhenius behaviors in power and capacity fades with cell impedance and heat generation in cylindrical lithium-ion cells. *Journal of Power Sources*, 119-121:874–886, 6 2003.

[89] Matthias Fleckenstein, Oliver Bohlen, Michael A. Roscher, and Bernard Bäker. Current density and state of charge inhomogeneities in li-ion battery cells with lifepo4 as cathode material due to temperature gradients. *Journal of Power Sources*, 196:4769–4778, 5 2011.

[90] Guangsheng Zhang, Lei Cao, Shanhai Ge, Chao-Yang Wang, Christian E. Shaffer, and Christopher D. Rahn. In situ measurement of radial temperature distributions in cylindrical li-ion cells. *Journal of The Electrochemical Society*, 161:A1499–A1507, 7 2014.

[91] Q. Wang, B. Jiang, Q. F. Xue, H. L. Sun, B. Li, H. M. Zou, and Y. Y. Yan. Experimental investigation on ev battery cooling and heating by heat pipes. *Applied Thermal Engineering*, 88:54–60, 9 2015.

[92] Jiayuan Lin, Xinhua Liu, Shen Li, Cheng Zhang, and Shichun Yang. A review on recent progress, challenges and perspective of battery thermal management system. *International Journal of Heat and Mass Transfer*, 167:120834, 3 2021.

[93] Youfu Lv, Xiaoqing Yang, Xinxi Li, Guoqing Zhang, Ziyuan Wang, and Chengzhao Yang. Experimental study on a novel battery thermal management technology based on low density polyethylene-enhanced composite phase change materials coupled with low fins. 2016.

[94] Xiongbin Peng, Siqi Chen, Akhil Garg, Nengsheng Bao, and Biranchi Panda. A review of the estimation and heating methods for lithium-ion batteries pack at the cold environment. *Energy Science  Engineering*, 7:645–662, 6 2019.

[95] Xiao-Guang Yang, Guangsheng Zhang, Shanhai Ge, and Chao-Yang Wang. Fast charging of lithium-ion batteries at all temperatures. *Proceedings of the National Academy of Sciences*, 115:7266–7271, 7 2018.

[96] Ahmad Pesaran, Shriram Santhanagopalan, and Gi-Heon Kim. Addressing the impact of temperature extremes on large format li-ion batteries for vehicle applications (presentation), nrel (national renewable energy laboratory). *Presented at the 30th International Battery Seminar, 11-14 March 2013, Ft. Lauderdale, Florida; Related Information: NREL (National Renewable Energy Laboratory)*, 2013.

[97] Thomas Waldmann, Marcel Wilka, Michael Kasper, Meike Fleischhammer, and Margret Wohlfahrt-Mehrens. Temperature dependent ageing mechanisms in lithium-ion batteries – a post-mortem study. *Journal of Power Sources*, 262:129–135, 9 2014.

[98] Naixing Yang, Xiongwen Zhang, Binbin Shang, and Guojun Li. Unbalanced discharging and aging due to temperature differences among the cells in a lithium-ion battery pack with parallel combination. *Journal of Power Sources*, 306:733–741, 2 2016.

[99] Carl Erik Lie Foss, Ann Mari Svensson, Øystein Gullbrekken, Svein Sunde, and Fride Vullum-Bruer. Temperature effects on performance of graphite anodes in carbonate based electrolytes for lithium ion batteries. *Journal of Energy Storage*, 17:395–402, 6 2018.

[100] P. Ramadass, Bala Haran, Ralph White, and Branko N. Popov. Mathematical modeling of the capacity fade of li-ion cells. *Journal of Power Sources*, 123:230–240, 9 2003.

[101] Matthew B. Pinson and Martin Z. Bazant. Theory of sei formation in rechargeable batteries: Capacity fade, accelerated aging and lifetime prediction. *Journal of The Electrochemical Society*, 160:A243–A250, 2013.

[102] Lena Spitthoff, Paul R. Shearing, and Odne Stokke Burheim. Temperature, ageing and thermal management of lithium-ion batteries. *Energies 2021, Vol. 14, Page 1248*, 14:1248, 2 2021.

[103] Victor Agubra and Jeffrey Fergus. Lithium ion battery anode aging mechanisms. *Materials*, 6:1310, 2013.

[104] Bramy Pilipili Matadi, Sylvie Geniès, Arnaud Delaille, Claude Chabrol, Eric de Vito, Michel Bardet, Jean-Frédéric Martin, Lise Daniel, and Yann Bultel. Irreversible capacity loss of li-ion batteries cycled at low temperature due to an untypical layer hindering li diffusion into graphite electrode. *Journal of The Electrochemical Society*, 164:A2374, 8 2017.

[105] Peizhao Lyu, Xinjian Liu, Jie Qu, Jiateng Zhao, Yutao Huo, Zhiguo Qu, and Zhonghao Rao. Recent advances of thermal safety of lithium ion battery for energy storage. *Energy Storage Materials*, 31:195–220, 10 2020.

[106] Yan Ji. Low-temperature operation of li-ion batteries for hybrid and electric vehicles a dissertation in mechanical engineering. 2014.

[107] Jacob J. Lamb and Bruno G. Pollet. Micro-optics and energy: Sensors for energy devices. *Micro-Optics and Energy: Sensors for Energy Devices*, pages 1–207, 1 2020.

[108] Jesus Castrellon-Uribe. Optical fiber sensors: An overview. *Fiber Optic Sensors*, 2 2012.

[109] Roghayeh Imani and Guillermo Huerta Cuellar. Introductory chapter: Optical fibers. *Optical Fiber Applications*, 4 2020.

[110] J. Komma, C. Schwarz, G. Hofmann, D. Heinert, and R. Nawrodt. Thermo-optic coefficient of silicon at 1550nm and cryogenic temperatures. *Applied Physics Letters*, 101:041905, 7 2012.

[111] Alan D. Kersey, Michael A. Davis, Heather J. Patrick, Michel LeBlanc, K. P. Koo, C. G. Askins, M. A. Putnam, and E. Joseph Friebele. Fiber grating sensors. *Journal of Lightwave Technology*, 15:1442–1462, 8 1997.

[112] Y Du, J Li, C Liu 2008 First International Conference on, and undefined 2008. A novel fiber bragg grating temperature compensated strain sensor. *ieeexplore.ieee.org*.

[113] Frode Østby. Internal temperature measurements in lithium ion battery with fbg, 2021.

[114] Glovebox mbraun labmaster pro. https://www.mbraun.com/us/products/glovebox-workstations.html.

[115] Anup Barai, Kotub Uddin, W. D. Widanage, Andrew McGordon, and Paul Jennings. A study of the influence of measurement timescale on internal resistance characterisation methodologies for lithium-ion cells. *Scientific Reports 2017 8:1*, 8:1–13, 1 2018.

[116] Li po battery cells -shenzhen melasta battery co.,ltd. https://www.melasta.com/cells/lithium-polymer-li-po-batteries-cells-.html.

[117] Christian Berge Foyn. Temperature measurement in lithium-ion batteries using fbg. 2021.

[118] Ajay Raghavan, Peter Kiesel, Lars Wilko Sommer, Julian Schwartz, Alexander Lochbaum, Alex Hegyi, Andreas Schuh, Kyle Arakaki, Bhaskar Saha, Anurag Ganguli, Kyung Ho Kim, Chae Ah Kim, Hoe Jin Hah, Seok Koo Kim, Gyu Ok Hwang, Geun Chang Chung, Bokkyu Choi, and Mohamed Alamgir. Embedded fiber-optic sensing for accurate internal monitoring of cell state in advanced battery management systems part 1: Cell embedding method and performance. *Journal of Power Sources*, 341:466–473, 2 2017.

[119] Seong Jin An, Jianlin Li, Debasish Mohanty, Claus Daniel, Bryant J. Polzin, Jason R. Croy, Stephen E. Trask, and David L. Wood. Correlation of electrolyte volume and electrochemical performance in lithium-ion pouch cells with graphite anodes and nmc532 cathodes. *Journal of The Electrochemical Society*, 164:A1195–A1202, 4 2017.

[120] Barbara Stiaszny, Jörg C. Ziegler, Elke E. Krauß, Mengjia Zhang, Jan P. Schmidt, and Ellen Ivers-Tiffée. Electrochemical characterization and post-mortem analysis of aged limn2o4–nmc/graphite lithium ion batteries part ii: Calendar aging. *Journal of Power Sources*, 258:61–75, 7 2014.

[121] G Zhang, S Ge, T Xu, XG Yang, H Tian, CY Wang Electrochimica Acta, and undefined 2016. Rapid self-heating and internal temperature sensing of lithium-ion batteries at low temperatures. *Elsevier*.

[122] Shengxin Zhu, Jindong Han, Tai Song Pan, Yi Min Wei, Wei Li Song, Hao Sen Chen, and Daining Fang. A novel designed visualized li-ion battery for in-situ measuring the variation of internal temperature. *Extreme Mechanics Letters*, 37:100707, 5 2020.

[123] Wenquan Lu, Hui Yang, and Jai Prakash. Determination of the reversible and irreversible heats of lini0.8co0.2o2/mesocarbon microbead li-ion cell reactions using isothermal microcalorimetery. *Electrochimica Acta*, 51:1322–1329, 1 2006.

# Appendix

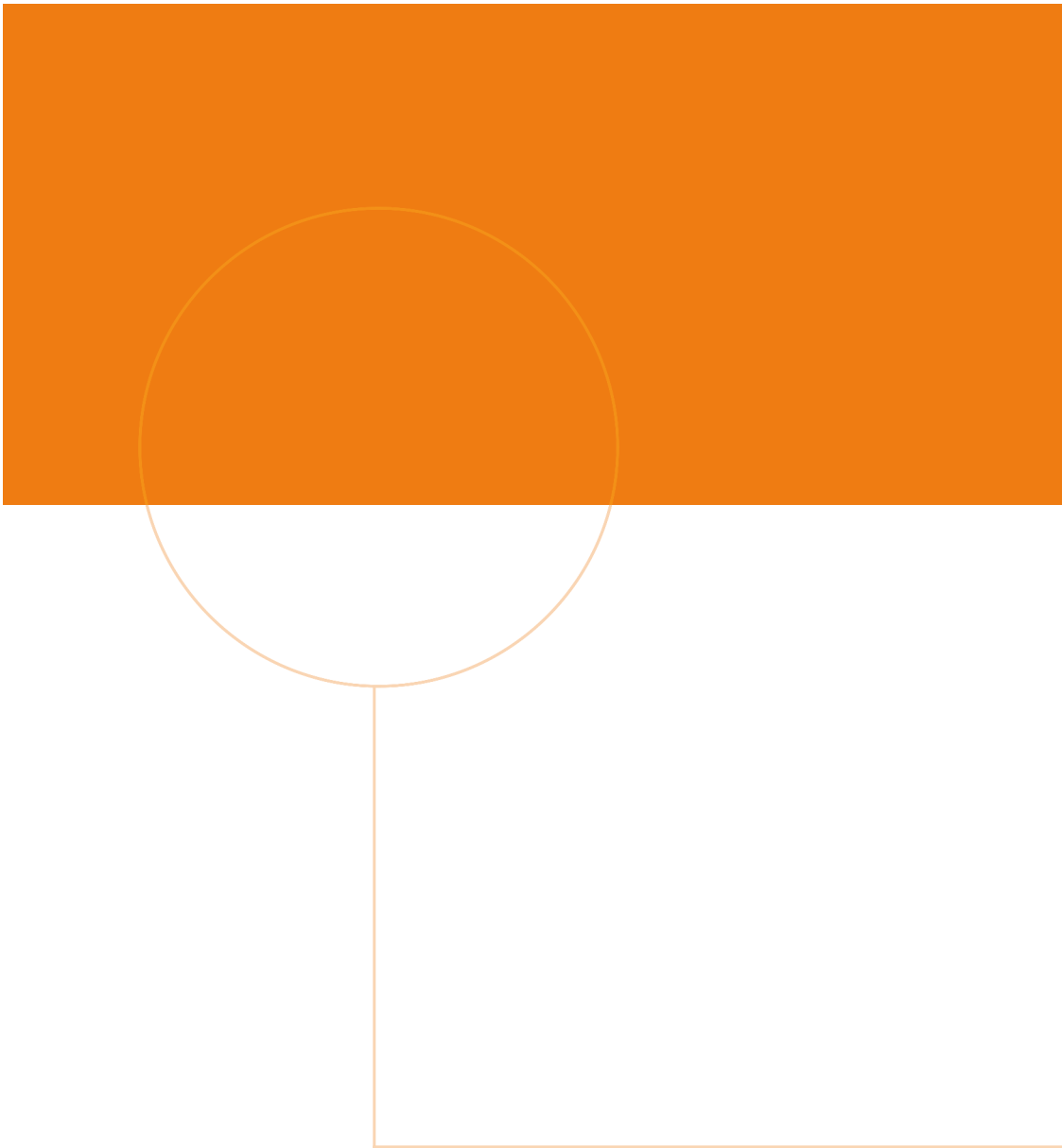

NTNU

Kunnskap for en bedre verden